Universidad de Concepción
Dirección de Postgrado
Facultad de Ciencias Químicas
Programa Doctorado en Ciencias Geológicas

Evolución Espacio-Temporal del Ciclo Eruptivo 2011 del Complejo Volcánico Puyehue Cordón Caulle (CVPCC), Andes del Sur

Tesis para optar al grado de Doctor en Ciencias Geológicas

DANIEL ARTURO BASUALTO ALARCÓN
CONCEPCIÓN-CHILE
MARZO DE 2019

Profesor Guía: Andrés Tassara Oddó
Dpto. de Ciencias de la Tierra, Facultad de Ciencias Químicas
Universidad de Concepción
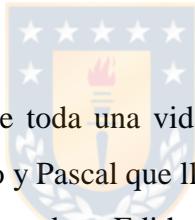
Dedico este trabajo a mi pareja de toda una vida, mi mujer, señora y esposa Dra. Marcela Calabi Floody, a mis hijos Máximo y Pascal que llegaron casi finalizando este extenso y difícil período de trabajo y estudio. A mis padres: Edith Alarcón Hunter y Alonso Basualto Arias por el incondicional apoyo durante estos 43 años de vida, estudio y trabajo.

Agradecimientos

Resumen

Las erupciones explosivas silíceas son uno de los fenómenos naturales más peligrosos, no obstante, poco se sabe sobre los procesos precursores que acompañan este tipo de erupciones, ya que son fenómenos poco comunes, registrando solo tres erupciones de este tipo en el último siglo (Novarupta Katmai 1912, Chaitén 2008, y Cordón Caulle 2011). En esta tesis presentamos la primera caracterización sistemática que se produce antes, durante y después de una gran erupción silícea, analizando datos geofísicos registrados en el Complejo Volcánico Puyehue Cordón Caulle (PCCVC) durante la erupción riolítica VEI=4 generada en junio 4 de 2011. La mayoría de los datos fueron registrados por la red de monitoreo del Observatorio Volcanológico de los Andes del Sur (OVDAS). El reprocesamiento de los datos sismológicos analizados durante el ciclo eruptivo se realizó dos años después de la erupción, desarrollando un exhaustivo análisis de inversiones sísmicas, mecanismos focales, una serie de tiempo del valor b y la relocalización de hipocentros generados gracias a un nuevo modelo local de velocidad 1D. Con esto se logró describir la evolución espacio-temporal de la sismicidad durante la crisis volcánica, logrando identificar las estructuras principales que controlaron la erupción. Considerando este extenso y meticuloso reprocesamiento, se logró identificar dos grandes fases durante la crisis registrada en 2011 (pre-eruptiva y post-eruptiva), las que fueron descritas y analizadas en profundidad. Ya generada la erupción, Wendt et al. (2016) detectó una deformación de la superficie a una escala métrica, la que logró ser observada por una serie de satélites ASAR de Envisat y una serie de tiempo de dos estaciones de GPS continuos. Además, la deformación descrita antes, durante y después de la erupción logró ser modelada, identificando varias fuentes puntuales y de tipo dique, las que se distribuyeron alineadas a lo largo del graben de Cordón Caulle. Las observaciones de GPS cerca del complejo volcánico revelaron un efecto adicional más localizado, esto debido a la reactivación sísmica registrada en el Sistema de Fallas Liquiñe-Ofqui (SFLO) al sureste del complejo durante la erupción. De igual forma, la deformación co-eruptiva del CVPCC fue consistente con la migración de la sismicidad relocalizada, la que se concentró principalmente a lo largo del Graben del Cordón Caulle y en la zona más oriental de éste, lugar donde se intercepta el graben (rumbo NW) con la SFLO (de rumbo NNE) y donde finalmente se produjo la erupción de 2011. El 15 de junio se inició la Fase Efusiva de la erupción, logrando ser seguida gracias al análisis de imágenes satelitales realizado por Bertín et al. (2015). Con estas imágenes se pudo corroborar que las

altas tasas de emisión en lavas silíceas son más frecuentes de lo que se pensaba, en particular durante las etapas eruptivas iniciales. Las aceleradas tasas de lavas viscosas fueron capaces de generar un tipo especial de tremor sísmico, denominado cuasi-armónico, el que fue utilizado para establecer una relación entre dicho tremor y las velocidades de emisión de lavas en superficie. Tal correspondencia logró ser aplicada como un método clave para la detección del inicio de las fases efusivas, especialmente en áreas remotas y/o muy nubladas, proporcionando una herramienta adicional de advertencia efectiva o para la evaluación de peligros y sus riesgos en tiempo casi real. Finalmente, gracias al análisis sismológico y los resultados obtenidos, se logró mostrar con detalles sin precedentes, la evolución espacio-temporal de la sismicidad durante una gran erupción silícea. De igual modo se logró identificar el reservorio magmático principal, definir un modelo 1D de velocidad locales y analizar una serie de procesos subyacentes asociados con el tránsito/ascenso de magmas silíceos (sismicidad tipo no doble cupla [NDC]), con énfasis en el posible papel que podrían tener las estructuras del basamento para permitir el alojamiento y posterior ascenso de magma a alta presión, provocando el desarrollo de un tremor quasi-armónico en la fase Efusiva, seguidos por una importante subsidencia y reactivación de fallas locales asociadas al SFLO durante la evacuación de magma y gases volcánicos, en uno de los fenómenos volcánicos más violentos y peligrosos de la naturaleza.
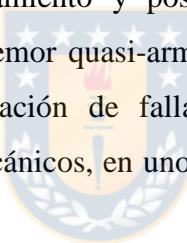
Abstract

The explosive siliceous eruptions are one of the most dangerous natural phenomena, however, few knowledge is available about the precursor processes that follow this kind of eruptions, because of they are unusual phenomena. Only three eruptions of this type had been recorded worldwide in the last century (Novarupta Katmai 1912, Chaitén 2008 and Puyehue Cordón Caulle 2011 volcanoes). In this thesis, we present the first systematic characterization that occurs before, during and after a large siliceous eruption, analyzing geophysical data recorded in the Puyehue Cordón Caulle Volcanic Complex (PCCVC) during the rhyolitic eruption VEI = 4 generated on June 4th, 2011. Most of data were recorded by the Southern Andes Volcanological Observatory (OVDAS) network. The reprocessing of the analyzed seismic data during the eruptive cycle was carried out two years after the eruption, developing an exhaustive analysis of seismic inversion, focal mechanisms, a time series of b-value and the relocation of hypocenters generated due to a new 1D local velocity model. It was also possible to describe the spatial-temporal evolution of the seismicity during the volcanic crisis, identifying the main structures that controlled the eruption. Taking into account this extensive and detailed reprocessing data, it was possible to identify two major phases during the crisis registered in 2011 (pre-eruptive and post-eruptive), which were described and analyzed in detail. After the eruption, Wendt et al. (2016) detected a deformation of the surface at a metric scale, which was observed by a series of Envisat ASAR satellites and a time series of two continuous GPS stations. In addition, the deformation described before, during and after the eruption was modeled, identifying several points and dike sources, which were distributed aligned along the Cordón Caulle Graben. The GPS observations near the volcanic complex showed an additional local effect, due to the seismic reactivation of the Liquiñe-Ofqui Fault System (LOFS) southeast of the PCCVC during the eruption. The volcanic co-eruptive deformation was consistent with the seismic migration, which was concentrated mainly along the Cordón Caulle Graben (strike NW) and in the eastern zone, where it is intercepted with the LOFS (strike NNE), place where the eruption of 2011 was finally located. On June 15th, the Effusive Phase of the eruption began, and it was recorded by the analysis of satellite images performed by Bertín et al. (2015). These images, allowed to corroborate that high emission rates in siliceous lavas are more frequent than we thought, particularly during the initial eruptive stages. The accelerated rates of the viscous lavas generated a special seismic tremor kind, called quasi-harmonic, which was used to establish a relationship between this tremor

and the velocity of emission lavas at the surface. Such correspondence managed to be used as a key method for the detection of the beginning of the effusive phases. Especially in remote and/or very cloudy areas, providing an additional tool of effective warning or for the evaluation of hazards and their risks in real time. Finally, our seismic results shown with unprecedented details, the spatio-temporal evolution of the seismicity during a evolution of a large siliceous eruption. Likewise, it was possible to identify the main magmatic reservoir, define a 1D local velocity model and achieving identify a series of underlying processes related with the migration/rise of siliceous magmas (non-double-couple seismicity [NDC]). On this way, we achieve identify the possible role that the basement structures could have to allow the lodging and later rise of magma at high pressures, causing the development of a quasi-harmonic tremor in the phase Effusive, followed by an important subsidence (fast *b-value* seismic change in the PCCVC) and reactivation of local faults related with SFLO during the evacuation of volcanic gases and magmas, in one of the most violent and dangerous volcanic phenomena of nature.

Tabla de contenidos

Índice de Figuras

Índice de Tablas

CAPÍTULO I: Introducción General

1.1 Introducción

Ubicado entre las regiones de Los Lagos y Los Ríos, el Complejo Volcánico Puyehue Cordón Caulle (CVPCC, 40.524° latitud S y 72.178° longitud W) forma parte del Segmento Central de la Zona Volcánica Sur (CSVZ por sus siglas en inglés; Stern 2004), sección del arco volcánico controlado por el Sistema de falla Liquiñe-Ofqui (SFLO). Esta última es considerada como una falla de rumbo generada debido a la subducción oblicua entre la placa de Nazca y la placa Sudamericana (Lavenu y Cembrano 1999; Lange et al., 2008; Cembrano y Lara, 2009; Legrand et al., 2011; Vargas et al., 2013). La extensa gama composicional de magmas para el CVPCC (basaltos a riolitas) generados por los numerosos centros eruptivos alineados en sentido NW-SE (Caldera Cordillera Nevada [CCN], volcán fisural Cordón Caulle [VCC] y Volcán Puyehue [VP]) durante el Pleistoceno Superior y Holoceno, han permitido definirlo como un gran complejo volcánico (Lara y Moreno 2006, Singer et al., 2008). Sin embargo, durante las últimas tres erupciones históricas (1921-1922; 1960 y 2011; VEI 3-4), el análisis petrológico en lavas/piroclastos no ha mostrado variaciones composicionales significativas, sugiriendo una génesis y un reservorio magmático en común (Singer et al., 2008; Silva et al., 2011; Castro et al., 2013, Jay et al., 2014). Si bien Alloway et al., 2015 describe sutiles diferencias composicionales para la erupción del 2011, dicho autor propone alojamientos magmáticos individuales en la fase final de la crisis volcánica de 2011, asociados con una serie de diques alimentadores alineados con la estructura principal del graben. Un rasgo poco habitual asociado a erupciones silíceas (riodacítica 68-75% $SiO2$), fue el marcado carácter fisural que tuvieron las erupciones registradas en 1921-1922 y 1960, evidenciando un importante control estructural predominante NW-SE (Lara et al., 2004-2006a), configuración que en superficie ha dado lugar a la formación de un graben elongado de 14x6 km en esta dirección (Lara y Moreno 2006). Sin lugar a dudas, este complejo a mostrado erupciones poco habituales, no obstante, el caso más particular fue la erupción registrada el 24 de

mayo de 1960, ya que tanto Barrientos (1994) como Lara et al., (2004) atribuyen dicha erupción a una extensión cosísmica del arco volcánico (2 m en el sector del CVPCC) provocada por el terremoto Mw:9,5 ocurrido en Valdivia, fenómeno que habría reactivado numerosas fallas en el arco volcánico, favoreciendo el ascenso de magmas. Finalmente, el alojamiento y posterior dinámica del ascenso de magmas silíceos en la corteza superior aún sigue siendo poco conocida, no obstante, el carácter poco profundo de las cámaras magmáticas (<10km) y la alta concentración de volátiles, facilitan el rápido ascenso de estos magmas a través de diques/fallas (Castro & Dingwell 2009), gatillando en el proceso final de desestabilización, el desarrollo de numerosos enjambres sísmicos (señales precursoras) con importantes magnitudes ($Ml>4,0$) como fue el caso de la erupción que se registró el 04 de junio de 2011. Debido a que este compejo volcánico tiene evidencias de activación gatillados por grandes terremotos, en marzo de 2010 se le suguirió a la jefatura del Observatorio Volcanológico de los Andes del Sur (OVDAS) instalar una red sismológica más densa. Gracias a la enorme data sísmica recopilada durante la crisis volcánica registrada en el CVPCC en 2011, se decidió realizar una investigación que pretendiera responder las grandes interrogantes que hay en el mundo científico relacionado con las erupciones riolíticas, como por ejemplo la relación estructural que existe con el o los reservorios magmáticos, el ascenso/migración de magmas, el mecanismo de erupción y finalmente identificar evidencias precursoras que permitan establecer diferentes alertas volcánicas ante erupciones tan violentas como las generadas por magmas silíceos.

1.2 Planteamiento del trabajo de investigación e hipótesis

Las erupciones volcánicas silícicas son uno de los peligros naturales más devastadores ya que se asocian comúnmente con la evacuación explosiva y violenta del magma rico en volátiles. Las erupciones explosivas con alto contenido de sílice no son frecuentes, no obstante, esta últimas están asociadas con algunos de los desastres naturales más grandes en la historia humana (por ejemplo, Vesuvius 79, Llopango 429,

Unzen 1792, Tambora 2015, Krakatau 1883, Mt Pelée 1902, Pinatubo 1991). Debido al extenso arco volcánico chileno y su compleja evolución magmática, en la última década se han podido registrar dos de las tres erupciones riolíticas generadas en el último siglo (Novarupta-Katmai 1912, Chaitén 2008 y Cordón Caulle 2011). Especial relevancia tiene esta última, debido a que ha sido la única erupción que ha podido ser registrada en detalle con una red geofísica local, dando la posibilidad de poder estudiar y comprender el desarrollo de estas potenciales grandes erupciones. Variaciones locales del estrés a nivel cortical generadas por grandes terremotos o producto de una importante migración/ascenso de magmas han sido ampliamente documentado por varios autores (King et al., 1994; Mikumo et al., 2001; Roman et al., 2004; Roman et al., 2006; Roman & Cashman, 2006; Roman & Heron, 2007; Bonali et al., 2012), provocando una rotación en la distribución de los esfuerzos locales, facilitando la reactivación de nuevas fallas, y con ello la migración/ascenso de nuevos pulsos magmáticos y la aparición de enjambres sísmicos. Otros autores (Harris, 2000; Brodsky et al., 2003; Brodsky & Prejean, 2005; Manga & Brodsky, 2006), han señalado que es posible generar un cambio del estrés local relacionado con una sobrepresión en cámaras magmáticas silíceas someras provocado por el paso de ondas superficiales (*dynamic stress*). Para el caso particular del Complejo Volcánico Puyehue Cordón Caulle (CVPCC), Barrientos (1994) y Lara et al., (2004) sugieren que la erupción registrada el 24 de mayo de 1960 fue gatillada debido a una extensión cosísmica de la corteza continental (2 m en el sector del CVPCC) provocada por el terremoto Mw9.5 ocurrido en Valdivia, posicionando este volcán a nivel mundial debido a la evidente interacción entre un terremoto y una posterior erupción (36 horas de diferencia). Si bien la controversia existe debido a el o los fenómenos que pudieron gatillar la erupción del CVPCC registrada el 04 de junio de 2011, los datos sismológicos y geofísicos obtenidos antes y después de la erupción permiten acotar dicho abanico. De esta forma, se plantea la siguiente hipótesis de trabajo: **La erupción del CVPCC durante el año 2011 fue generada por un cambio de estrés local (fenómeno precursor) provocado por una sobrepresión de fluidos magmáticos bajo el cordón fisural Cordón Caulle, gatillando la reactivación de las**

principales estructuras como el graben (NW) y la SFLO (NNE). Dicha hipótesis tratará de ser abordada con datos geofísicos generados en la erupción del Complejo Volcánico Cordón Caulle, registrada por OVDAS durante el año 2010-2014 y datos de GPS otorgados por la Universidad de Concepción. De igual forma, se desarrollará un completo análisis bibliográfico relacionado con trabajos geológicos y tectónicos publicados en la zona de estudio, esto con el fin de poder complementar la información geofísica analizada y poder caracterizar tanto el ambiente tectónico regional como las variaciones locales atribuidas a la erupción del CVPCC durante el año 2011 y así poder comprender la dinámica que se desarrolla antes, durante y después de esta importante erupcion silícea.

1.2.1 Objetivos

De acuerdo con el análisis y discusión desarrollada a la fecha, se han planteado varias inquietudes relacionadas con la erupción de este complejo volcánico y esperamos que esta investigación las pueda responder:
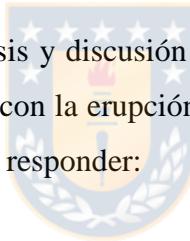
- ➢ ¿Qué tipo de actividad sísmica está asociada con intrusiones de magmas silíceos?
- ➢ ¿Dónde y a qué profundidad se localiza el/los reservorios magmáticos principales?
- ➢ ¿Cuáles estructuras controlaron la migración y/o ascenso de fluidos magmáticos?
- ➢ ¿Cómo se orientan los esfuerzos principales durante las fases pre y post eruptivas?

1.2.2 Objetivo general

Comprender la dinámica de una erupción riolítica en el CVPCC y su relación con el marco geológico y tectónico tanto local como regional.

1.2.3 Objetivos específicos

➤ Caracterizar las fuentes sísmicas del CVCC, identificando el reservorio magmático y las estructuras que participaron en la migración de fluidos magmáticos y posterior erupción.

➤ Identificar las orientaciones de los esfuerzos principales involucrados durante las fases pre y post eruptivas y cómo estas se relacionan con la dinámica regional.

➤ Determinar la estructura interna del CVCC a través de la actividad sísmica, integrando los resultados obtenidos con la geodesia satelital publicada por Bertín et al. (2015) y Wendt et al. (2016).

1.3 Marco tectónico y geológico regional

Desde hace 5 Ma (Millones de años), el vector de movimiento de la placa de Nazca se ha mantenido relativamente constante, con un ángulo oblicuo de 22 ° (N78ºE) en relación al ángulo normal a la fosa, con una tasa de convergencia de 65 a 110 mm/año (Pardo-Casas y Molnar, 1987). En base a los datos cinemáticos y sísmicos, propuestos por Lavenu & Cembrano (1999), estos autores describieron dos direcciones tectónicas principales compresivas que gobernaron la zona del intra-arco volcánico entre los 37ºS a 42ºS desde el Mioceno al presente. El primero fue descrito como de tipo compresional, abarcando desde el Mioceno Tardío al Plioceno (entre 8,2 y 1,6 Ma), con un σ1 en dirección E-W. El segundo evento, que abarcó principalmente el Cuaternario (1,6 Ma) fue descrito de tipo transpresional dextral con una orientación σ1 NE-WS. En este último período, en el arco volcánico se han generado dos tipos principales de volcanismo, uno con predominancia félsica, con un dominio en las estructuras NW (ejemplo: CVPCC); y por otro lado un volcanismo más máfico, con un dominio estructural de dirección NNE/NE (ejemplo: Carrán los Venados), sugiriendo que los dominios NW poseen un régimen compresional en su naturaleza, lo que favorece el alojamiento de magmas con una larga residencia y diferenciación magmática, en contraste con las estructuras extensionales NNE/NE, las que a diferencia del primero,

favorecen el rápido ascenso de magmas predominantemente básicos y de orígenes más profundos (Cembrano & Moreno 1994). Sin embargo, la segmentación del arco magmático a lo largo de Chile también es consecuencia del cambio en el espesor cortical (70 km en el Zona Volcánica Central [ZVC] v/s 35 km a lo largo de la Zona Volcánica Sur [ZVS]) y su correspondiente composición predominantemente félsicas en la ZVC, en contraste con un origen de afinidad más máfica que predomina en la ZVS (Tassara y Yanez 2003).

Estructuralmente, el SFLO está representada por una estructura de primer orden, de unos 1000 km de longitud un rumbo NNE, generando un carácter anisotrópico a lo largo de la ZVS (Cembrano et al., 1996; Cembrano et al., 2000; Cembrano et al., 2002), controlando todo el arco volcánico cuaternario (39ºS - 46ºS). En una escala más local, la ZVS se cruza con anisotropías de segundo orden (oblicuas), con orientaciones NW y NE (Sanchez et al., 2013; Pérez-Flores et al., 2016). Algunos estratovolcanes como el Villarrica, CVPCC y Casablanca (39ºS y 40ºS) se localizan en el cruce entre el arco paralelo y estas estructuras oblicuas secundarias. Anisotropías de rumbo NW (Fallas transversales Andinas [FTA], [Sanchez et al., 2013]) se han atribuido a estructuras antiguas heredadas del basamento (Figura 1.3.1 y figura 1.3.2), generados antes de Ciclo Andino Cenozoico (Cembrano y Moreno, 1994). Sin embargo, no solo el volcanismo activo responde a este tipo de estructuras heredadas; Munizaga et al. (1988) entre las latitudes 39ºS y 42ºS sugieren la existencia de cinturones plutónicos orientados con rumbos NW, todos ellos originados desde fines del Paleozoico al Jurásico. Finalmente, estructura NW del CVPCC se extiende al noroeste a través del Valle Iculpe, más allá del perímetro asociado al volcanismo Cuaternario, indicando la existencia de un volcanismo pre-Cuaternario más antiguo.

Legend

- Basement rocks
- Quaternary (laharic, alluvial, fluvial, glacial)

Quaternary volcanic rocks

Mecheca
- Pre-intra-post glacial basalt

Carran-Los Venados
- Intra-post-glacial/historic basalt

Cordillera Nevada
- Pre-intra-glacial basalt

Cordon Caulle
- Pre-intra glacial basalt
- Post-glacial/historic dacite-rhyolite

Puyehue
- Pre-intra-glacial basalt
- Post-glacial andesite-dacite
- Post-glacial pyroclastic

Casablanca-Antillanca
- Intra-post-glacial basalt

- Lake water
- Thermal manifestations
- Fault/lineament/alignment

LAKE RANCO · ICULPE 120 ± 30 ka · NEVADA 117 ± 15 Ka · CORDON CAULLE · CORDILLERA NEVADA · LOFZ · INT 5.44 ± 0.02 Ma · LAKE LLIFUE · LICAN 200 ± 40 ka · PUYEHUE 310 ± 20 ka · PUYEHUE VOLCANO · LAKE PUYEHUE · PUYEHUE-AGUAS CALIENTES HOT SPRINGS · CASABLANCA VOLCANO · LAKE RUPANCO · 0 5 km · N · 72°20' · 72°10' · 40°20' · 40°40'

Figura 1.3.1 Mapa geológico y estructural de Moreno 1977. Fuente: Sepúlveda et al., 2005.

El control estructural y los ascensos magmáticos son claves para poder comprender no solo la evolución de los magmas, también los posibles estilos eruptivos en un extenso arco volcánico como es la Cordillera de los Andes. Al asumir que la propagación de diques andersonianos son favorables a lo largo de grietas orientadas con un σ3 perpendicular (Emerman y Marret, 1990), alineaciones de centros monogenéticos se pueden utilizar para rastrear la disposición de los esfuerzos existente al momento de una erupción. En dicho contexto, la estructura NW del CVPCC y sus conos de pómez serían coherentes con un "modelo extensional" solo en el período cosísmico asociado

con un gran terremoto de subducción, donde σ2 y σ3 estarían configurados en una posición horizontal, con una orientación σ3 NE (Sepúlveda., et al 2005). Dicha configuración se habría producido para la erupción de 1960. La dirección del mínimo esfuerzo horizontal (σ3) generada por el terremoto de Valdivia Mw:9,5 fue instantánea y se orientó aproximadamente en la misma dirección de convergencia de las placas pero en el sentido opuesto (N78ºE), produciendo una posible reactivación dextral (?) a lo largo de la fisura del graben del CVPCC (Lara et al., 2004). No obstante, indicadores cinemáticos dextrales no se han documentado a lo largo de la fisura del CVPCC. La hipótesis de Cembrano y Moreno (1994) relacionada con un dominio compresional para lavas siliceas y el estrés regional (transpresional dextral con σ1 orientado hacia el NE) evidencian una coexistencia de dos regímenes diferentes para el CVPCC. Klotz et al. (2001) y Sepúlveda et al. (2005) interpretan esta dualidad tensional como un ciclo de deformación Andina generada por grandes terremotos la que estaría relacionada con una deformación extensional coseismica (rebote elástico), y luego con una deformación transpresión en el período intersísmico. Sepúlveda et al. (2005) sostiene que un régimen dual de estrés es consistente con el ciclo de terremotos que domina la deformación de la corteza. En el CVPCC, los períodos de acortamiento elástico inter-sísmicos en la dirección de convergencia de la placa favorecería un estancamiento de magmas y la diferenciación de este, y por otro lado, los períodos de deformación cosísmica inducida por terremotos a gran escala, podrían inducir extensión y ascenso de magmas o movilización de fluidos. Finalmente, el hecho de que se producen a lo largo de arcos volcánicos activos de márgenes convergentes (compresión en un sentido amplio) llevó a que Nakamura (1977) afirmara que la tectónica global de arcos volcánicos deben ser preferentemente del tipo strike-slip (σ1 y σ3 horizontal, σ2 vertical), en lugar de compresionales (σ1 y σ2 horizontal; σ3 vertical). Esto permitiría que el magma ascienda a través de diques verticales que tienen una dirección preferencial paralela a σHmax (Nakamura y Uyeda, 1980). Un trabajo más reciente sobre la relación de causalidad entre tectónica y volcánica (por ejemplo Bellier y Sébrier, 1994; Tibaldi, 1995; Dhont et al. 1998) han puesto en evidencia la estrecha relación espacial y temporal existente entre

volcanes y cuencas pull-apart, favoreciendo la formación de fracturas de tensión y cizallas tipo Riedel, dentro de zonas con predominio de deformación tipo strike-slip. Cabe destacar que las publicaciones sobre mecanismos focales para terremotos corticales generados en arcos volcánicos (Cembrano y Lara, 2009), muestran que la deformación tipo cizalle predomina sobre la demás (compresión, fallas inversas o extensión, fallas normales).
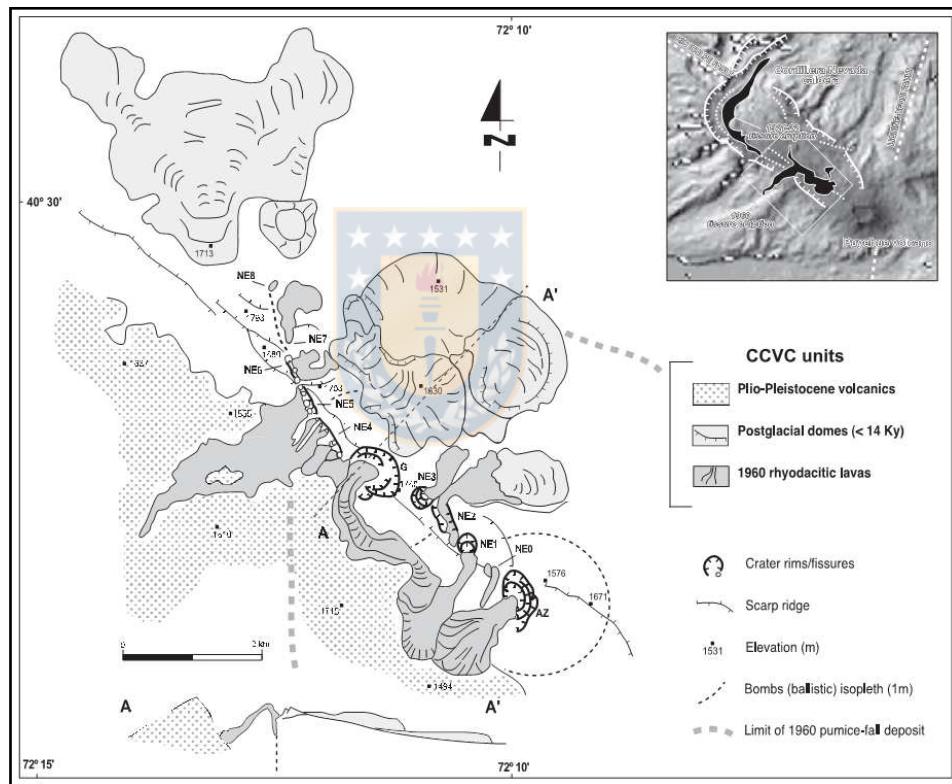
Figura 1.3.2 Mapa estructural erupción 1960. Fuente: Lara et al., (2004).

1.4 Geología local

El basamento del CVPCC está conformado, en parte, por rocas intrusivas, las que afloran relativamente de forma continua a lo largo y adyacentes al SFLO entre los 39,5°-40,5°S con edades entre 20-5 Ma (Campos et al., 1998 en Sepúlveda, 2006). Hacia el norte del CVPCC, a lo largo de la ribera del Lago Ranco, el basamento es más

heterogéneo, incluyendo cuerpos intrusivos Paleozoicos asignados al Batolito Futrono-Riñihue (Campos et al., 1998) y rocas estratificadas. Parte de estas rocas estratificadas son asignadas al Complejo Metamórfico Trafún (Devónico-Carbonífero Inferior), compuestas de rocas sedimentarias con un bajo grado de metamorfismo. De igual forma en la ribera del Lago Ranco se encuentran los Estratos de Lago Ranco (Oligoceno-Mioceno Inferior), los que corresponden a una secuencia sedimentaria y volcánica de composición intermedia continental con algunas intercalaciones marinas. Incluye ignimbritas, areniscas volcanoclásticas y lutitas plantíferas, en algunas de las cuales se observan lentes de pirita. Los Estratos de Pitreño (Mioceno Superior-Plioceno) afloran en la parte alta de los farellones de la ribera sur del Lago Ranco, como una secuencia volcánica y sedimentaria continental subhorizontal apoyada discordantemente sobre los Estratos de Lago Ranco, el Batolito Futrono-Riñihue y el Complejo Metamórfico Trafún (Sepúlveda, 2006).
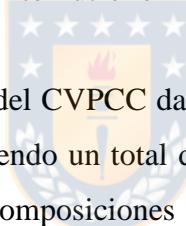
Las rocas más antiguas del CVPCC datan de unos 315 ka (Pleistoceno Superior; Singer et al., 2008), comprendiendo un total de 148 km^3 que forman parte del CVPCC (Sepúlveda et al., 2005), con composiciones que van desde basaltos y andesitas hasta riolitas (Campos et al., 1998; Lara et al., 2001), enfatizando el comportamiento bimodal del sistema, donde destacan los basaltos (en su base, más antiguas) sobre las lavas ricas en sílice (más someras y jóvenes). La geología del CVPCC se encuentra detallada el en mapa geológico escala 1:50.000 publicado por Sernageomin (Lara y Moreno 2006).

1.4.1 Caldera Cordillera Nevada

La Caldera Cordillera Nevada (CCN) fue un volcán de escudo colapsado cuyos productos (andesitas basálticas a dacitas) cubrieron un área de 700 km^2 al NW del CVPCC. La caldera resultante del colapso de este volcán tiene un diámetro de 8.5 Km con una apertura al sureste, desde donde el graben se extiende siguiendo esta orientación hasta el volcán Puyehue (Lara et al., 2006). Las rocas y sus edades se pueden resumir de la siguiente forma:

1.4.1.1 Volcanismo pre-caldera

Cordillera Nevada I (cn1): Escudo basal (>377 ka)

Esta unidad posee gruesas sucesiones volcánicas, radiales y suaves formadas por flujos de lavas andesítico-basálticas, gravas y con escasas ignimbritas máficas cristalinas, localmente soldadas. Esta secuencia alcanza unos 200 km de espesor en algunos valles glaciares (Lara et al., 2006). La edad de esta unidad fue determinada por Lara et al. (2001), quienes establecieron por dataciones ^{40}Ar/^{39}Ar que pertenece al Pleistoceno Medio con una edad de 377±7 ka.

Cordillera Nevada II (cn2): Escudo superior (377-117 Ka)

Es la sección más joven de las secuencias pre-caldera la cual está representada por secuencias volcánicas que cubren parcialmente el escudo basal glacialmente erodado y se produce como gruesos flujos de lava estancada dentro del valle glacial principal del río Iculpe, las lavas de esta unidad son dominantemente andesítico-basálticas (Lara et al., 2006). Sepúlveda et al., (2005) determinaron por dataciones ^{40}Ar/^{39}Ar que la parte superior de la secuencia pre-caldera tiene una edad de 117±15 ka.

Ignimbrita San Pablo y caldera de colapso

Es una sucesión volcanoclástica reconocida en los valles al oeste del CVPCC y cruza todo el ancho del valle central. Ésta cubre un área de 1500 km^2 con un grosor de aproximadamente 1 m cerca de la ciudad de Osorno, 80 km al Oeste del CVPCC. Adicionalmente a esta distancia del CVPCC, presenta un canal de este flujo piroclástico de 70 m de grosor en los valles de río Pilmaquén y río Bueno. La facies distal de la Ignimbrita San Pablo está caracterizada por ser una unidad masiva, sin estructuras sedimentarias, compuesta de pumitas y escasos piroclástos de escoria en una fina matriz de ceniza amarillenta y se encuentra ampliamente cubierta por los depósitos de la Glaciación Llanquihue (90-32 ka; Clapperton, 1993). En los valles principales la Ignimbrita San Pablo cubre a la penúltima glaciación llamada Santa María (262-132 ka; Clapperton, 1993). Un depósito de toba de lapilli se encuentra sobre la Ignimbrita San Pablo, la cual es enterrada por una sucesión epiclástica de materiales piroclásticos reelaborados. En su parte superior se depositan limos, arenas y gravas relacionados con el Último Máximo Glacial (LGM son sus siglas en inglés, por Last Glacial Maximum),

estos depósitos forman el principal acuífero en el valle central. Del total del área cubierta por la Ignimbrita San Pablo se puede decir que su volumen es de aproximadamente 15 km^3 (Lara et al., 2006). La Ignimbrita San Pablo se depositó entre la penúltima y última glaciación. La penúltima glaciación termina alrededor de los 132 ka y la última glaciación tiene lugar entre los 90-32 ka (Clapperton 1993), por ende se sugiere que la Ignimbrita San Pablo se formó después del término de la penúltima glaciación (132 ka) pero antes del comienzo de la última glaciación (90 ka).

1.4.1.2 Volcanismo post-caldera

Cordillera Nevada III (cn3): Relleno parcial de la caldera (< 117 ka)

Esta unidad surge como un relleno de la caldera compuesto por lavas andesíticas probablemente provenientes del anillo de fallas que se forma una vez colapsado el volcán Cordillera Nevada (Lara et al., 2006). La edad determinada por Sepúlveda et al. (2005) en andesitas del Valle del río Nilahue por el método 40Ar/39Ar fue de 110±30 ka.

Cordillera Nevada IV (cn4): Actividad tardía del anillo de fallas (< 40 ka?)

Está compuesta por lavas andesíticas a dacíticas que son extruidas desde el anillo de fallas. Los flujos de lava de esta unidad son erodados por glaciares, algunos muestran estrías en su superficie. Esta unidad es equivalente a la unidad cc3 del Cordón Caulle, ambos representan una etapa post-colapso con dominantes erupciones fisurales en la sección norte del CVPCC. Dataciones pobres se obtuvieron de un plateau andesítico en el muro este de la caldera a través de dataciones ^{40}Ar/^{39}Ar obteniendo una edad de 25±15 ka (Lara et al., 2006).

1.4.2 Sistema fisural Cordón Caulle

El cordón Caulle es un sistema fisural que mide 9 km de largo y 4 km de ancho, este sistema contiene un graben asimétrico definido por dos escarpes de tendencia NW. Dentro de éste se encuentran depósitos volcánicos dacíticos y riolíticos (lavas, domos, depósitos de flujos piroclásticos, conos de escoria y depósitos de caídas de cenizas

[tefras]; Singer et al., 2008), todos ellos acumulados durante la fase terminal de la última glaciación (16.500-12.000 AP: Antes del Presente) y la fase post-glaciar, Holoceno (últimos 11.700 años AP).

1.4.2.1 Secuencia pre-graben

Cordón Caulle I (cc1): Complejo de escudo oriental (>430 ka)

Esta unidad se extiende al NE como un conjunto de lavas silícicas, ignimbritas soldadas, alfeizares, sills, lacolitos y gruesos caminos de gravas yuxtapuestos a las lavas pre-caldera de los volcanes Cordillera Nevada y Mencheca. Edades ^{40}Ar/^{39}Ar de 430±60 ka fueron obtenidas de lavas dacíticas de la parte superior de esta unidad (Lara et al., 2006).

Cordón Caulle II (cc2): Escudo a transición fisural (aprox. 300-70 ka)

La segunda unidad es Cordón Caulle 2 (cc2) la cual es reconocida en dos secuencias de lavas aisladas que presentan diferentes alimentadores. La secuencia oeste (cc2w) es dividida por el arroyo Licán en dos pilas volcánicas. La pila norte es una sucesión de 60 m de espesor con un escarpe cóncavo hacia el NE, esta brota de la unidad Cordillera Nevada 1 (cn1) y tiene profundas incisiones glaciares. Brechas piroclásticas y flujo de detritos con matriz oxidada y lavas andesíticas son expuestos en el escarpe principal, donde diques andesítico-basálticos y sills intruyen. Los diques en la parte baja de la secuencia tienen una edad de entre 173-167 ka. La pila sur es una suite de lavas y rocas piroclásticas de 150 m de espesor en la pared que forma un escarpe subvertical. Lavas, brechas e ignimbritas máficas masivas son subhorizontales o ligeramente deflectadas alrededor del lacolito que las intruye. Diques basálticos verticales cortan esta sucuencia (Lara et al., 2006). La secuencia este (cc2e) es una sucesión de 120 m de espesor que cubre en inconformidad a la unidad cc1. Esta secuencia forma un escarpe cóncavo de 8 km de largo y abierto al oeste, está compuesto por lavas dacíticas que se sumergen al este y son cortadas por los domos y sills dacíticos. En general la secuencia muestra una tendencia de las fallas NW y además es intruida por diques basálticos (Lara et al., 2006). La edad ^{40}Ar/^{39}Ar de un flujo basal de lava determinada por Sepúlveda et al. (2005) fue de 300±20 ka cerca del lago Puyehue, una edad ^{40}Ar/^{39}Ar de 74±18 ka fue obtenida para

un lacolito usando laser de CO_2 por SERNAGEOMIN, adicionalmente se dató por el mismo método dos flujos de lavas dacíticas donde se obtuvieron edades de 70±20 ka (Lara et al., 2006).

1.4.2.2 Volcanismo fisural intra-graben (<70 ka-presente)

<u>Cordón Caulle III (cc3): Ignimbritas y lavas (<70 ka)</u>

Esta unidad corresponde a ignimbritas parcialmente soldadas, masivas o con estructuras sedimentarias débiles, junto con lavas dacíticas forman paquetes que pueden alcanzar 250 m de espesor. Esta unidad rellena el graben y las capas más externas muestran un manteo "dentro" del graben donde en la parte interna pasan a ser subhorizontales (Lara et al., 2006). En el sector sur estas coladas de lava sobreyacen a cc2 y son intruidas por diques y sills de aprox. 54-32 ka (Harper, 2003 en Lara et al., 2006).

<u>Cordón Caulle IV (cc4): Domos y coulées intra-postglacial (<32 ka)</u>

En esta unidad se encuentra la primera generación de domos y coulées que se hallan en el centro del graben. Estos son principalmente dacíticos y tienen un aspecto elongado en dirección NW. Ellos muestran una superficie de erosión en los flancos y tienen una cubierta de depósitos piroclásticos y edades $^{40}Ar/^{39}Ar$ de 16.5±3.8 ka fueron obtenidas para estos (Lara et al., 2006).

<u>Cordón Caulle V (cc5): Domos y coulées postglaciares (Holoceno)</u>

Esta unidad comprende la suite más joven de domos y lava-domos dacíticas a riolíticas dentro del graben. Un gran lava-domo ubicado cerca del escarpe del graben se formó en el sector NW cuya lava invade la Caldera Cordillera Nevada. Dos coulées riodacíticos localizados en la parte central del graben fueron emitidos desde vents localizados en la parte más sur del escarpe. Un singular domo riolítico de 1.5 km de diámetro dentro del "cráter" se rellena como un tapón con forma de espina (Lara et al., 2006).

1.4.3 Volcán Puyehue

El volcán Puyehue (2236 m s.n.m) es un estratocono localizado al SE del Cordón Caulle. Éste cubre un área de 160 km^2 y tiene un cráter de 2.4 km de diámetro (Lara et al., 2006).

1.4.3.1 Secuencia pre-caldera (245-96 ka)

Puyehue I (p1): volcanismo de escudo

Las antiguas secuencias del volcán Puyehue son parcialmente enterradas por flujos más jóvenes o expuestos en acantilados que rodean al actual estratocono. El remanente que se encuentra en la zona más occidental es una sucesión de aproximadamente 150 m de espesor compuesto por lavas andesíticas y brechas que mantean al oeste. La sucesión oriental está compuesta por basaltos y andesitas máficas cortadas por numerosos diques (Lara et al., 2006).

1.4.3.2 Estratovolcán post-caldera (69-2.3 ka)

Puyehue II (p2): volcán englacial (69-34 ka)

Corresponde a lavas andesíticas fuertemente erosionadas en la base del presente estratocono o yuxtapuesta a la secuencia p1. En el acantilado oriental donde se encuentra p1, un complejo de andesitas máficas y afíricas son cruzadas por diques que representan la facies del vent lateral. Se obtuvieron edades de 68 y 45 ka para los flujos de lava andesíticos, adicionalmente en un flanco del Volcán Puyehue, lavas andesíticas a riolíticas presentan marcas de erosión glacial, y su edad es de 34 ka (Harper, 2003).

Puyehue III (p3): lavas tardiglaciares (19-11 ka)

Esta unidad contiene múltiples flujos de lava, de basálticas a riodacíticas con débil erosión glacial que se encuentra en el flanco occidental del volcán Puyehue. Una edad mínima para esta unidad podría estar indirectamente limitada por el retiro del hielo del Último Máximo Glacial en la orilla oriental del lago Puyehue (~190 m s.n.m), inferido por Bentley (1997) en aproximadamente 12.2 ka.

Puyehue IV (p4): lavas post-glaciares (7-2.5 ka)

La última unidad corresponde a Puyehue IV (p4) donde La mayoría de los flujos de lava riolítica y domos se encuentran en el flanco oriental del volcán Puyehue. Ellos están bien expuestos en la pared del cráter, donde al menos 150 m de riolitas vítreas están cubiertas por capas de tefra. Harper (2003) determinó una edad máxima para la formación del cráter del volcán Puyehue está dada por 6.4 ka para las riolitas del cráter, pero las lavas y

la tefra que lo cubren son considerados más jóvenes (Lara et al., 2006). Un resumen de las litologías presentes en este complejo volcánico se muestran en la Tabla 1.4.1.

Tabla 1.4.1 Resumen de litologías presentes en el Complejo Volcánico Puyehue-Cordón Caulle CVPCC. Fuente: elaboración propia.

Caldera Cordillera Nevada		Cordón Caulle		Volcán Puyehue	
Volcanismo pre-caldera	**Cordillera Nevada I(cn1):** flujos de lavas andesítico-basálticas, gravas y con escasas ignimbritas máficas cristalinas, localmente soldadas.	**Secuencias pre-graben**	**Cordón Caulle I (cc1):** conjunto de lavas silícicas, ignimbritas soldadas, alfeizares, sills, lacolitos y gruesos caminos de gravas yuxtapuestos a las lavas pre-caldera de los volcanes Cordillera Nevada y Mencheca.	**Secuencia pre-caldera**	**Puyehue I (p1):** en la zona más occidental se encuentran lavas andesíticas y brechas que mantean al oeste. La sucesión oriental está compuesta por basaltos y andesitas máficas cortadas por numerosos diques.
	Cordillera Nevada II (cn2): secuencias volcánicas que se produce como gruesos flujos de lava estancada dentro del valle glacial principal del río Iculpe, las lavas de esta unidad son dominantemente andesítico-basálticos.		**Cordón Caulle II (cc2):** brechas piroclásticas y flujo de detritos con matriz oxidada y lavas andesíticas son expuestos al oeste, al este se encuentran lavas dacíticas, y son cortadas por los domos y sills dacíticos.		
Volcanismo post-caldera	**Cordillera Nevada III (cn3):** lavas andesíticas que rellenan la caldera.	**Volcanismo fisural intra-graben**	**Cordón Caulle III (cc3):** esta unidad corresponde a ignimbritas parcialmente soldadas, masivas o con estructuras sedimentarias débiles, junto con lavas dacíticas, esta unidad rellena el graben.	**Estratovolcán post-caldera**	**Puyehue II (p2):** lavas andesíticas yuxtapuestas a la secuencia p1. En el acantilado oriental donde se encuentra p1, un complejo de andesitas máficas y afíricas son cruzadas por diques que representan la facies del vent lateral.
	Cordillera Nevada IV (cn4): lavas andesíticas a dacíticas. Esta unidad es equivalente a la unidad cc3 del Cordón Caulle, ambos representan una etapa post-colapso con dominantes erupciones fisurales en la sección norte del CVPCC.		**Cordón Caulle IV (cc4):** primera generación de domos y coulées que se hallan en el centro del graben. Estos son principalmente dacíticos y tienen un aspecto elongado en dirección NW.		**Puyehue III (p3):** en el flanco occidental del volcán Puyehue se encuentran múltiples flujos de lava, de basálticas a riodacíticas con débil erosión glacial.
			Cordón Caulle V (cc5): comprende la suite más joven de domos y lava-domos dacíticas a riolíticas dentro del graben.		**Puyehue IV (p4):** flujos de lava riolítica, domos y capas de tefra se encuentran en los flancos del volcán y paredes del cráter respectivamente.

1.5 Estudios recientes

1.5.1 Deformación

La erupción registrada durante el año 2011 (VEI 3-4; Lara et al., 2012) fue precedida por al menos cinco años de deformación cortical (inflación, Fournier et al., 2010; Jay et al, 2014), definiendo dos zonas principales de alzamiento. La mayor fue localizada en el flanco este de la Caldera Cordillera Nevada (CCN), 11 km al W del cráter formado en 2011. El segundo alzamiento (de menores dimensiones), según los autores antes mencionados, se ubicó en el borde sureste del graben, 5 km al SSE del cráter 2011, ambas deformaciones situadas entre 5-9 km de profundidad, las cuales fueron inferidas modelando imágenes InSAR. Aunque dichos datos sugieren posibles reservorios, las limitaciones inherentes de imágenes interferométricas desplazadas en el tiempo restringen las observaciones, desconociendo el proceso que hay detrás de estas importantes deformaciones y las estructuras que podrían estar participando en los procesos de deformación (inflación-deflación), ya que las soluciones de las inversiones propuestas utilizando el modelo esférico de tipo Mogi siguen siendo las más precisas. Estudios petrológicos han permitido acotar aun más la profundidad de los reservorios modelados por InSAR, ubicándolos entre los 2.5-5 km (Castro et al., 2013) y 6-7 km (Jay et al., 2014). De igual forma, si bien dichos estudios han colaborado a dilucidar las condiciones de presión, temperatura y saturación de agua de estos reservorios magmáticos, las condiciones reológicas del medio son aún desconocidas, por lo tanto se hace relevante contar con un modelo local de velocidades que permita, por un lado, obtener buenas localizaciones, y por otro identificar zonas anómalas locales de velocidad dentro de la corteza.

1.5.2 Mediciones gravimétricas

Con el objeto de identificar la configuración estructural del CVPCC, Sepúlveda et al. (2005) llevaron a cabo un perfil gravimétrico. Con el fin de limitar mejor los intervalos de densidad, ellos utilizaron en el modelado de gravedad una densidad promedio de 2650 kg/m^3. Trabajaron además con densidades medidas para dacitas y riolitas (unidad CCIV según la nomenclatura de Moreno, 1977) con promedios de 2370 kg/m^3. Fragmentos de pómez recogidos de depósitos superficiales tuvieron densidad mucho más baja (1000 kg/m^3), no obstante, para incorporar el efecto de la compactación en profundidad para depósitos de pómez, el autor utilizó una densidad media de 1700 kg/m^3. Anomalías residuales calculadas por Sepúlveda et al. (2005) para los 3 perfiles realizados a través del CVPCC, alcanzaron unos 20 mGal en el centro de la depresión del graben. Todos los perfiles reprodujeron formas similares, con un formato tipo "U" relacionadas con las curvas residuales de dichas

anomalías. Para describirlo, el autor seleccionó el perfil central (Figura 1.5.2.1) usando un enfoque 2D. Se asumió la presencia de un cuerpo anómalo superficial (5 km de profundidad) para modelar la anomalía residual. En base a las interpretaciones geológicas y apuntando a un relleno superficial de lavas félsicas y tefra que cubre la base del complejo, este último, compuesto por basaltos densos y rocas del basamento cristalino (con un promedio densidad de 2650 kg/m3), el CVPCC mostró un contraste de densidad de 650 kg/m^3, cuya geometría se muestra en la Figura 1.4.2.1. A este modelo se le añadió un hipotético cuerpo de baja densidad de carácter hidrotermal, con un 10-15 % de porosidad y un depósito con temperaturas de 250 ℃ (Sepúlveda et al., 2004).
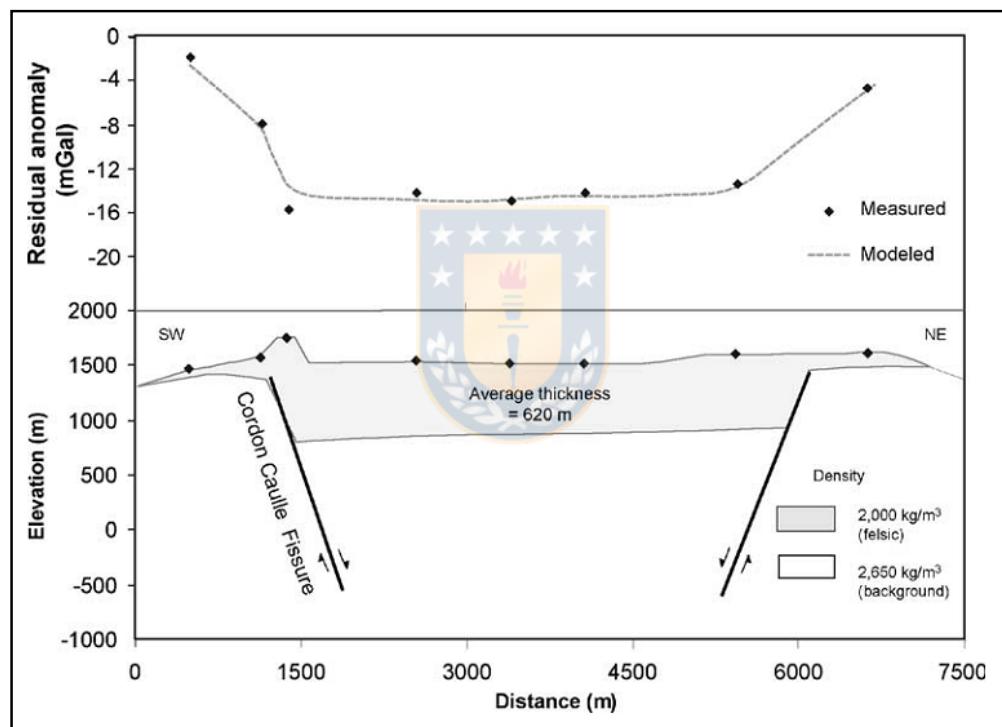
Figura 1.5.2.1 Modelo estructural del CVPCC propuesto por Sepúlveda et al. (2005). El volumen de material del CVPCC se calculó utilizando un espesor de 490 m entregado por el modelo de gravedad, y junto con el área de la depresión central, arrojó un volumen del orden del 33 km^3. Fuente: Sepúlveda et al. (2005).

1.5.3 El sistema hidrotermal del CVPCC

Los sistemas hidrotermales se componen de una fuente de calor y un reservorio donde los fluidos geotérmicos son almacenados. Los sistemas hidrotermales pueden ser dinámicos o estáticos, esto dependiendo del grado de circulación del reservorio y del mecanismo de

transferencia de calor (convección o conducción). En los sistemas dinámicos el reservorio es cargado continuamente desde la superficie, conformando un ciclo de infiltración, calentamiento y descarga superficial como fuentes termales. En este tipo de sistema hidrotermal el mecanismo de transferencia de calor es la convección inducida por la circulación de los fluidos hidrotermales. Adicionalmente, los sistemas hidrotermales se pueden clasificar como de alta entalpía (>180°C) o de baja entalpía (<180°C). Los sistemas de alta entalpía están asociados a rocas calentadas por cámaras magmáticas con un volcanismo reciente asociado (menos de 50 ka), sistemas que generalmente están asociados a márgenes de subducción, como por ejemplo el sistemas hidrotermal en el CVPCC, Chile (Sepúlveda et al., 2004). Otra forma de clasificar los sistemas hidrotermales depende de su contenido relativo de líquido y vapor, clasificándose como líquido-dominante y vapor-dominante (White, 1973). Para el caso del CVPCC, Sepúlveda (2006) lo clasificó como un sistema vapor-dominante, donde tanto el agua como el vapor coexisten en el reservorio, no obstante, el vapor es la fase principal que controla la presión del reservorio. Finalmente, este acuífero principal (primario) calienta por vapor a un segundo acuífero más somero (secundario), el que finalmente alimenta las numerosas fuentes termales que se encuentran a lo largo del complejo, destacando el mayor outflow de este sistema hidrotermal, denominado Trahuilco.
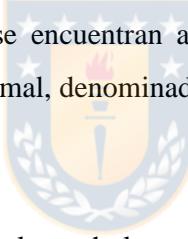
1.5.4 Estudios petrológicos

El carácter geoquímico de las lavas holocenas del graben sugieren una evolución desde un magma parental andesítico-basáltico, el que bajo un régimen tectónico transpresivo local (intra-arco) y ligado a antiguas estructuras corticales heredadas del ciclo pre-andino (rumbo NW-SE; Rapela y Pankhurst 1992; Martin et al., 1999; Melnick et al., 2003; Corbella y Lara 2008), los magmas han logrado ser retenidos, alojándose en la corteza superior (2,5-6 km), para luego mediante cristalización fraccionada, asimilación cortical y mezcla de magmas ser enriquecido tanto en sílice como en volátiles (Sepúlveda et al.,2005; Lara et al., 2006a,b; Singer et al., 2008; Cembrano et al., 2009; Castro et al., 2013, Jay et al., 2014). Aunque varios autores coinciden con una importante participación estructural tipo diques en las erupciones registradas durante el Holoceno para el CVPCC (Lara et al., 2004-2006a; Lara y Moreno 2006; Singer et al., 2008; Castro et al., 2013), ninguno de ellos ha podido cuantificar la participación de dichas estructuras en un proceso eruptivo y su relación con el o los reservorios magmáticos. Geoquímicamente, según el análisis desarrollado por Singer et al. (2008) las lavas del Cordón Caulle sugieren un carácter bimodal ya que el contenido de sílice ha ido variando (51.9% a 71.2% de SiO_2) en lavas y flujos piroclásticos en los últimos 32 ka.

Gerlach et al.,(1988) proponen que las riolítas y riodacitas derivadas del sistema fisural Cordón Caulle y el volcán Puyehue son producto de una cristalización fraccionada de basaltos con una importante asimilación cortical. Este proceso requiere de un largo tiempo de residencia. Debido a que de los magmas erupcionados en 1921-1922, 1960 y 2011-2012 son casi idénticos (dacíticos a riodacíticos), Jay et al. (2014) sugieren que derivaron del mismo reservorio, una zona rica en cristales localizada entre los 4-7 km de profundidad, donde la segregación de riodacitas ocurre. El mismo autor describe lavas con cristales de olivino rico en magnesio y plagioclasas ricas en anortita (An), determinando que este conjunto mineral no está en equilibrio con las lavas más silíceas, por ende aunque el Cordón Caulle haya erupcionado exclusivamente magma riodacítico en los últimos 100 años, magmas máficos han logrado ser capaces de llegar a la parte inferior del reservorio silícico. Según Jay et al. (2014) los cristales de plagioclasa ricas en An han estado por lo menos unos 200 años en el magma, por lo tanto, la intrusión de magma debería haber ocurrido mucho antes de la erupción del 2011, por ende, el magma máfico no fue el agente que gatilló la erupción. Finalmene estos autores proponen que hubo intrusión magmática que alcanzó la parte inferior de la cámara magmática, por lo que no se mezcló con el reservorio riodacítico pre-existente, y en lugar de ello, el nuevo magma pudo generar la deformación registrada durante el 2007-2009, al acumularse en la base del reservorio, proporcionó una fuente de calor para este (Figura 1.5.4.1). Mediciones petrológicas proponen un depósito de magma pre-existente en forma de lacolito a una profundidad de 4 a 7 km, con un área inferida de 20 km^2 que pudo haber alimentado las tres erupciones históricas más recientes (1921, 1960 y 2011). Debido a que los productos de las tres erupciones históricas poseen composiciones similares, es consistente sugerir que de este extenso reservorio es posible encontrar reservorios magmáticos más pequeños (individuales) que alimentaron las tres erupciones históricas (Alloway et al., 2015). Finalmente, intrusiones máficas en magmas silícicos también han ocurrido en el Volcán Puyehue durante los últimos 5.000 años (Singer et al., 2008), por ende este tipo de configuración podría ser consistente.
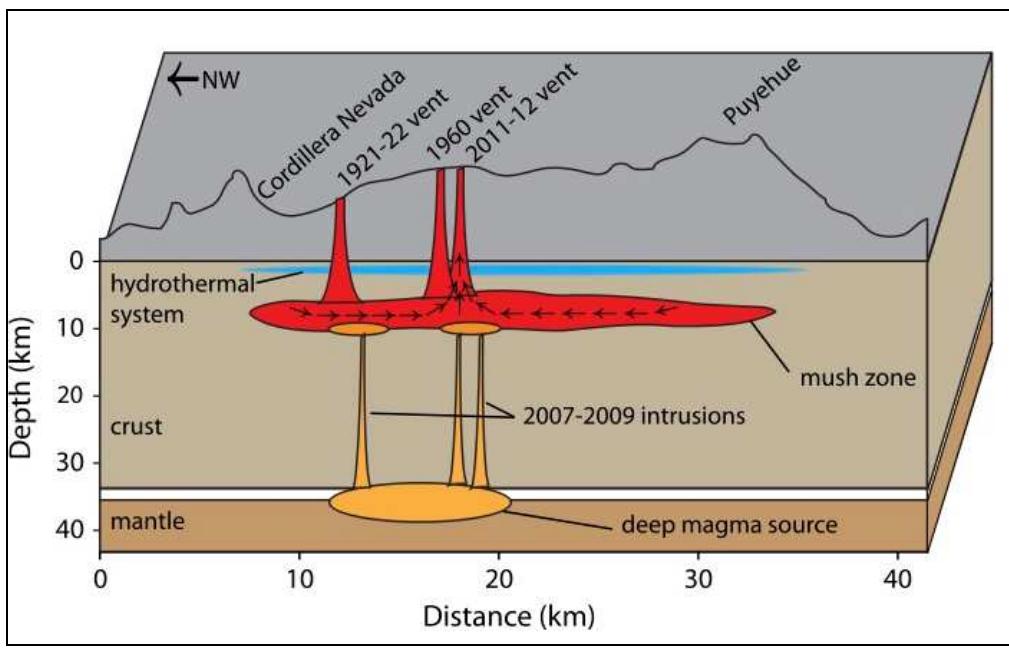
Figura 1.5.4.1 Esquema de la cámara magmática, el sistema hidrotermal e intrusiones de magma en el CVPCC. La imagen muestra un perfil topográfico NW-SE del Complejo Volcánico Puyehue-Cordón Caulle, los sitios de las últimas tres erupciones históricas, el tamaño y localización del reservorio magmático y los procesos que podrían ocurrir en profundidad. Se observa un gran cuerpo magmático rico en cristales a 4-7 km de profundidad con los conductos alimentadores de las últimas tres erupciones, el sistema hidrotermal cercano a la superficie y las posibles intrusiones de magma que pudo producir el alzamiento registrado en 2007-2009 utilizando InSAR. Fuente: Jay et al. (2014).

1.5.5 Mediciones magnetotelúricas

1.5.5.1 Introducción al modelo magnetotelúrico

La magnetotelúrica es una técnica de exploración geofísica que se basa en el fenómeno de la inducción electromagnética de origen natural para estimar la distribución de la conductividad eléctrica en el subsuelo. Las corrientes eléctricas (telúricas) que se inducen y que generan un campo magnético interno secundario, contienen variada información (amplitud y fase), de las estructuras conductoras que componen la corteza. En este capítulo se detalla de forma resumida los datos magnetotelúricos (MT) obtenidos por el Sr. Gonzalo Rojas, el alumno de pregrado del Departamento de Geofísica de la Universidad de Concepción en la campaña de terreno auspiciada por OVDAS-Sernageomin, cuyo trabajo formó parte de su tesis de grado.

1.5.5.2 Resultados

A fines de enero de 2013, se llevó a cabo la campaña de terreno que tuvo por objetivo adquirir datos MT en la zona del CVPCC, todo esto motivado por la necesidad de experimentar con el método en una zona volcánica activa y develar el control estructural que posee el cordón fisural de tipo graben que une la CCV con el VP. El modelo realizado por Gonzalo Rojas que mejor se acopló a los datos MT (figura 1.5.5.1) entregó un ajuste RMS de 1,63 [Ωm].
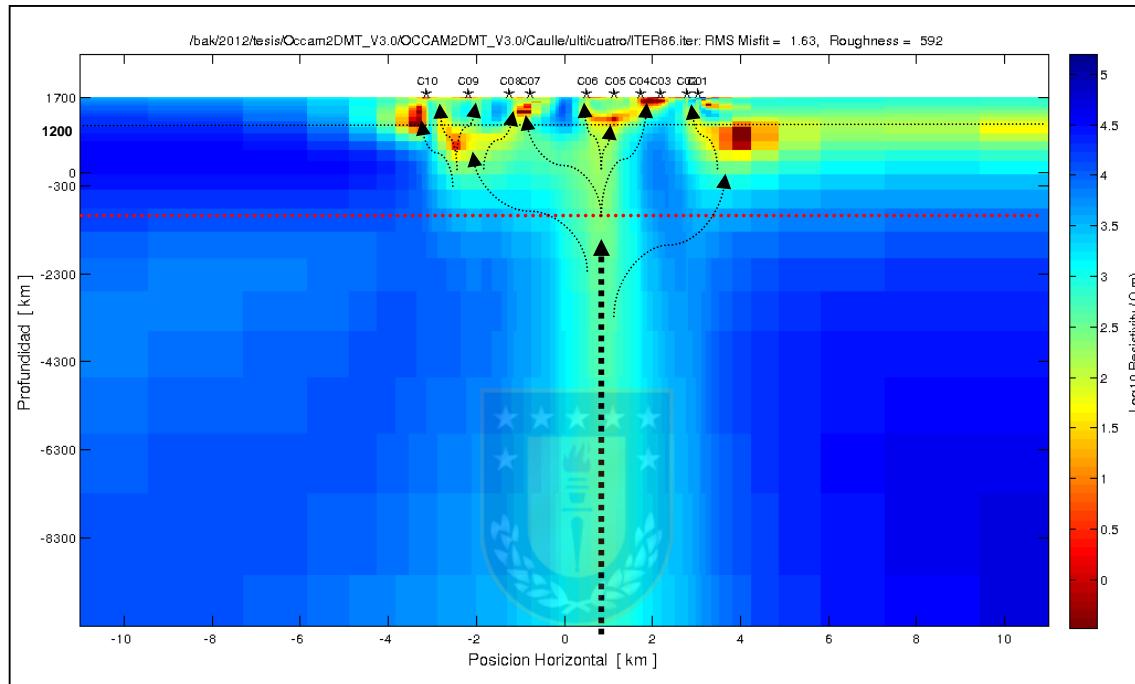
Figura 1.5.5.1 Perfil 2D MT para el CVPCC modificado por Daniel Basualto. Fuente: Tesis de grado Gonzalo Rojas 2013, Universidad de Concepción, Chile.

1.5.5.3 Discusión y conclusiones

Considerando la baja resolución del perfil MT, solo fue posible identificar estructuras de primer orden (líneas segmentadas, Figura 1.5.5.1). Uno de los principales rasgos del perfil MT es la anomalía resistiva que se localiza en la zona central del perfil [10^2,5 - 3,5 Ωm], que se extienden de forma vertical en profundidad, sugiriendo la existencia de una estructura de primer orden, la que separa dos zonas de mayor resistividad (tonos azules [10^4-5 Ωm] sectores izquierdo y derecho del perfil, figura 1.5.5.1). Esta anomalía resistiva se bifurca según nos aceramos a zonas más someras del perfil, las cuales son consistentes con una configuración de tipo graben. La estructura de primer orden podría estar controlando tanto el ascenso de magma como la circulación de fases mesotermales dentro del complejo, las que

podrían estar alimentando al sistema hidrotermal más somero. Si consideramos que el CVPCC es uno de los campos geotérmicos más importantes de la ZVS, podríamos asociar la zona de menor resistividad con sistemas de alta porosidad/permeables, facilitando la circulación de fluidos, controlando tanto el flujo de calor, como el ascenso de fluidos hidrotermales/magmáticos. En superficie, la baja resistividad en los puntos C03 y C04 coinciden con el sector denominado "Las Sopas". Este punto fue descrito e identificado en el mapa geológico de Lara y Moreno (2006), ya que presenta una profusa alteración hidrotermal producto de la circulación de fluidos hidrotermales junto con manifestaciones de aguas termales en superficie con temperaturas cercanas a los 90° C y la presencia de fumarolas ricas en H_2O-CO_2-H_2S entre otros gases. Este sitio fue destacado además por Sepúlveda et al. (2005) por ser el sector donde se extiende el lineamiento estructural de fumarolas y fuentes termales "Los Venados-Las Sopas", evidenciando un importante rasgo estructural dentro del complejo. Según los datos entregados por el perfil MT, las zonas someras de mayor resistividad presentan una potencia aproximada de unos 500 metros, valores similares a los propuestos por Sepúlveda et al., (2005) de 490 metros atribuidos a depósitos recientes descritos en el modelo de gravedad. Por otro lado, dicho autor propone una zona hidrotermal activa entre los 0 y los 2.500 metros, profundidad consistente con zonas de menor resistividad que se pueden apreciar en el perfil MT, destacándola con una línea segmentada de color rojo (Fig. 1.5.5.1). Bajo esta zona de menor resistividad, debería aflorar el basamento del CVPCC, el que podría estar conformado por: depósitos volanoclásticos más antiguos (Formación Estratos de Lago Ranco, Pitreño) o por el Batolito Patagónico Norte. Finalmente, si asumimos estos rasgos generales para la corteza superior del complejo, podríamos mencionar una primera cobertura de depósitos poco consolidados (tefras, flujos piroclástios, lahares y lavas) de unos 500 metros de espesor. Bajo esta capa, el perfil MT sugiere la existencia de unos 2000 metros de depósitos volcanoclásticos Holocenos/Cuaternarios que conforman el complejo volcánico, y finalmente bajo este, un basamento cristalino ígneo/sedimentario (?) posiblemente Mioceno. Indicios de variados xenolitos ígneos encontrados en numerosas lavas y flujos piroclásticos que afloran dentro del graben Fig. 1.5.5.2) sugerirían un basamento ígneo, el que posiblemente está siendo controlado por importantes estructuras de rumbo NW denominadas Fallas Transversales Andinas (FTA; Perez-Flores et al., 2016).

Figura 1.5.5.2 Xenolito (granodiorita) inmerso en un flujo piroclástico depositado dentro del graben del CVPCC. Fuente: elaboración propia.

1.6 Datos y métodos

1.6.1 Red geofísica

La red sísmica utilizada, y con la cual se logró pronosticar la erupción del 04 de junio de 2011, constó de 7 estaciones de banda ancha de 30 segundos (Fig. 1.6.1.1), 6 de las cuales contaban con sensores tipo Reftek151-30A, 0.03-50 *Hz*, digitalizadores Reftek 130B. Solo la estación PHU fue instalada a comienzos de 2011 con un sensor Guralp 6TD de 30 segundos, digitalizador 6TD. De un total de 7 estaciones, 4 se ubicaron entre los 9-35 km de distancia del CVPCC (campo cercano); y 3 entre los 35-80 km (campo lejano). Luego de generada la erupción, se instalaron 3 nuevas estaciones de banda ancha 30 segundos adicionales en campo cercano (Reftek151-30A, 0.03-50 *Hz*, digitalizadores Reftek 130B), esto con el objeto de localizar y caracterizar, de forma más precisa, la actividad post-eruptiva. Finalmente, se contó con la instalación de dos cámaras que monitorearon el fenómeno eruptivo (Cámaras: Sony Ipela SNC-RZ25N y Axis P1343), facilitando la vigilancia de la fase post-eruptiva.
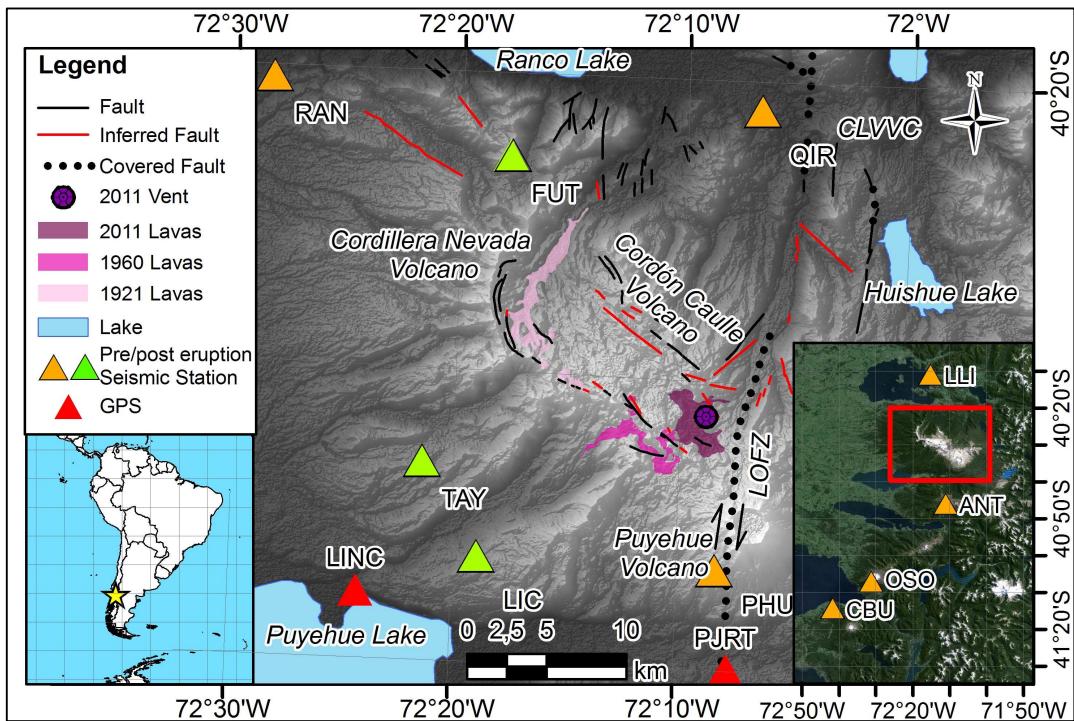
Figure 1.6.1.1 Localización del Compejo Volcánico Puyehue Cordón Caulle (CVPCC) ubicada en la Zona Volcánica Sur (ZVS) de los Andes del sur de Chile. En la parte superior del mapa se pueden ver las principales estructuras geológicas (LOFS sistema de falla Liquiñe-Ofqui), los flujos de lava generados por las erupciones de 1921, 1960 y 2010, el cono de 2011 y la ubicación de las estaciones sísmicas. La imagen de la esquina inferior derecha muestra la ubicación de las estaciones sísmicas de campo lejano. Fuente: elaboración propia.

1.6.2 Metodologías y análisis de los datos geofísicos

El detalle de las metodologías más importantes desarrolladas en esta tesis (modelo de velocidad 1D, Parámetro b e inversión de ondas sísmicas) fueron descritas con más detalle en el capítulo de Material Suplementario.

1.6.2.1 Clasificación de sismos

Las señales sísmicas trabajadas en esta tesis doctoral fueron analizadas utilizando diferentes algoritmos, esto con el fin de obtener una caracterización de la actividad sísmica y así poder sugerir las posibles fuentes sísmicas que actuaron durante el ciclo pre y post-eruptivo. Para llevar a cabo este trabajo, se clasificaron cerca de 32.850 sismos registrados entre diciembre de 2010 y diciembre de 2011 (7100 Volcano-Tectónicos, 12.500 de tipo

Largo Período/Muy Largo Período; 7.150 Híbridos; 6.100 Tremores), utilizando para ello la clasificación propuesta por Lahr et al. (1994) y Chouet (2003), las que se basan principalmente en características espectrales, morfologías de ondas y la duración que poseen los diferentes sismos. De esta forma, el catálogo se subdividió en: 1.- sismos asociados con fracturamiento de material cortical (Volcano-Tectónico [VT]); 2.- eventos generados por perturbación o migración de fluidos magmáticos/hidrotermales (Largo Período [LP] y Muy Largo Período [VLP]); 3.- sismos compuestos que involucran una combinación de los orígenes (Híbrido, [HB]) y finalmente 4.- el Tremor volcánico [Tr], fenómeno caracterizado por presentar una combinación de fuentes sísmicas que se extienden por largos períodos de tiempo (minutos-horas-días, Aki 1981 y Chouet 1981). Un caso particular de tremor fue clasificado como cuasi-arónico, señal que se caracterizó por presentar un espectro de frecuencias muy particular, con un pick dominante de 1.0 Hz y luego tres picos subdominantes en 2.0, 2.9 y 3.8 Hz, mostrando un patrón modulado la mayor parte del tiempo.

1.6.2.2 Relocalización y modelo de velocidad

Uno de los rasgos más importantes en una erupción es la distribución tanto espacial como temporal de la actividad sísmica. Con el objeto de mejorar las localizaciones obtenidas con HYPO71, y así poder identificar claramente las reactivaciones de estructuras mayores involucradas en la crisis volcánica, se calculó un modelo de velocidad local en 1 dimensión (1D) para el CVPCC. Para el desarrollo del modelo 1D, se utilizó el programa VELEST (*Joint Hypocenter Determination technique* JHD; Kissling et al., 1994), relocalizando parte de la actividad sísmica. Es importante destacar que para lograr una buena solución del modelo de velocidades, se debe trabajar con sismos que tengan buenas localizaciones. Para llevar a cabo esta labor, se filtró la base de datos, se tomaron sismos que tuvieran 8 o más fases leídas, errores horizontal < 0,5 y vertical < 1 km, gap<180°, y soluciones con RMS < 0,15; obteniendo como resultado final 425 sismos (entre VT y HB) registrados entre abril y diciembre de 2011. Se utilizó un nivel de referencia de 1,5 km s.n.m, altura promedio que posee el graben del CVPCC.

1.6.2.3 Polarización y cuantificación de ondas sísmicas

Con el objetivo de corroborar la existencia de ondas *p* en las trazas sísmicas para eventos representativos (>10 μm) de baja frecuencia (LP, VLP y Tr cuasi-armónico), se utilizó la polarización de ondas (Matsumura 1982). Con este método adicionalmente se logró estimar

algunas localizaciones, ya que se pudieron calcular azimuts [A$_Z$] y ángulos de incidencia [Φ] de las ondas P para cada una de las estaciones receptoras que conforman la red sísmica. Esta herramienta fue de gran ayuda, ya que debido al carácter emergente de muchos sismos, se lograron sugerir localizaciones aproximadas tanto para sismos de tipo LP como el Tr cuasi-armónico, logrando identificar su fuente, y con ello, sugerir su origen (emisión de lavas). La cuantificación de la magnitud para los sismos de tipo VT y HB se llevó a cabo utilizando la magnitud local [*Ml*] propuesta por Lee et al., 1972. De igual forma, para poder cuantificar el tamaño del tremor volcánico y sismos tipo LP-VLP y Tr, se utilizó el desplazamiento reducido (D$_R$, Aki 1981), herramienta que fue útil al momento de pronosticar la erupción, ya que fue posible cuantificar el incremento de la actividad sísmica asociada con el tránsito/ascenso de fluidos, logrando tomar acertadas decisiones al momento de sugerir los cambios de alerta a las autoridades durante la crisis volcánica.

A= mayor amplitud de la señal sísmica (cm/s)
r=distancia estación-fuente sísmica (cm)
P=período predominante de la señal sísmica (s)

$$D_R \, (\text{cm}^2) = \frac{A \, r \, P}{4\sqrt{2\pi}}$$

1.6.2.4 Mecanismos focales e inversión de ondas sísmicas

Para poder determinar los principales ejes de esfuerzos involucrados en la actividad volcánica, y con ello poder reconstruir las fuentes sísmicas implicadas en el proceso, se trabajaron mecanismos focales [MF] con eventos que presentaran una *Ml*>3,0. Se utilizó el programa SEISAN (Earthquake Analysis Software Versión 10.0), generando finalmente 26 MF con 7 o más polaridades impulsivas. Con el propósito de lograr restringir de mejor forma las soluciones (elección de planos nodales), se complementaron los resultados con la relación de amplitudes de las ondas S/P (Hardebeck y Shearer 2003). De igual forma, y considerando además la participación de fluidos magmáticos y/o hidrotermales asociados a mecanismos No-doble-Cupla [NDC] en su fuente, se calculó el tensor de momento [TM] sísmico, utilizando inversiones de ondas sísmicas. Las inversiones calculadas se realizaron tanto para eventos de tipo VLP-HB como para sismos tipo VT. Las inversiones se llevaron a cabo utilizando ondas de cuerpo, las cuales fueron identificadas mediante el método de polarización de ondas, utilizando para ello un filtro pasa bajos <0,25 Hz. El objetivo de utilizar metodologías diferentes para el cálculo de mecanismos focales se debe a que estas son complementarias y por otro lado se busca validar los resultados obtenidos mediante las inversiones. El software utilizado para las inversiones fue ISOLA versión 2013 (Sokos y Zahradnik 2008). Este programa está basado en iteraciones de deconvolución punto-fuente para ondas de cuerpo. El cálculo de las funciones de Green asociado al campo de onda total

generado producto del comportamiento elástico de la corteza, se realizó siguiendo la metodología propuesta por Bouchon (1981). El tensor de momento es calculado con el método de mínimos cuadrados. El tiempo de origen y la posición espacial de la fuente puntual (centroide) se buscaron entorno al hipocentro relocalizado por VELEST. Luego de ingresar la respuesta instrumental de las estaciones y definir un modelo cortical de velocidad de propagación para las ondas de cuerpo (P y S), se procedió a integrar el registro sísmico, ya que el programa ISOLA trabaja con sensores que miden desplazamientos y no con sensores que miden velocidades. De igual forma, y para corroborar que la relación señal/ruido estuviera por sobre los parámetros necesarios para invertir las señales, se graficaron en el dominio de la frecuencia y del tiempo, evitando que el registro se distorsiona producto del bajo coeficiente señal/ruido. Finalmente, para el cálculo de las inversiones se utilizó la aproximación a la solución: "único punto de origen", iterando cada 1 km desde 0,25 a 12,25 km de profundidad.

1.6.2.5 Parámetro b

Debido a la gran cantidad de sismos relacionados con el proceso volcánico, su distribución temporal y la variada gama de magnitudes, se analizó la "Distribución de la Frecuencia de Magnitudes" (DFM) a través del tiempo, abarcando desde abril de 2011 (fase pre-eruptiva), hasta la emisión de lavas silícea, involucrando una amplia gama de magnitudes en el proceso. Con el objetivo de cuantificar y determinar las anomalías sísmicas atribuidas a la erupción, se procedió a establecer la variación temporal del parámetro b (*b-value*). El valor de b se calculó utilizando un script realizado por el geofísico de la Universidad de Concepción Sr. Hugo Soto durante el trabajo que realizó en el grupo de investigación del profesor guía de esta tesis Dr. A. Tassara. Se trabajó con un total de 1.750 sismos localizados, con una magnitud de completitud (*MC*) de 1,6. Para el cálculo de b, se utilizaron ventanas de 125 sismos y un *overlap* de un 75%. Con el objeto de poder validar los datos utilizados en el proceso, se calculó además el error de b (estimación de la incertidumbre) propuesto por Aki (1965).

1.7 Contenido de la tesis

Esta tesis consta de tres publicaciones, las dos primeras fueron trabajadas como co-autor, en las que se desarrolló un análisis sismológico específico centrado en dar respuesta a un fenómeno particular del ciclo eruptivo que se desarrolló en el CVPCC durante el año 2011. El primer artículo hace referencia al análisis del tremor cuasi-armónico, el que se relacionó con las tasas de emisiones de lava riolítica en superficie a través del desplazamiento reducido

(D_R), valor inmerso en la señal sísmica del tremor. El segundo artículo intenta modelar la deformación que sufrió el CVPCC antes y después de la erupción, utilizando datos InSAR y de GPS, y como esta deformación se relaciona con la actividad sísmica, sus localizaciones tanto espaciales como temporales, sus fuentes sismogénicas y las estructuras que participaron del fenómeno eruptivo. De igual forma, con la relocalización se logró calcular un nuevo modelo de velocidades para el complejo, sugiriendo cambios reológicos importantes, los cuales facilitarían el alojamiento de magmas en zonas más someras, resultados consistentes con las observaciones realizadas con los datos geodésicos. Finalmente, el tercer artículo (autor) está centrado en entender los procesos y mecanismos que se generan en las erupciones más explosivas del fenómeno volcánico, fenómenos pobremente estudiados a nivel mundial. En este trabajo se describió detalladamente toda la actividad sísmica antes, durante y después de la erupción, individualizando sus principales fases, estableciendo las fuentes sismogénicas, la evolución espacio-temporal de la sismicidad, los mecanismos focales asociados, la evolución del parámetro b durante la crisis volcánica y se sugieren los posibles mecanismos que controlaron la erupción. En la última parte, se intenta abordar la relación entre terremotos y actividad volcánica, ya que existe evidencia que sugieren la participación del terremoto del Maule (Mw:8.8) como un fenómeno que aceleró el proceso eruptivo ya en gestación dos años antes (2008-2009) para el CVPCC.
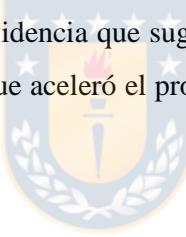
CAPÍTULO II: High effusion rates of the Cordón Caulle 2011–2012 eruption (Southern Andes) and their relation with the quasi-harmonic tremor

Paper published in Geophysical Research Letters

D. Bertin[1], L. E. Lara[1], D. Basualto[1,2], Á. Amigo[1], C. Cardona[1,2], L. Franco[1,2,] F. Gil[1], and J. Lazo[1]

[1]Red Nacional de Vigilancia Volcánica, Servicio Nacional de Geología y Minería, Temuco, Chile.

[2]Departamento Ciencias de la Tierra, Facultad de Ciencias Químicas, Universidad de Concepción, Concepción, Chile.

2.1 Resumen

Las altas tasas de efusión de lavas silíceas parecen ser menos infrecuentes de lo que se pensaba, en particular durante sus etapas eruptivas iniciales. En este estudio, reportamos velocidades de descarga promediadas calculadas por satélite para la fase efusiva 2011-2012 en el Cordón Caulle, las que muestran una buena correlación con la evolución del temblor cuasi-armónico, la señal sísmica más significativa después de la etapa explosiva inicial. Tal correspondencia podría convertirse en un método clave para la detección del inicio de las fases efusivas, especialmente en áreas remotas y/o muy nubladas, proporcionando una herramienta adicional de advertencia efectiva y para la evaluación de peligros y sus riesgos en tiempo casi real.

Es importante destacar que el trabajo realizado en esta publicación consistió en identificar y clasificar el tremor cuasi-armónico que se registró en toda la red de estaciones durante la fase post-eruptiva (Fig. 3.2 b y c), para luego realizar un script en MatLAB que tomara los parámetros de: distancia, amplitud y frecuencia de la señal sísmica con los cuales se calculó el Despazamiento Reducido de la señal de tipo tremor (reduced displacement, cuantificado en cm^2, Fig. 2.3 a), herramienta que luego fue utilizada para establecer

cuantitativamente tasas de emisión de lavas riolíticas (m³/s). Debido a que esta señal de tremor podía tener variadas fuentes, adicionalmente se definió el tipo de onda de cuerpo (onda p, Fig. 2.3 d) y adicionalmente se calculó el azimut (ángulo) de arribo de dicha onda para cada una de las estaciones que componían la red, esto con el objetivo de identificar el origen de esta señal, la que fue consistente con la emisión de lavas localizadas desde el vent alojado en superficie.

2.2 Abstract

High effusion rates of intermediate-to-high-silica lavas seem to be less uncommon than previously thought, in particular during their initial eruptive stages. In this study, we report satellite-based time-averaged discharge rates for the 2011–2012 effusive phase at Cordón Caulle, which are well correlated with the evolution of the quasi-harmonic tremor, the most significant seismic signal after the initial explosive stage. Such a correspondence could become a key method for detection of the onset of effusive phases, especially in remote and/or very cloudy areas, supplying an additional tool for effective warnings and near-real-time hazard appraisal.

2.3 Introduction

Since Walker [1973] coined the term "effusion rate," further improved by Lipman and Banks [1987], diverse methods have been proposed in order to obtain more rigorous estimations of the rates at which the lava is emitted. In fact, during the past decade they were grouped, for example, in model-based measurements, volume-based measurements, sulphur flux based measurements, deformation data, and seismic and thermal approaches [Harris et al., 2007, and references therein], where volume-based implies changes in volume over a known time interval.

Intrinsically linked to the growth of a lava body [Wadge, 1978; Pieri and Baloga, 1986; Swanson and Holcomb, 1990; Stasiuk and Jaupart, 1997], measurement of effusion rates allows to constrain mass flux out of the shallow feeder system and to assess/model the dynamics of the effusive behavior [Wadge, 1981; Denlinger, 1997; Harris et al., 2000]. Accordingly, effusion rate is a crucial parameter for understanding of the eruptive style and lava flow dynamics during ongoing eruptions and/or assessing the most likely hazards posed by an active flow [Kilburn et al., 1995; Tanguy et al., 1996; Sparks et al., 1998; Calvari et al., 2003; Harris et al., 2007]. Other useful terms are Eruption rate and Mean output rate [Harris

et al., 2007]; the former strictly related to the total volume of lava emitted since the onset of the effusive phase and divided by the elapsed time, while the latter is the final volume of lava divided by the total duration of the eruption.

The effusive behavior of many of the most active volcanoes worldwide has allowed accurate estimates of effusion rates. In fact, many studies have been carried on Etna [Wadge, 1978; Guest et al., 1987; Harris et al., 2000; Harris and Neri, 2002; Behncke and Neri, 2003; Calvari et al., 2003; Andronico et al., 2005; Burton et al., 2005; Mazzarini et al., 2005], Kīlauea [Richter et al., 1970; Jackson et al., 1975; Swanson et al., 1979; Tilling, 1987; Rowland and Munro, 1993; Harris et al., 1998], Krafla [Harris et al., 2000], Piton de la Fournaise [Battaglia et al., 2005], Okmok [Patrick et al., 2003], Fernandina [Rowland, 1996], and Stromboli [Harris et al., 2000; Calvari et al., 2005]. Many of these studies are focused in basaltic and basaltic andesite volcanoes, but the abundance decreases dramatically for more SiO2-rich magmas. Consequently, a few studies can be found for more evolved magmas as those erupted from Soufrière Hills [Sparks et al., 1998], Santiaguito [Rose, 1973; Harris et al., 2002, 2003], St. Helens [Anderson and Fink, 1990; Fink et al., 1990], Unzen [Nakada et al., 1999], Chaitén [Pallister et al., 2013a], Merapi [Pallister et al., 2013b], Augustine [Coombs et al., 2010], and Redoubt [Diefenbach et al., 2012]. Effusion rates as high as ~130m^3/s and ~400m^3/s have been measured for Etna 1981 [Guest et al., 1987] and Kīlauea 1959–1960 [Richter et al., 1970] eruptions, respectively, although for those basaltic centers their mean output rates have been estimated as ~15m^3/s for the former [Harris et al., 2000] and ~3m^3/s for the latter [Swanson et al., 1979; Tilling, 1987; Rowland and Munro, 1993]. Conversely, good statistics are scarce for silicic centers, and the most reliable values are ~65m^3/s for flow [Kilburn et al., 1995; Tanguy et al., 1996; Sparks et al., 1998; Calvari et al., 2003; Harris et al., 2007]. Other useful terms are Eruption rate and Mean output rate [Harris et al., 2007]; the former strictly related to the total volume of lava emitted since the onset of the effusive phase and divided by the elapsed time, while the latter is the final volume of lava divided by the total duration of the eruption. Chaitén 2008 [Pallister et al., 2013a] and less than 40m^3/s for Augustine 2006 [Coombs et al., 2010], Redoubt 2009 [Diefenbach et al., 2012], and Merapi 2010 [Pallister et al., 2013b] eruptions. Those high values seem to be more common than previously recognized, particularly during the initial phases [Pallister et al., 2013b].Which is remarkable is that most of these values have been obtained in the last 5 years, suggesting that they are linked to advances in some measuring techniques (e.g., volume and sulphur flux-based measurements, deformation data, and seismic and thermal approaches [Harris et al.,

2007]). Consequently, the rhyolitic composition of the lava flow field emitted during the Cordón Caulle 2011–2012 eruption [Castro et al., 2013], together with a reliable sequence of satellite images and seismological data, indeed represents a key opportunity to estimate effusion rates and recognize signals of the explosive-effusive transition, a key issue for silicic eruptions [e.g., Eichelberger et al., 1986; Woods and Koyaguchi, 1994; Adams et al., 2006; Degruyter et al., 2012; Schipper et al., 2013; Castro et al., 2014].

Concurrently, volcanic tremor has been described in many eruptions worldwide [e.g., Yamaoka et al., 1991; Kawakatsu et al., 1992; McNutt,1992; Falsaperla et al., 1998; Cannata et al., 2010; Tárraga et al., 2014] although different mechanisms have been proposed for its source. The classical model developed by Aki et al.,[1977] describes tremor as generated by the vibration of cracks filled with magma and driven by the excess of magmatic pressure, triggering a sudden jerky extension of the cracks if the tensile strength varies spatially. Conversely, Chouet [1981], Fehler and Chouet [1982], and Chouet [1988] proposed a hydraulic transient pressure origin (either magmatic or hydrothermal) within a crack or conduit. Another possibility that should be considered is related to a complete masking of the tremor source by conduit resonance, as was noted by Denlinger and Moran [2014] during a noneruptive tremor episode at Mount St. Helens in 2004, which was finally linked to cataclastic deformation along the conduit wall. Accordingly, it was first established that the nature of the tremor effectively pointed out to a shallow source and, subsequently, an effusive behavior was directly observed.

An example of the use of volcanic tremor to estimate effusion rates can be found in Battaglia et al. [2005], who observed a quadratic relation between both lava flow rate and tremor source amplitude during eruptions of the basaltic Piton de la Fournaise volcano. In fact, their best estimations were done using such a quadratic relation for frequencies below 5 Hz, obtaining volumes 15% and 30% lower than those field measured for the July–September 1999 and February 2000 eruptions, respectively. However, that method does not explain the large amounts of magma erupted at the beginning of both eruptions, probably due to local processes (e.g., geometry changes of the conduit), and hence, tremor amplitude would be useful to estimate effusion rates through longer time scales.

As counterexamples, propagation of opening fissures during eruptions reported by Aki et al. [1977] and Aki and Koyanagi [1981] was not accompanied by any seismicity, showing

that in some cases (generally basaltic lava fountaining) the correlation of lava flow rate and the tremor signal is poor. Additional problems arise because of many moderate-to-highly uncertain variables, such as channel shape, jerky crack extension, conduit width, transient pressure fluctuations, and gas-bubble fraction. To avoid those uncertainties, we propose here an approach using the steady cumulative reduced displacement [after Aki and Koyanagi, 1981] from the quasi-harmonic tremor in a 1 h time window.

Finally, there is strong evidence that tremor amplitude depends on fluid viscosity and the source area [Chouet, 1988], suggesting that a relationship between reduced displacement and lava flow rate, as proposed here, could be more successful if meets some conditions, such as shallow source and viscous magma. Those requirements were satisfied during the 2011–2012 Cordón Caulle eruption [Castro et al., 2013], so a reliable correspondence between both parameters can be found in order to recognize variations in the lava flow rate and to firmly establish the beginning of the effusive phase.

2.4 Time-Averaged Discharge Rates Estimated From Satellite Data

Here we used panchromatic and radar satellite imagery to delineate the lava emplacement between June 2011 and August 2012 into a tectonic depression of known volume and without signatures of surface rupture or volume change. Previous studies have been carried out at Augustine, Etna, Mauna Iki, and Okmok volcanoes, but preferably using panchromatic or thermal data to obtain the lava morphology, so the volume was calculated either knowing areas and heights or by means of a local digital elevation model [e.g., Rowland and Munro, 1993; Harris and Neri, 2002; Patrick et al., 2003; Coombs et al., 2010]. Here we considered that the lava volume is given by the fill volume into the depression, calculated using a preeruptive Advanced Spaceborne Thermal Emission and Reflection Radiometer (ASTER) Global Digital Elevation Model version 2 [Advanced Spaceborne Thermal Emission and Reflection Radiometer Global Digital Elevation Model Validation Team, 2011] with a spatial resolution of ~30m for the study area.

Satellite imagery consisted of 20 Strip Map TerraSAR-X (from12 June 2011 to 11 August 2011), seven panchromatic Advanced Land Imager Earth Observing-1 (from 31 July 2011 to 26 January 2012), and two panchromatic multispectral WorldView-2 images (for 10 April 2012 and 27 August 2012). All these images covered 14 months since the beginning of the effusive phase and had a frequency of ~3 days for the first 60 days and ~2months for the

next year. All images were processed in ArcMap 10[®] in order to obtain shape files, which allow area-covered estimations (Figure 2.1). Fill volumes were calculated with Global Mapper 13[®] coupling each shape-file with the ASTER Global Digital Elevation Model version 2, assuming a constant edge thickness of 35 ± 2.5m for the lava as measured in the field [e.g., Tuffen et al., 2013]. In addition, it was assumed that the top of each fill volume consisted in a flat surface, which height was defined by the edge thickness and confirmed as a good approach by field inspection.

Effusion rates were measured as the difference among two consecutive volumes divided by the elapsed time (units in m^3/s; Figure 2.3a). According to Harris et al. [2007], this procedure corresponds to "time-averaged discharge rates", whose benefits include smoothing of any short-term variation that could be nonrepresentative for the long-time effusive activity [Bailey et al., 2006]. Uncertainties were managed considering limit values of the estimated volumes, which include the 2.5m error on the thickness at the edge.
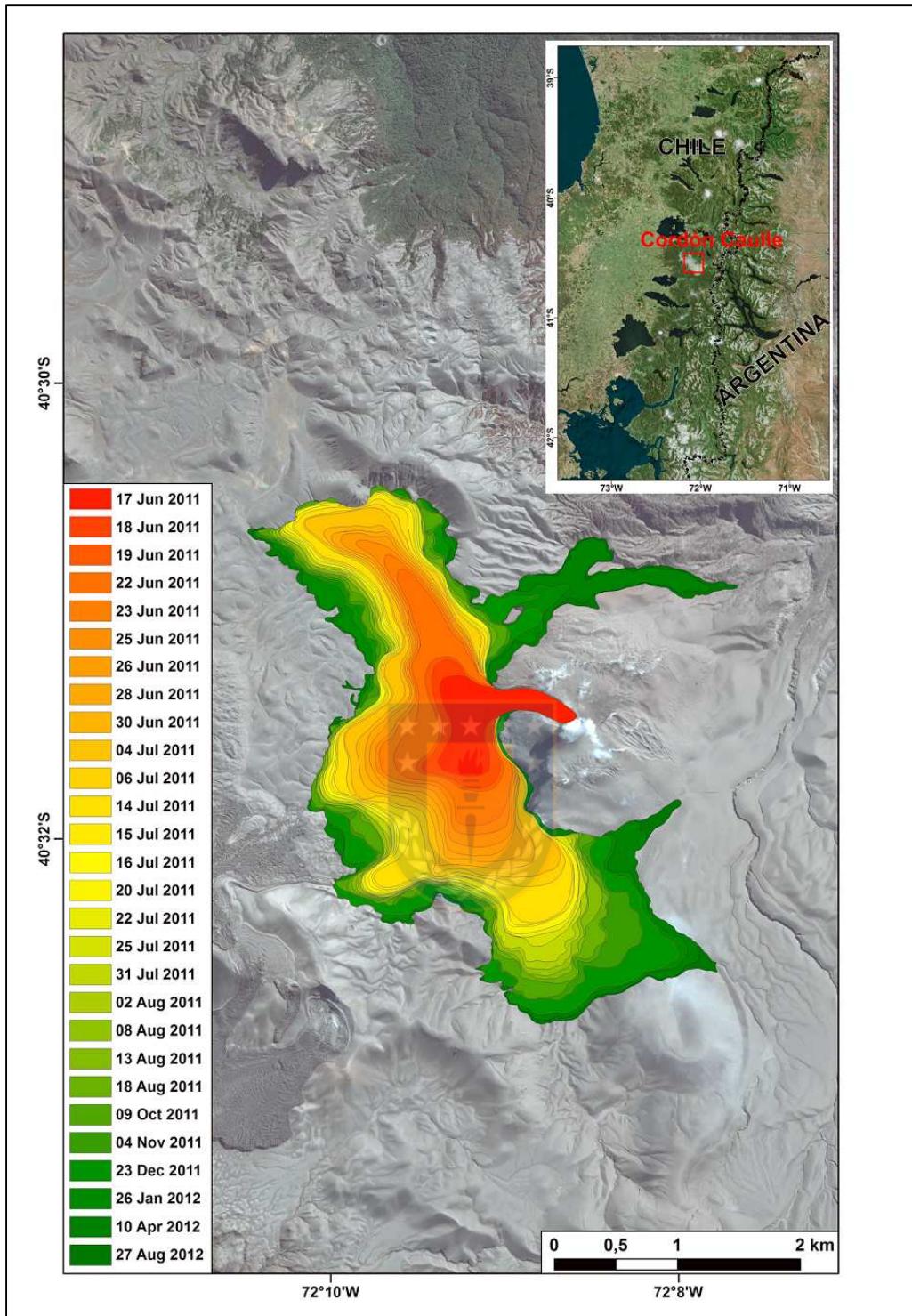
Figure 2.1 Map showing lava flow extent throughout 14 months. The flow filled initially a NW-SE tectonic depression. Then, by October 2011, the lava overstepped that and started to flow northeastwards through a narrow channel. A map of regional location is shown in the inset. Fuente: Bertín et al. (2015).
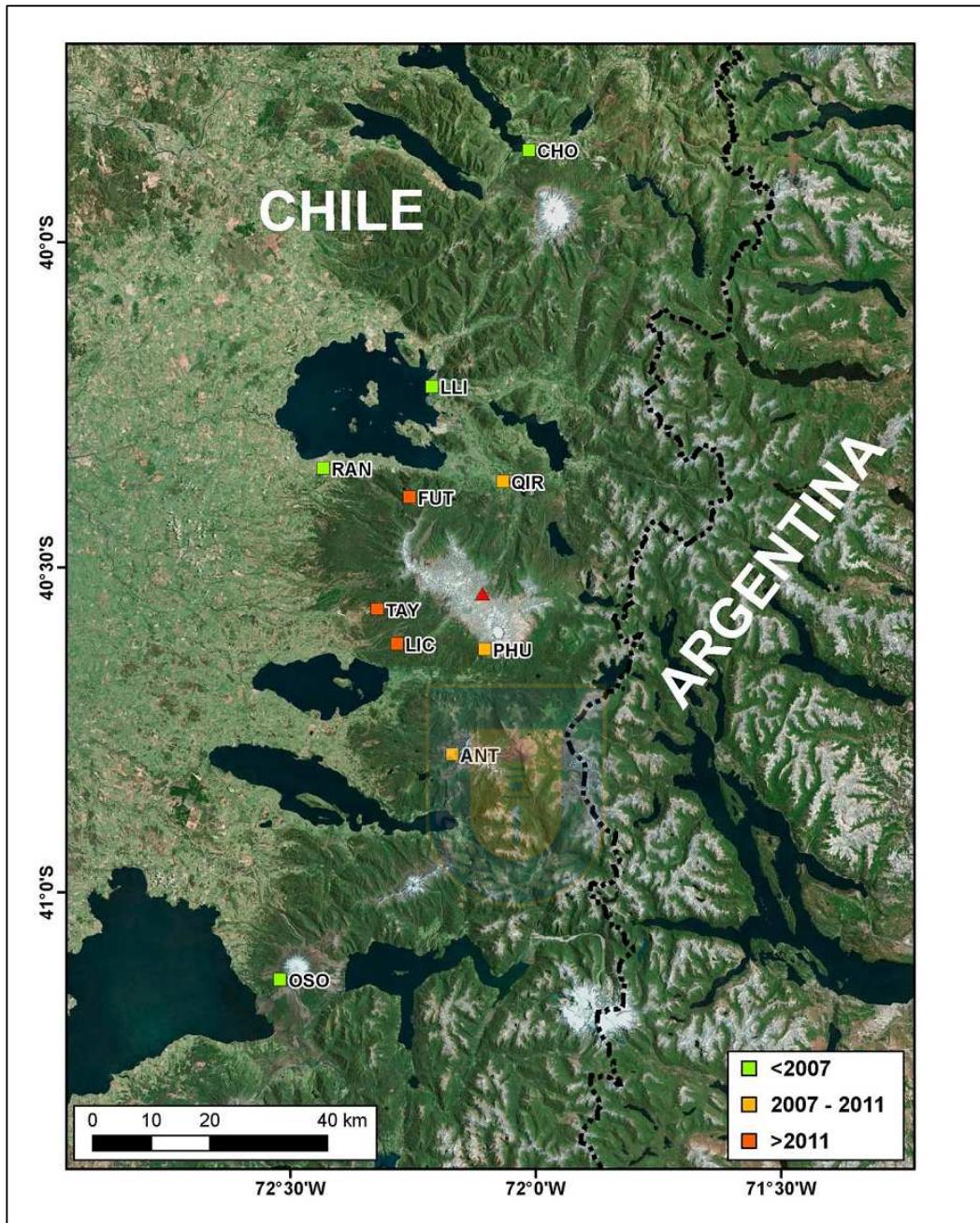
Figure 2.2 Seismic network before and during the Cordón Caulle 2011–2012 eruption. The 2011 vent is highlighted as a red triangle. The stations were grouped considering their start-up. PHU depicts the closer station to the vent (~8 km), in which all the analysis were performed and consists in a broadband (30 s) Güralp CMG-6TD seismometer. Fuente: Fuente: Bertín et al. (2015).

2.5 Observation of Tremor

Puyehue-Cordón Caulle Volcanic Complex and Carrán-Los Venados distributed field [Lara et al., 2006] began to show some variable patterns of shallow seismicity since 2007. By that time, seismological network installed around the complex by the volcano observatory (OVDAS, the Southern Andes Volcanic Observatory at SERNAGEOMIN) was composed by four broadband (30 s) stations (two near-field and two far-field). Between 2007 and early 2011 three near-field broadband stations were added. On February 2011, clear unrest was detected with an epicentral area on the northern part of Cordón Caulle, consisting of volcanotectonic (VT), long-period, and hybrid events, evolving to a more intense and shallow seismicity on April 2011. Since 3 June 2011, seismic activity increased vigorously both in number of events and magnitude, together with migration of the epicenters to the area where the active vent appeared. Such an increase of seismicity lasted until the beginning of the explosive eruption on 4 June 2011 (18:45 UTC), being accompanied by surface deformation up to 10 km away from the vent [Jay et al., 2014]. Three more near-field broadband stations were quickly installed, completing eight near-field and two far-field seismic stations (Figure 2.2).
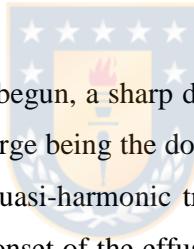
Once the explosive phase had begun, a sharp decrease of VT seismicity was recorded and a spasmodic tremor started to emerge being the dominant component of the signal since 6 June. On 15 June at 19:00 UTC, a quasi-harmonic tremor was recorded (Figures 2.3b and 2.3c), which was associated with the onset of the effusive phase [Cardona et al., 2012]. Lava flow was actually confirmed on 17 June by a Strip Map TerraSAR-X image and later on 20 June by an overflight once the eruptive column declined.

2.6 Results

During the effusive phase, quasi-harmonic tremor showed a maximum reduced displacement equal to 195 cm^2 (Figure 2.3a) with a dominant frequency of 1.0 Hz and three subdominant peaks in 2.0, 2.9, and 3.8 Hz, showing a modulated pattern most of the time (Figures 2.3b and 2.3c). Since quasi-harmonic frequencies were common at all the stations, it was inferred that they were associated with a common source. Along the entire effusive phase, tremor particle motions showed a P wave nature with incidence angles close to 90° (Figure 2.3d), pointing out to a shallow source and being consistent with the observed effusive behavior. Furthermore, there were virtually no changes with respect to the dominant frequency. Accordingly, among the many models proposed for volcanic tremor worldwide [Alparone et al., 2003, and references therein], the data presented here suggest that this quasi-

harmonic tremor was caused by oscillations of volcanic layers from moving magma [Omer, 1950].

On the other hand, the highest time-averaged discharge rate reached $72.1 \pm 5.6\mathrm{m^3/s}$ and was obtained 8 days after the onset of the effusive phase. During the first 20 days, eruption rate averaged $50\mathrm{m^3/s}$ and mean output rate, obtained once the eruption had finished by mid-2012 [Tuffen et al., 2013], was $16.7 \pm 0.5\mathrm{m^3/s}$. Such a high discharge rate can be appreciated more properly considering other effusive eruptions worldwide plotted against their silica content (Figure 2.4).
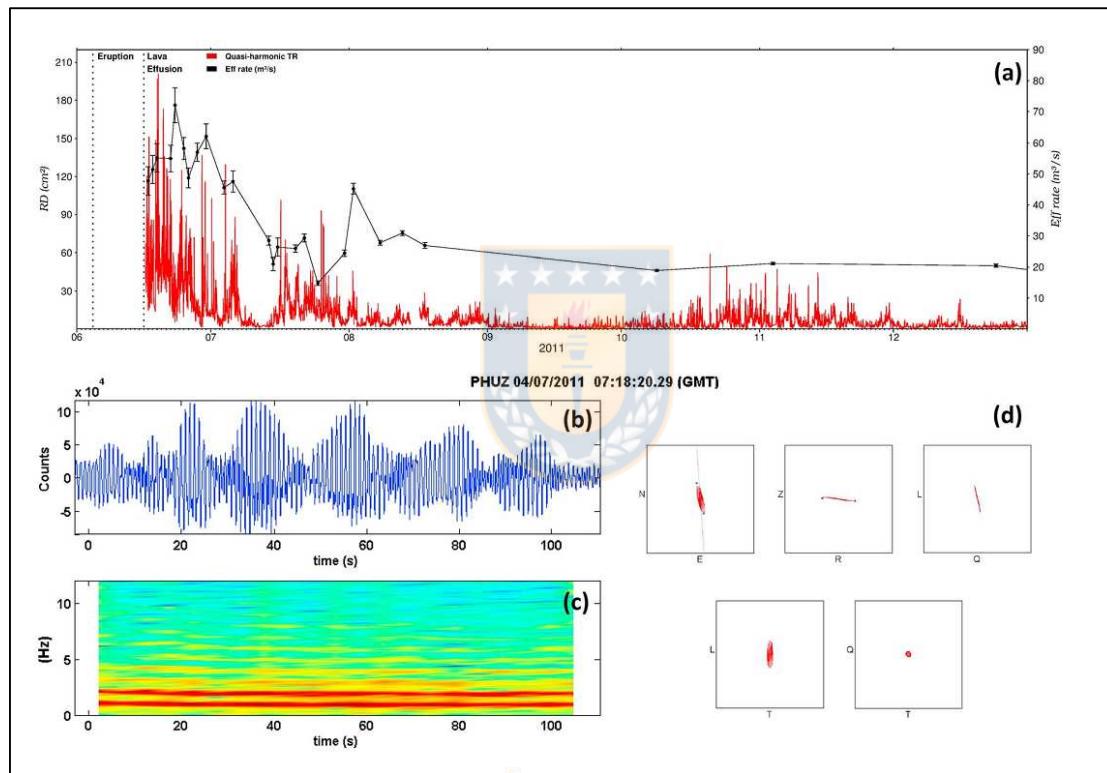
Figure 2.3 (a) The maximum reduced displacement in $\mathrm{cm^2}$ calculated in a 1 h time window (red line) and the time-averaged discharge rate in $\mathrm{m^3/s}$ (black dotted line). (b) The velocity seismogram of tremor with its related spectrogram (c) highlighting the quasi-harmonic pattern. (d) A polarization analysis of the tremor within the dominant frequency. PHU denotes the closer station to the vent (~8 km), as can be seen in Figure 2.2. Fuente: Elarboración propia.

2.7 Discussion

A lava body filling a depression (Figure 2.1) gave an excellent chance to obtain volumes without any other rough estimation. The latter, together with good satellite imagery,

allowed us to obtain a time series of discharge rates sufficiently robust to compare with the time series of reduced displacement.

Figure 2.3a shows good correlations on large-to-middle scale, mostly during the first 2 months when both parameters decreased to values after that were maintained by another 2 months. A small reactivation occurred between mid-October and mid-November 2011, with short-lived eruptive columns of ~3300m above sea level. That behavior was accompanied by an increase of the reduced displacement and is temporarily linked to subtle higher discharge rates. On smaller scales, however, there are fairly significant discrepancies, especially during the first 45 days, strongly suggesting that reduced displacements are not exclusively reflecting discharge rates. Indeed, there are some processes where harmonic or quasi-harmonic tremor is identified without lava flow emission. For example, Lascar volcano showed in April 1994 a harmonic tremor characterized by narrow and repetitive peaks at a same frequency, which were explained as movements of shallow water and/or gases [Hellweg, 2000]. Those peaks can also be generated by nonlinear flow-induced oscillations inside the channels transporting magmatic fluids, though seems to be more likely to occur in low-silica rather than intermediate-to-high silica eruptions [Julian, 1994]. Additionally, Galeras volcano showed in 1991 short episodes of harmonic tremor with a spectrum marked by narrow peaks separated by a constant frequency interval, which suggest resonant excitation of a narrow conduit filled with gases and producing steady degassing on surface [Gil and Chouet, 1997]. Furthermore, some discrepancies can also be rooted within the different temporal lapses inherent to both parameters. In fact, reduced displacement was obtained every hour while time-averaged discharge rate, in the first 2 months, was obtained using satellite imagery spaced by ~3 days, implying that each estimate of discharge rate covers ~72 counts of reduced displacement, and hence, the bigger the time lapse considered for the time-averaged discharge rate, the bigger the discrepancies. Another issue that should be considered is the standard deviation (1σ) of the discharge rate, which is bigger at shorter time lapses.
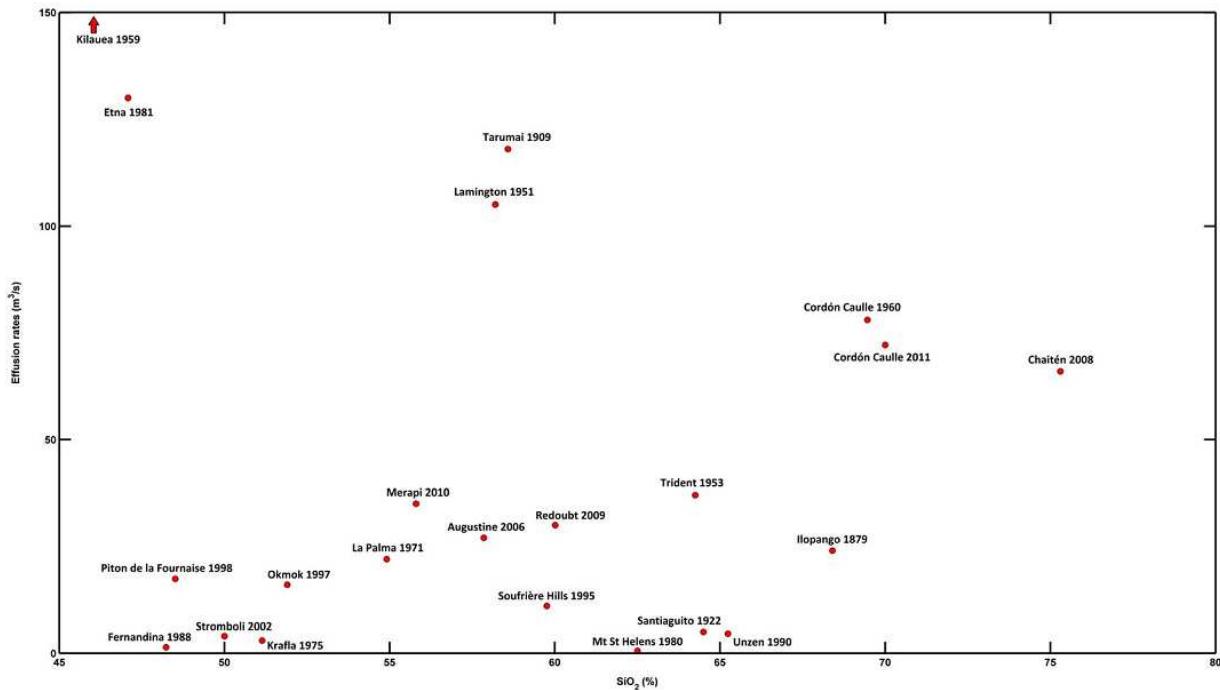
Figure 2.4 Effusion rates for 22 volcanic eruptions plotted against their silica content. Cordón Caulle and Chaitén effusion rates belong to both higher effusion rates and silica content. Extremely high effusion rate measured for Kīlauea 1959–1960 eruption ($\sim$400m^3/s) is plotted outside the figure. Some effusion rates are based on Pallister et al. [2013a]. Eruptions plotted are Kīlauea 1959 [Richter and Eaton,1960; Macdonald and Katsura, 1961], Etna 1981 [Guest et al., 1987], Piton de la Fournaise 1998 [Villeneuve, 2000; Vigouroux et al., 2009], Fernandina 1988 [Rowland, 1996; Allan and Simkin, 2000], Stromboli 2002 [Calvari et al., 2005; Landi et al., 2006], Krafla1975[Jónasson, 1994; Harris et al., 2000], Okmok 1997 [Patrick et al., 2003; Larsen et al., 2013], La Palma 1971 [Prægel and Holm, 2006],Merapi 2010 [Surono et al., 2012; Pallister et al., 2013b], Augustine 2006 [Coombs et al., 2010; Larsen et al., 2010], Lamington 1951 [Arculus et al., 1983], Tarumai 1909 [Ishikawa, 1952], Soufrière Hills 1995 [Devine et al., 1998; Sparks et al., 1998], Redoubt 2009 [Coombs et al., 2013], St Helens 1980 [Swanson et al., 1987; Fink et al., 1990], Trident 1953 [Coombs et al., 2000], Santiaguito 1922 [Harris et al., 2002], Unzen 1990 [Nakada and Motomura,1999; Nakada et al., 1999], Ilopango 1879 [Richer et al., 2004], Cordón Caulle 1960 [Lara et al., 2004], Cordón Caulle 2011 [Castro et al., 2013], and Chaitén 2008 [Pallister et al., 2013a]. Fuente: Bertín et al. (2015).

At the end of 2011, despite the reduced displacement was near the background noise, the end of the eruption could not be established yet because of the time-average discharge rates still reaching 20m^3/s (Figure 2.3a). In fact, the lava was still pouring out of the vent during January 2012 [Schipper et al., 2013; Tuffen et al., 2013] and the lava supply actually ceased by mid-2012 [Tuffen et al., 2013]. By August 2012, satellite imagery still showed

increases in the lava flow area (Figure 2.1) but such changes were probably not produced by eruptive activity but by gravitational rearrangements of the blocks at the lava front [Tuffen et al., 2013], causing spreading without significant volume increase.

The highest effusion rates obtained here (~70m^3/s) are surprisingly similar to that estimated for the Cordón Caulle rhyodacitic fissure eruption in 1960 [Lara et al., 2004; Pallister et al., 2013a, and references therein]. Furthermore, considering both effusion rates and silica content for 22 eruptions worldwide (Figure 2.4), the values here obtained confirm that high effusion rates are not only restricted to low-to-intermediate silica eruptions [Pallister et al., 2013b]. This is not a coincidence but a result of recent advances in several estimation methods.

2.8 Concluding Remarks

There are many volcanoes worldwide for which, due to geographic and/or extreme weather conditions, it would be impossible to do a reliable estimation of time-averaged discharge rates. Here we propose a suitable approach to estimate them indirectly using data provided by tremor characterization (e.g., amplitude and dominant frequency, and hence reduced displacement), which can be easily measured. Indeed, in the same way as Battaglia et al. [2005] found empirical relations between tremor source amplitude and lava flow rates, we have observed a general relationship between reduced displacements of the quasi-harmonic tremor and time-averaged discharge rates, for what no evident large-to-middle scale discrepancies arise, suggesting that reduced displacement can be used as a proxy of effusion rate throughout the entire eruptive cycle within temporal lapses larger than the average time interval between two consecutive satellite images. A crucial requisite for such a relationship is the absence of other tremor sources, which could produce fairly significant discrepancies.

Time-averaged discharge rates up to 70m^3/s and eruption rates of ~50m^3/s at Cordón Caulle show that high values would be more common for silicic eruptions than previously thought, especially during their early stages, so it would be worth to focus efforts to survey the first 30 or 60 days of a given silicic effusive eruption because of the direct implication on a more accurate hazard assessment, effective warnings, and crisis management. Finally, being most of case studies of effusion rates for fissural-to-punctual basaltic eruptions, here we have expanded to rhyolitic eruptions, settling a precedent toward a unified model of effusive eruptions, especially those accompanied with volcanic tremor.

2.9 Acknowledgments

CAPÍTULO III: Possible structural control on the 2011 eruption of Puyehue-Cordón Caulle Volcanic Complex (southern Chile) determined by InSAR, GPS and seismicity

Geophysical Journal International

Anja Wendt[1,2], Andrés Tassara[3], Juan Carlos Báez[4], Daniel Basualto[5], Luis E. Lara[6], Francisco García[3]

[1]Bayerische Akademie der Wissenschaften, München, Germany

[2]formerly at: Centro de Estudios Científicos, Valdiva, Chile

[3]Departamento de Ciencias de la Tierra, Facultad de Ciencias Químicas, Universidad de Concepción, Chile

[4]Centro Sismológico Nacional, Universidad de Chile, Santiago, Chile

[5]Observatorio Volcanológico de los Andes del Sur, Servicio Nacional de Geología y Minería, Chile

[6]Red Nacional de Vigilancia Volcánica, Servicio Nacional de Geología y Minería, Chile
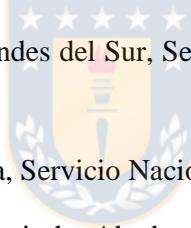
Corresponding author: A. Wendt, Bayerische Akademie der Wissenschaften, Alfons-Goppel-Str.11, 80539 München, Germany, (wendt@keg.badw.de, phone +49- 89230311 111, fax +49- 89230311 100)

Abbreviated title: 2011 eruption of Puyehue-Cordón Caulle Volcanic Complex (southern Chile)

3.1 Resumen

El Complejo Volcánico Puyehue-Cordón Caulle (PCCVC) es uno de los mejores ejemplos de control tectónico y volcánico en la Zona Volcánica Sur de los Andes (sur de Chile). El PCCVC comprende varios centros volcánicos con magmas ricos en SiO_2 alojados en la intersección de la zona de falla Liquiñe-Ofqui (LOFZ) y una estructura del basamento heredado de rumbo NW-SE. El PCCVC comenzó con una erupción explosiva el 4 de junio de 2011, causando una deformación de la superficie a una escala métrica, la que logró ser observada por una serie de satélites ASAR de Envisat. Modelamos estos datos y los

complementamos con series de tiempo de dos estaciones de GPS continuas y además con sismicidad registradas por una red local del Observatorio Volcanológico de los Andes del Sur, OVDAS. La deformación durante los primeros tres días de la erupción pudo ser modelada por dos fuentes puntuales alineadas con el graben NW-SE del Cordón Caulle y por un dique de cierre con un componente significativo de movimiento lateral izquierdo a lo largo del graben. Finalmente, estos modelos se discutieron con respecto a sus implicaciones en la reología propuesta y el mecanismo de la erupción. Las observaciones de GPS cerca del complejo volcánico revelan un efecto adicional más localizado relacionado con la LOFZ al sur del complejo. La deformación co-eruptiva en las principales estructuras geológicas del PCCVC son consistentes con la sismicidad relocalizada, la que se concentra principalmente a lo largo del Graben del Cordón Caulle y en el lado occidental de la LOFZ.

Es importante destacar que el trabajo realizado en esta publicación consistió en relocalizar toda la actividad sísmica (sismos de tipo VT y HB) registrada por la red de estaciones de OVDAS (Fig. 3.1) generada durante y después de la crisis volcánica (abril 2011- abril 2014) para poder entender e interpretar la evolución espacio-temporal de la sismicidad utilizando los sismos de mejor calidad (Fig. 3.7). Para llevar a cabo este trabajo fue necesario realizar un filtro de la actividad sísmica (elegir las mejores localizaciones), para así calcular un nuevo modelo de velocidades (Tabla 3.2) que se ajustara de mejor manera a la realidad reológica del CVPCC, ya que durante la crisis de 2011 se utilizó un modelo de velocidad regional. La relocalización de los sismos, los orígenes involucrados (sismos VT v/s sismos HB) y su disposición tanto espacial como temporal, nos dio la posibilidad de identificar fases asociadas con diferentes fenómenos volcánicos y establecer finalmente las estructuras (fallas) que participaron en la ruptura, migración y posterior erupción, el rol de estas fallas en el tiempo y sugerir un posible reservorio magmático (discontinuidad asociada con un cambio brusco de velocidades), el que fue consistente con los datos de GPS e InSAR.

3.2 Abstract

The Puyehue-Cordón Caulle Volcanic Complex (PCCVC) is one of the best examples of tectonic control on volcanism at the Southern Volcanic Zone of the Andes (southern Chile). The PCCVC comprises several volcanic centres that erupted dominantly SiO_2-rich magmas at the intersection of the trench-parallel Liquiñe-Ofqui Fault Zone (LOFZ) and an inherited NW-SE basement structure. The PCCVC began an explosive and later effusive eruption on 4 June 2011 causing decimetre- to metre-scale surface deformation that was

observed by a series of Envisat ASAR satellite scenes. We modelled this data and complemented it with time series of two continuous GPS stations and seismicity recorded by a local network. Deformation during the first three days of the eruption can be modelled either by two point sources aligned with the NW-SE Cordón Caulle graben or by a closing dike with a significant component of left-lateral motion along the graben. These models are discussed with respect to their implications on the estimated rheology and the eruption mechanism. GPS observations near the volcanic complex reveal an additional, more localised effect related to the LOFZ in the south of the complex. Coeruptive deformation at the main geological structures of the PCCVC is further supported by relocated seismicity, which is concentrated along the Cordón Caulle graben and to the western side of the LOFZ.

3.3 Introduction

Puyehue-Cordón Caulle Volcanic Complex (PCCVC, Fig. 3.1) is a long-lived active centre in the Southern Andes that has erupted basalts to rhyolites since the Middle Pleistocene (Lara et al., 2006; Singer et al., 2008). PCCVC is formed by three juxtaposed volcanoes (Cordillera Nevada caldera, Cordón Caulle fissure system and Puyehue stratovolcano) located to the NW of the intersection between a major trench-parallel fault system (the Liquiñe-Ofqui Fault Zone, LOFZ) with an old NW-SE basement structure (Cembrano & Lara 2009). The volcanoes were active coevally during an early stage but activity focused on Cordón Caulle and Puyehue since the Late Pleistocene. Time-averaged eruptive rates (0.42 km^3/kyr) are one of the highest in the Southern Andes (Singer et al., 2008). The Holocene evolution is characterised by a remarkable emission of silica-rich magmas (~70 % SiO$_2$) sourced at both Cordón Caulle and Puyehue (Lara et al., 2004). After a cone-destruction stage on Puyehue volcano at ca. 1.09 kyr, activity concentrated along Cordón Caulle system with a number of rhyodacitic domes and lava flows. Historical eruptions of 1921 and 1960 were sourced along the Cordón Caulle fissures with multiple vents (Lara et al., 2006). The 1960 event is thought to be a classic example of remote triggering caused by a nearby subduction earthquake, the giant Mw9.5 Valdivia earthquake that occurred 36 hours before the eruption (Barrientos & Ward 1990; Lara et al. 2004).

The most recent eruption started explosivelyon 4 June 2011 after 2 months of shallow seismicity (Bertin et al., 2015). The phase of most intense explosive activity lasted for about 72 hours, when ca. 0.96 km^3 of tephra was erupted(0.75 km^3 the first two days) as estimated by Pistolesi et al. (2015)based on a detailed stratigraphic analysis aided by satellite imagery. Considering the upper bound value of 750 kg/m^3 for density of the juvenile fragments measured by these authors, the corresponding dry rock equivalent (DRE) volume of the tephra would be 0.27 km^3.

After several days of waning intensity of the explosive phase, an effusive stage started on 15 June at very high rates that peaked near 70 m^3/s a week later (Bertin et al., 2012; Tuffen et al., 2013). Effusion rates then gradually decreased over subsequent months and the eruption terminated between June and August 2012 with ca. 0.5 km^{3}of erupted lava (Bertin et al., 2012). Summing the DRE volume of the explosive phase and this volume of lava, the total erupted volume was ca. 0.77 km^3.

Lava and tephra deposits of the eruption have been analysed to derive properties of the magma and its pre-eruption conditions (Castro et al., 2013; Jay et al., 2014; Alloway et al., 2015). Particularly, major and trace element analyses of Alloway et al. (2015) point to three distinct magma bodies contributing to the eruption, which these authors suggest could be structurally controlled by the complex spatial association between the NW-oriented PCCVC and the LOFZ. In addition, analytical and experimental petrologic results presented by Castro et al. (2013) suggest that the hybrid activity of the eruption (combining explosive and effusive phases) was likely fed by a dike allowing simultaneous eruption of variably degassed magma patches.

A possible structural control on this eruption as inferred by these authors fits perfectly into the geological context of the PCCVC and suggests that poorly studied but largely dangerous eruptions of viscous acidic magma could be more likely generated under such control. Indeed, the only other well-documented hybrid acidic eruption occurred in 2008 at Chaitén volcano in Southern Chile and was controlled by active structures of its basement as demonstrated by modelling surface deformation recorded by Interferometric Satellite Aperture Radar (InSAR) images (Wicks et al., 2011) and Global Positioning System (GPS) observations (Piña-Gautier et al., 2011). However, similar studies on Cordón Caulle eruption 2011 (Jay et al., 2014; Bignami et al., 2014) did not consider an explicit control of crustal

structures on co-eruptive surface deformation observed by InSAR, but used point sources embedded in an elastic medium (Mogi 1958) to model the deformation (Jay et al., 2014). In this contribution, we model SAR interferograms between February and December 2011 using Mogi point sources and alternative dike-like sources in an elastic medium (Okada 1985), which we combine with continuous GPS data and locally recorded seismicity in order to evaluate the possible control exerted by the structural grain below PCCVC on the onset and evolution of its recent eruption.

3.4 Previous studies on surface deformation at PCCVC

Deformation patterns of volcanoes have been studied by InSAR in the phase of stress accumulation (e.g. Pritchard &Simons 2004a; Fournier et al., 2010 for the Southern Andes) as well as during eruptions (e.g. Froger et al., 2004; Biggs et al., 2010; Wicks et al., 2011). Previous InSAR-based studies for volcanoes of the Southern Volcanic Zone (SVZ) of the Andes recognised a notable surface deformation at PCCVC years before the 2011 eruption. Pritchard &Simons (2004a) using ERS data from 1996 and 1999 observed a subsidence equivalent to a rate of about 3 cm/yr, in a region coinciding with the NW-oriented Cordón Caulle graben at its intersection with the Cordillera Nevada Caldera. Fournier et al. (2010) observed inflation of the same region whose rate increased from about 1 cm/yr in 2003-2005 to almost 20 cm/yr in 2007-2008. This surface deformation signal was attributed to a volume increase of 0.06 km^3 distributed among 2 point sources at 7 km and 4 km depth coinciding the first with the intersection of the graben with the caldera rim and the second at the centre of the graben near the 2011 eruptive vent. Pritchard et al. (2013) analysed the effect of the 2010 Mw 8.8 Maule earthquake on SVZ volcanoes finding coseismic subsidence at several volcanoes within 300 km of the epicentre.
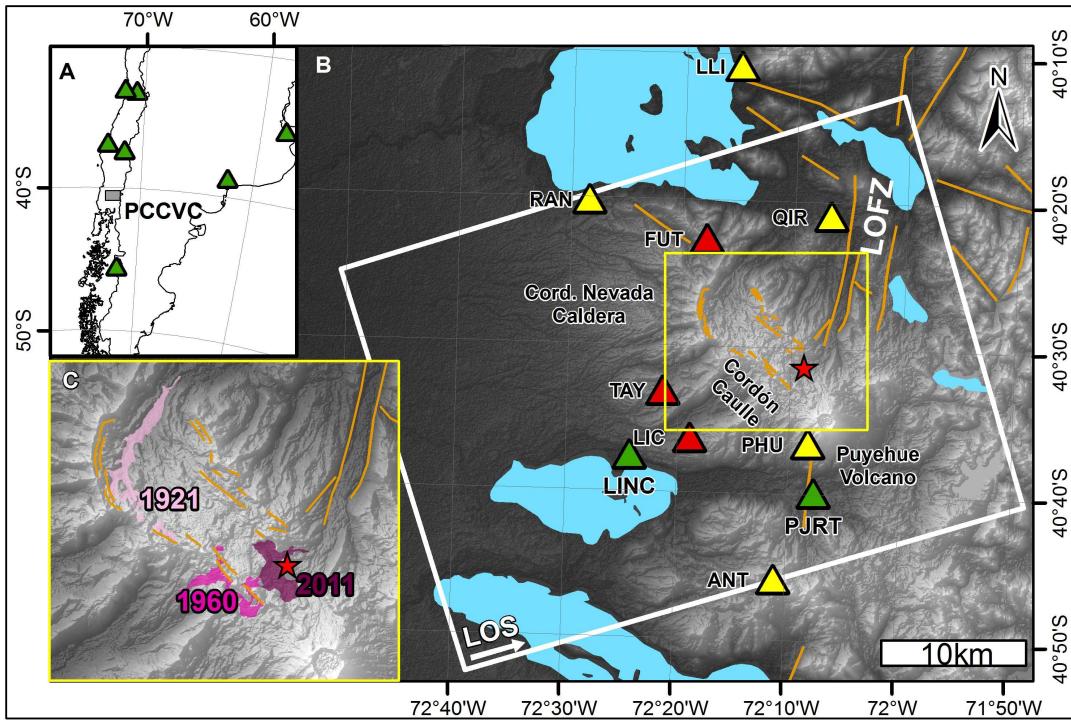
Figure 3.1 Tectonic setting of the Puyehue-Cordón Caulle Volcanic Complex (PCCVC). A) Location of the study area in the Chilean Southern Andes. Green triangles show seven of the 16GPS stations used in the GPS processing. B) Digital elevation model of the SRTM-3, white rectangle marks the Envisat scene (white arrow labelled LOS indicates the line-of-sight direction), main faults and lineaments are mapped in orange, Liquiñe-Ofqui Fault Zone (LOFZ) extracted from the literature (e.g. Lara & Moreno, 2006), red star: the location of the vent activated during the June 2011 eruption, green triangles: continuous GPS stations installed days after the eruption, yellow and red triangles: seismic stations installed before and after the start of the eruption. The yellow box marks the extent of C) Detail of the PCCVC showing the distribution of lava flows generated during the eruptions of 1921, 1960 (Lara et al., 2006) and 2011 (see e.g. Bertin et al., (2015) for a detailed analysis of lava emplacement). Note their coincidence with NW structures forming the walls of the Cordón Caulle graben. Fuente: Wendt et al. (2017).

The PCCVC is located at a distance of 500 km but showed an abnormal uplift signal of about 10 cm within a month of the earthquake. Previous InSAR analysis of the 2011eruption has shown that it was accompanied by a large subsidence centred in the Cordillera Nevada caldera with a smaller peak west of Puyehue volcano just at the beginning of the eruption (Jay et al., 2014; Bignami et al., 2014). Jay et al. (2014) used point sources embedded in an elastic medium (Mogi 1958) to model the co-eruptive surface deformation as produced by in total three deflating sources at depths between 3 and 6 km, which are consistent with the depth range estimated for the pre-eruptive magma reservoir based on their petrological analysis. Two of these co-eruptive sources showed signs of inflation since 2007.

Additionally, Jay et al. (2014) analysed the gas content of the erupted lava in order to estimate the compressibility of the magma, which is necessary to relate the modelled volume change the depth with the actually erupted volume.

3.5 Data and Methods

3.5.1 InSAR Processing

We analysed Envisat ASAR Image Mode data acquired between February and December 2011 (Table 3.1) that cover the months before and after the onset of the eruption. Scenes were recorded in ascending orbit in image swath IS6 with a high incidence angle of about 41°. Therefore, they exhibit less distortion of layover and foreshortening than data taken at steeper incidence angles. Since differential interferograms are sensitive to deformation, topography and atmospheric refraction, these effects have to be accounted for. While the effect of topography in the interferogram depends on the perpendicular baseline Bn between the acquisitions, deformation directly translates into interferometric phase scaled by the radar wavelength. For Envisat ASAR data one fringe – a phase change of 2π – corresponds to 2.8 cm of deformation along the satellite line-of-sight direction (LOS).

Date1	Date2	Interferogram	B_n [m]	H_a [m]
2011-02-07	2011-03-09	2011-02/2011-03	45.7	335.3
2011-03-09	2011-04-08	2011-03/2011-04	230.0	66.6
2011-04-08	2011-05-08	2011-04/2011-05	-240.8	-63.6
2011-05-08	2011-06-07	2011-05/2011-06	-98.4	-155.7
2011-06-07	2011-07-07	2011-06/2011-07	153.2	100.0
2011-07-07	2011-10-05	2011-07/2011-10	-265.2	-61.1
2011-10-05	2011-12-04	2011-10/2011-12	150.7	108.2

Table 3.1 List of Envisat scenes over PCCVC used in this study. The table lists the dates of the two acquisitions, the name of the interferogram used in the text, the perpendicular baseline Bn and the height of ambiguity Ha. Fuente: Wendt et al. (2017).

Interferometric analysis of the Envisat data was done with the Gamma software (Werner et al., 2000). From each consecutive image pair, a differential interferogram with the shortest possible time span was computed (Fig. 3.2) omitting acquisitions from August and September

that showed low coherence probably caused by wet snow cover. Differential interferograms were processed with 1x5 looks in range and azimuth direction, filtered by an adaptive filter based on the local fringe spectrum (Goldstein & Werner, 1998) and masked using a coherence threshold. These interferograms forma time series of consecutive time steps covering the months before and after the onset of the eruption. The topographic component of the interferometric phase was removed using the Digital Elevation Model SRTM-3 derived by the Shuttle Radar Topography Mission in 2000 (Farr et al.,, 2007). Perpendicular baselines range from 18 m to 265 m (Table 3.1) resulting in different sensitivities to topography. Even for the interferograms with the largest baselines, the height of ambiguity Ha equivalent to a phase change of 2π in the interferogram amounts to about 60 m. The nominal accuracy of the SRTM topography is in the order of 6 m (Rodríguez et al.,, 2006), although higher errors can be expected in areas of high relief such as volcanoes. Converted into deformation this nominal height error corresponds to about 3 mm in LOS, which is a negligible fraction (less than 2 %) of the observed signal in the interferograms during the eruption. In contrast to the topographic contribution that can be corrected reliably, the effect of tropospheric refraction is more difficult to assess. Therefore, we use the available pre-eruption interferograms (Figure 3.2 A-C) to estimate the magnitude of the tropospheric effect, although there could be more pronounced differences in atmospheric conditions than sampled in these three interferograms. The resulting phase signal seen in interferograms 2011-02/2011-03 and 2011-03/2011-04 (Figure 3.2 A, B) that is correlated with elevation is typical for a phase delay caused by the propagation through a layered atmosphere resulting in a differential signal between the base and the top of a topographic feature (e.g. Beauducel et al., 2000). At Llaima volcano also located in the Southern Volcanic Zone, Remy et al. (2015) observed a vertical phase gradient of up to 35 mm/1000 m related to precipitable water vapour. The two fold phase pattern of ± one fringe (2.8 cm in LOS) in the northern part of the April interferogram 2011-04/2011-05 (Figure 3.2 C), that was interpreted as deformational signal by Jay et al. (2014), is not correlated with topography and is thus more difficult to attribute unambiguously to either a tropospheric or deformational signal. In any case, it is neither clear subsidence nor uplift, and its amplitude does not exceed significantly the signal in the other pre-eruptive interferograms. The root mean square in these interferograms is indicative of the uncertainty caused by unmodelled effects. RMS values of 0.40 fringes, 0.34 fringes and 0.76 fringes for 2011-02/2011-03, 2011-03/2011-04 and 2011-04/2011-05, respectively, convert to a deformational signal in LOS of 11 mm, 10 mm and 21 mm, thus two orders of magnitude less than the signal observed in the interferogram 2011-05/2011-06 spanning the beginning of the eruption

(Figure 3.2D). The deformational signal in this interferogram with dense concentric fringes is clearly restricted to the volcanic complex, whereas the lowland in the west shows almost constant phase.
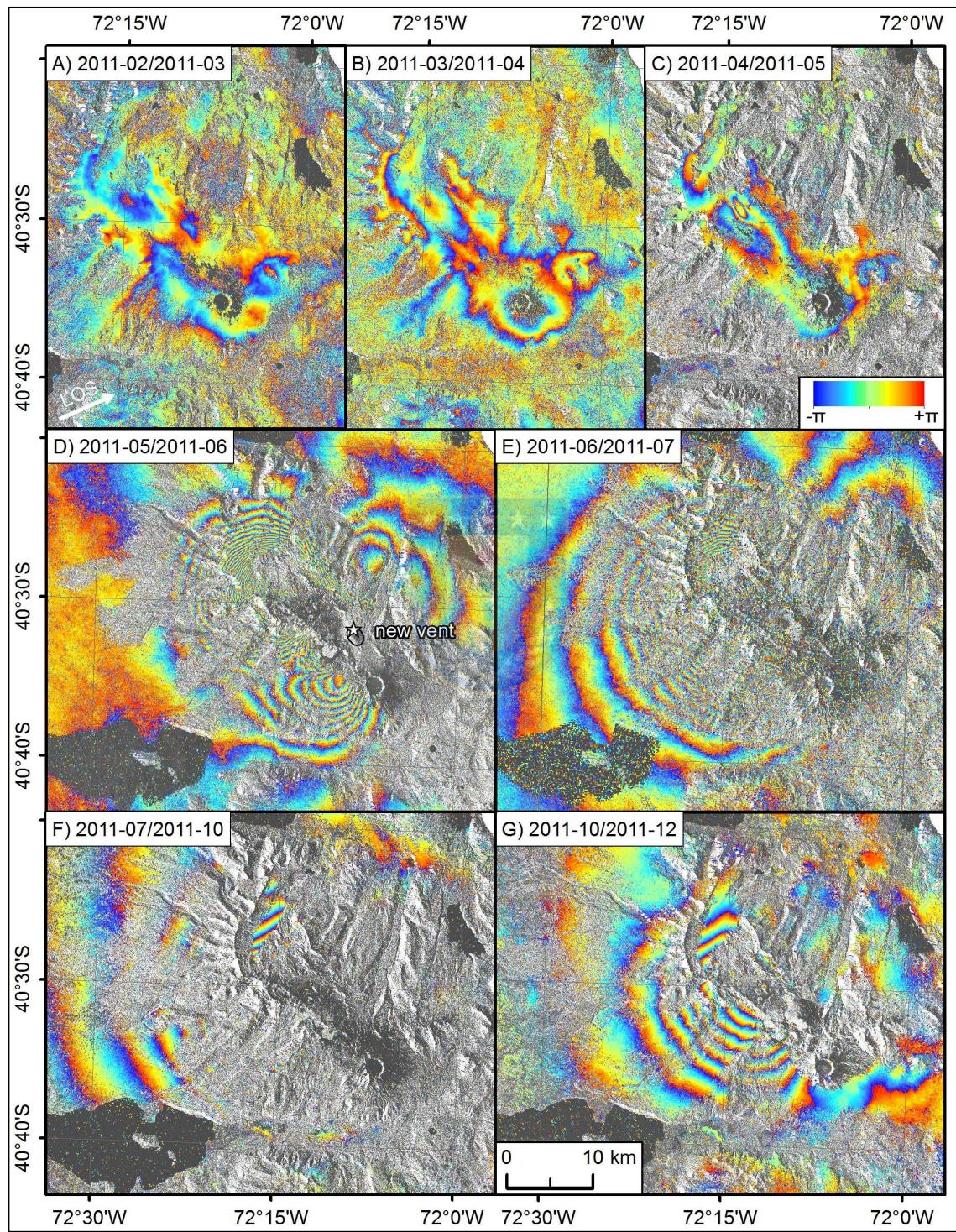
Figure 3.2 Envisat differential interferograms of PCCVC, upper row: pre-eruptive interferograms showing good coherence on the plateau and mainly tropospheric signal, middle row and lower row: co-eruptive interferograms all showing deflation of the edifice. The eruptive vent is marked by a star in D) together with the outline of the ash plume that is only visible in the amplitude image acquired on 6 June. Fuente: Wendt et al. (2017).

Interferograms after the start of the eruption show a considerable reduction in coherence with respect to pre-eruptive scenes. The densest part of the ash plume is faintly visible in the amplitude image taken three days after the start of the eruption (background of Fig. 3.2D, ash plume trace towards the SE of the new vent marked in black). Nevertheless, the incoherent part is considerably larger and stretches in the upwind direction, meaning that the ash plume is not solely responsible for decorrelation. The loss of coherence is rather attributed to the high fringe rate near the centre of the deformation in the interferogram spanning the onset of the eruption, additionally to the effect of changes in the ash deposits in all the interferograms. While phase unwrapping using the minimum cost flow method algorithm (Werner et al., 2003) did not pose any problems on pre-eruption interferograms, large phase gradients resulting in loss of coherence near the centre of deformation and fresh tephra deposits inhibited robust automatic phase unwrapping in the co-eruptive interferograms. Therefore, phase has been unwrapped by georeferencing fringes in order to avoid phase unwrapping errors and to downsample the data. This leads to an uneven distribution of data points, but the large incoherent areas have the same effect.

Each interferogram provides the projection of the three-dimensional deformation onto its line of sight (LOS). Ideally, data from ascending and descending tracks and different incidence angles are combined to resolve the three components of the displacement (Wright et al., 2004). In the case of PCCVC there are only Envisat data from an ascending orbit available, providing one projection of the three-dimensional deformation vector onto the LOS of the satellite (unit vector [-0.60, -0.26, 0.75] in East, North, Up coordinates). Thus, the observed LOS displacement is less sensitive to movements in north-south direction.

The interferogram 2011-05/2011-06 (Fig. 3.2D) covers the first three days after the onset of the eruption on 4 June. It shows an increase in LOS distance (surface moves down and/or to the east) of up to 1.2 m collocated with the Cordillera Nevada caldera rim and a less prominent and less coherent LOS increase signal along the Cordón Caulle graben toward the

eruptive vent. East of the graben, a decrease in LOS distance is observed, i.e. a deformation towards the satellite. The second eruptive interferogram 2011-06/2011-07 (Fig. 3.2E) shows an expansion of the deforming area toward the base of the complex with a more concentric distribution of fringes compared with the first co-eruptive interferogram and a less intense increase in LOS distance (up to 0.8 m at Cordillera Nevada caldera centre). The subsequent interferogram 2011-07/2011-10 covers a larger time span of 90 days because interferograms constructed using intermediate SAR scenes have significantly lower coherence due to snow cover and less deformation. Interferogram 2011-07/2011-10 has generally less coherence over the Cordón Caulle plateau and shows a concentric pattern of small-amplitude LOS increase, similar to the one observed in interferogram 2011-10/2011-12 covering 60 days until beginning of December 2011.The lower magnitude of deformation in these two interferograms makes them more susceptible to tropospheric effects that could contaminate the deformational signal.

3.5.2 Continuous GPS data

On 12 June, a few days after the start of the eruption, a preexisting campaign GPS site marked in bedrock (LINC, see Figure 3.1) was reoccupied with a dual-frequency continuously recording GPS receiver (CGPS).After another 6 days, the CGPS site PJRT was installed in a stable zone of soil and marked by a steel monument similar to the shallow drilled braced monument of UNAVCO (http://kb.unavco.org/kb/article/shallow-drilled-braced-monument-overview-301.html) to exclude monument instabilities. The data of these two sites were processed within a continental GPS network consisting of 16 IGS stations using the Bernese GPS Software V5.0 (Dach et al., 2007) applying precise orbit and Earth rotation parameters from IGS final products (Dow et al., 2009). More details about our processing strategy can be found in Bedford et al. (2013). For the datum definition of the GPS network we use the minimum constraint approach, applying the No Net Rotation and No Net Translation conditions for a group of selected reference stations, and therefore our results are compatible with ITRF2008 (Altamimi et al., 2007). The coordinates are reduced to a South American fixed frame, using a selected number of tectonically stable stations, which are located in the craton of the continent. Because the 2010 Maule earthquake occurred only 15 months earlier, the whole region was still subject to postseismic deformation. Due to the distance of more than 200 km between the southern limit of the Maule rupture zone and PCCVC, both the effects of afterslip and viscoelastic relaxation are considerably attenuated (Klein et al., 2016). Measured as well as modelled postseismic deformation in the region were steadily decreasing

throughout the second year after the earthquake and ranged as low as 10 to 20 mm/yr horizontally and less than 6 mm/yr vertically in the region of PCCVC (Klein et al., 2016), i.e. well below the observed signal.

3.5.3 Seismicity

Before 2010, the seismic network of the Observatorio Volcanológico de los Andes del Sur (OVDAS, Southern Andes Volcano Observatory belonging to SERNAGEOMIN, the Chilean Geological Survey) around PCCVC was composed by only two vertical short period stations (RAN and LLI in Figure 3.1). These stations showed a significant increment of the seismic activity (swarms with Local Magnitude $Ml= 4.0$) between June 2007 and January 2008, in coincidence with the notable shallow deformation evidenced by InSAR (Fournier et al., 2010; Jay et al., 2014). During the next three years (February 2008-January 2011), the seismic activity decreased and focused in the Cordillera Nevada caldera. After the 2010 Maule earthquake, three new broadband seismic stations (30 seconds) were installed around the volcano (QIR, PHU, ANT, Fig. 3.1) and previous short period stations were replaced by broadband instruments. After the eruption, three additional stations were installed (TAY, FUT, LIC) to complete a network of eight broadband stations around the complex.

The categorization of the seismic activity was made using the classification proposed by Lahr et al. (1994) and Chouet (2003), classifying about 14,000 earthquakes in 2011. From this database, around 1500 events were initially located with 47% recorded between 16 April and the day of the eruption. The recorded seismicity was relocated using VELEST (Kissling 1988; Kissling et al., 1994) in order to improve the 1D velocity model and establishing the corresponding delay times at each station via simultaneous mode Joint-Hypocentre-Determination (JHD). Details of data, methods and results regarding the seismicity before and during the eruption will be presented in another paper (Basualto et al.,, in preparation). Table 3.2 shows the obtained velocities for compressional and shear waves Vp and Vs as a function of depth representing the final velocity model. Finally, the JHD procedure generated a seismicity catalog of 425 high quality events (more than eight seismic phases; gap stations locations <180°) divided in two different periods, before (174 events) and after (251 events) the start of the eruption. The final data solutions have a root mean square RMS<0.15 and horizontal and vertical errors less than 0.65 km.

Depth (km)	Vp (km/s)	Vs (km/s)
0.5	4.9	2.75
1.5	5.05	2.84
2.5	5.1	2.87
3.5	5.15	2.89
4.5	6.05	3.4
5.5	6.38	3.58
6.5	6.46	3.63
7.5	6.47	3.63
8.5	6.5	3.65

Table 3.2. Seismic velocity model resulting after seismicity relocation process. The table shows values of Vp and Vs with depth. Fuente: elaboración propia.

3.6 Modelling sources of co-eruptive surface deformation observed by InSAR

In order to assess the sources of the deformation pattern observed in the InSAR interferograms, analytical models were applied to relate subsurface volume change and displacements to surface deformation. To invert the first interferogram covering the onset of the eruption, 2 point sources (Mogi 1958) aligned approximately with the local maxima of deformation were assumed. For both sources, the exact centre coordinates and the parameters source depth and volume change were solved for iteratively. To derive the best-fitting parameters, the parameter space was searched for by uniform random sampling (Sambridge & Mosegaard 2002) to find the model that minimises the misfit represented by the root mean square (RMS) of the differences between model and data at the sampled points. The resulting horizontal position (Fig. 3.3A) is located to the east of the maximum deformation recorded in the interferogram, because this maximum is the sum of vertical deformation (maximum above the source) and horizontal one (towards the source, relevant mainly east-west with opposite

maxima on either side of the source) projected onto LOS. The region of positive LOS displacement east of the northern source is also a result of the horizontal displacement towards the source and does not reflect uplift as could be erroneously assumed if only vertical deformation were considered. Best fit was achieved for a deflating northern source below Cordillera Nevada caldera with a volumetric change of -0.096 km^3 at a depth of 3400 m and a second one below the intersection of the graben with the LOFZ near Puyehue volcano with a deflation of -0.017 km^3 at a depth of 3900 m (Table 3.3, Figure 3.3A). The RMS value between data and model amounts to 0.054 m, and the model accounts for 87% of the total signal RMS. However, as the deformation is proportional to volume change and inversely proportional to source depth, there is a trade-off between the two parameters (e.g. Pritchard & Simons, 2004b), meaning that a smaller and shallower source can produce a similar deformation pattern as a larger, but deeper one. Additionally, the availability of only one projection of the 3D deformation onto the look direction of one satellite path does not allow separating between horizontal and vertical displacement. The polar orbit with an almost NS flight direction results in a low sensitivity to deformation in this direction.
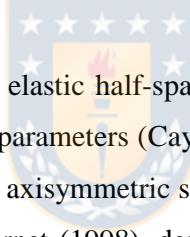
Assessing a deformation in an elastic half-space and thus neglecting the presence of topography affects the derived source parameters (Cayol & Cornet 1998), but the influence at PCCVC is less severe than at a typical axisymmetric stratovolcano because the slopes are less pronounced. As stated in Cayol & Cornet (1998), depth values have to be considered depth below the plateau level of 1500 m. Our modelled Mogi sources are similar in both spatial location and amplitude compared with those reported by Jay et al. (2014).
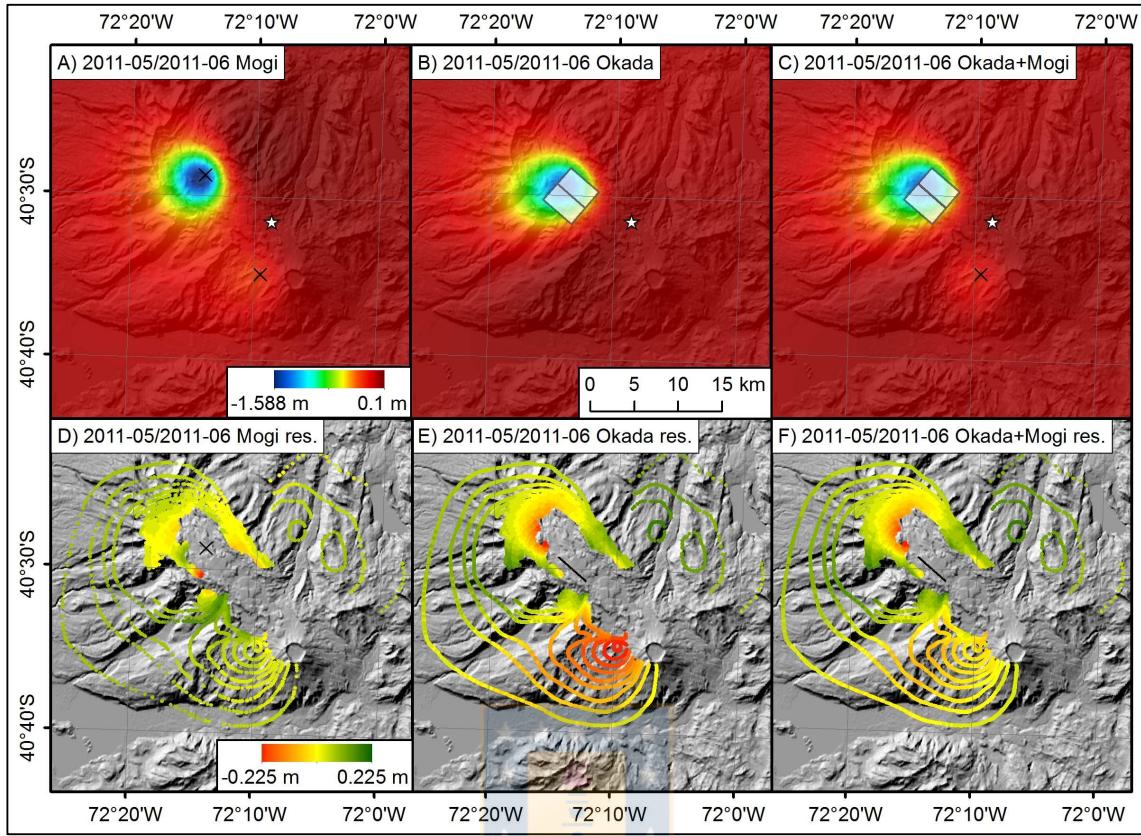
Figure 3.3 Different models for the interferogram in Figure 3.2 D). upper row: modelled LOS displacement, lower row: residuals. Scales in A) and D) refer to all subfigures in the respective rows; source centers are marked by crosses. Black line in B), C), E) and F) shows the trace of the center line of the dike with the grey plane depicting its extent. The eruptive vent is marked by a star. Fuente: Wendt et al. (2017).

In order to evaluate the possibility of a structural control on eruption onset and considering that the eruptive vent is located along the Cordón Caulle graben to the southeast of the deforming region below Cordillera Nevada caldera, we also test a closing (deflating) dike structure oriented NW-SE along the graben assuming in this case the analytical approximations of Okada (1985). In comparison with the Mogi model, more parameters have to be adjusted for the Okada model, i.e. the geometry of the fault (central position, length, depth and width, strike orientation), direction of slip in terms of dip and rake, slip magnitude in the rake direction and opening perpendicular to the fault plane. We fixed geometric parameters following the geological structure of the graben (e.g. Lara et al., 2006; Sepúlveda et al., 2005; García 2015) and in consistency with seismicity presented below. The remaining free parameters were modelled searching for the minimum misfit with a Monte-Carlo method.

Different tests especially for the dip of the dike were performed, because the dip of the walls of the graben is supposed to decrease with increasing depth forming a trough (Sepúlveda et al., 2005; García 2015).

The best result was obtained for a combination of closing of a dike-like structure and oblique left-lateral normal movement along the walls of this dike (Table 3.3, Figure 3.3B), a model with an RMS of 0.082 m. Additional tests were done to evaluate two extreme cases with only closing or only slip along the dike, both giving a worse fit. Without a slipping component, the inversion results in a deep (7400 m) horizontal sill with a closing of 5 m and an RMS of 0.183 m. The second test precludes any component transverse to the dike and thus any volume change, and therefore cannot explain the transfer of magma to the eruptive vent. This setting would result in a deeper dike than the combined model with a slip of about 9 m and an RMS of 0.086 m. The performance of the preferred model of combined slip and closing is slightly weaker than for the Mogi sources and accounts for 76% of the total signal RMS. Taking the amount of closure and the dimensions of the dike into account, the change in volume is -0.062 km^3, about half of the one predicted by the Mogi sources.
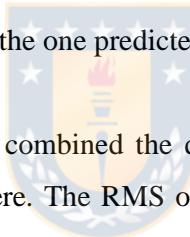
As an additional exercise, we combined the dike with the southern Mogi source to compensate for the large residuals there. The RMS of the combined model is 0.072 m. The bulge of LOS increase in the south cannot be completely offset by the Mogi source, but the fit between data and model is considerably improved. The total volume change at depth is -0.078 km^3 for this combined scenario.

Deformation observed for the second co-eruptive interferogram 2011-06/2011-07 covering the waning stage of the explosive phase and the initiation of the effusive phase (Figure 3.2E) was modelled with a single point Mogi source (Figure 3.4) estimating a volume change of -0.169 km3 at a depth of 5200 m. The RMS between data and model amounts to 0.022 m and explains 94% of the signal RMS.

Interferograms 2011-07/2011-10 (90 days), and 2011-10/2011-12 (60 days), were also modelled by single Mogi sources. The best-fit model of the former one has an RMS of 0.008 m accounting for 87 % of the signal RMS, while the latter results in an RMS of 0.011 m explaining 85%.While Jay et al. (2014) assume a common source location for all interferograms after 7 June, source location is adjusted for each interferogram independently in our approach. Although the source seems to move successively deeper and slightly towards

the new vent, this should be interpreted with caution because of the tropospheric contamination that is more pronounced in these interferograms with smaller deformation. The estimated volume change rates are considerably smaller than in the first month of eruption. In general, our volume estimates agree with the ones of Jay et al. (2014) within about 25%.

Interferogram 2011-05/2011-06, 30 days, Mogi models								
Location (UTM 18S)	Depth [m]	Volume [km³]	RMS [m]					
734500 m E, 5515300 m N	3400	-0.096	0.054					
740600m E, 5504100 m N	3900	-0.017						
Interferogram 2011-05/2011-06, 30 days, Okada model								
Location (UTM 18S)	Depth [m]	Length[*] [m]	Width[*] [m]	Strike[*] [°]	Dip [°]	Rake [°]	Slip [m]	Open [m]
735000 m E, 5513000 m N	5500	4250	7250	139	42	-47	6.3	-2.0
		Volume [km³]	RMS [m]					
		-0.062	0.082					
Interferogram 2011-05/2011-06, 30 days, Okada + Mogi model								
		Volume [km³]	RMS [m]					
		-0.078	0.072					
Interferogram 2011-06/2011-07, 30 days, Mogi model								
Location (UTM 18S)	Depth [m]	Volume [km³]	RMS [m]					
736100 m E, 5514200 m N	5200	-0.169	0.022					
Interferogram 2011-07/2011-10, 90 days, Mogi model								
Location (UTM 18S)	Depth [m]	Volume [km³]	RMS [m]					
736800 m E, 5512500 m N	5700	-0.077	0.008					
Interferogram 2011-10/2011-12, 60 days, Mogi model								
Location (UTM 18S)	Depth [m]	Volume [km³]	RMS [m]					
738250 m E, 5513100 m N	6200	-0.047	0.011					

Table 3.3 Parameters of best-fitting models for the co-eruptive interferograms. For the Mogi models, Location, depth and volume change were adjusted for. For the Okada model, fixed parameters are

marked with an asterisk. RMS values after the adjustment are listed as well. Fuente: Wendt et al. (2017).
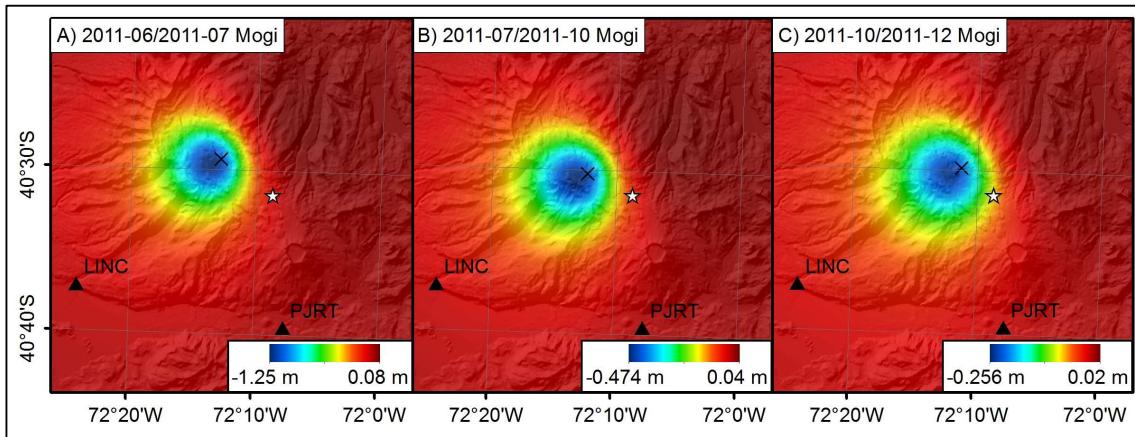
Figure 3.4 Model of LOS deformation in interferograms in Figure 3.2 E), F) and G).Black cross marks the location of the respective Mogi source, black triangles indicate GPS sites, note different colour scales. The eruptive vent is marked by a star. Fuente: Wendt et al. (2017).

3.7 GPS-Derived deformation

Time series of displacement for the two GPS sites situated in the south and southwest of the volcanic complex (Fig. 3.5) start during the second co-eruptive interferogram (2011-06/2011-07). During this timewindow both sites show a rapid displacement of 51 mm towards northeast in the case of LINC and of 19 mm to the north in the case of PJRT. The vertical component, although more noisy, shows a notable subsidence with values on the order of 20 mm in LINC and about 200 mm in PJRT. This phase of rapid subsidence abruptly declined near 2011-07-07 coinciding with the day when the scene forming the interferograms 2011-06/2011-07 and 2011-07/2011-10 was taken by the satellite. The surface deformation recorded by both CGPS stations afterwards (between July and December 2011) maintains its azimuthal direction at lower rates. While PJRT remains vertically stable for the rest of the observed period, LINC shows a clear uplift starting in August, amounting to a net uplift of several centimetres compared to the beginning of the observations.

To compare the GPS displacement with InSAR-derived source models we first calculated a linear trend for the three components (N, E, U) of the time series at both CGPS stations (Figure 3.5) for the time spans of the particular InSAR scenes and then we projected

the 3D deformation along the LOS of the SAR satellite. A direct comparison of GPS deformation and InSAR data would otherwise be restricted to LINC because PJRT is surrounded by forest and does not show a coherent signal in the interferograms.

Therefore, we computed the predicted 3D deformation at the position of both CGPS stations from the source models determined in section 4. Considering that the CGPS stations started data recording eight (LINC) and fourteen (PRJT) days after the initiation of the eruption, the recorded deformation cannot be compared with the predictions of the source models derived from interferogram 2011-05/2011-06. Results of the comparison between measured and modelled displacements for the subsequent interferograms are listed inTable 3.4.
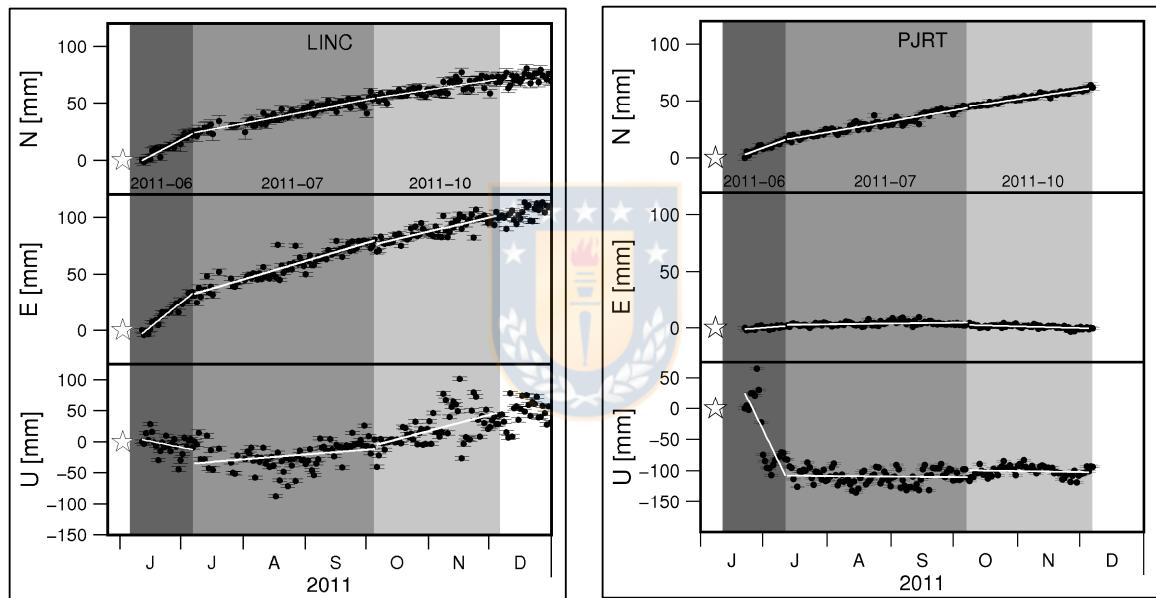
Figure 3.5. Time series of daily solutions for northern (N), eastern (E) and vertical (U) component at continuous GPS stations LINC (left) and PJRT (right) starting 12 June and 18 June respectively. Displacements are relative to the South American craton; for processing details see section 3.2. Black dots are daily solutions with error bars, star marks the day of the eruption initiation (4 June). The time span of interferograms covering the time series are highlighted in different grey levels and indicated at the bottom of the North panel; white lines depict linear trends for the time spans of the individual interferograms as listed in Table 3.4. Fuente: Wendt et al. (2017).

	LINC				PJRT			
	East	**North**	**Up**	**LOS**	**East**	**North**	**Up**	**LOS**
	2011-06/2011-07 (30 days)							
GPS	0.043	0.028	-0.020	-0.048 ± 0.011	0.004	0.019	-0.200	-0.158 ± 0.030

Mogi	0.057	0.050	-0.017	-0.060 ± 0.020	-0.028	0.067	-0.016	-0.020 ± 0.020
2011-07/2011-10 (90 days)								
GPS	0.047	0.030	0.023	-0.019 ± 0.008	0.002	0.028	-0.003	-0.010 ± 0.004
Mogi	0.029	0.021	-0.010	-0.031 ± 0.020	-0.015	0.043	-0.014	-0.013 ± 0.020
2011-10/2011-12 (60 days)								
GPS	0.025	0.016	0.052	0.020 ± 0.010	-0.003	0.016	-0.003	-0.005 ± 0.003
Mogi	0.015	0.011	-0.005	-0.016 ± 0.020	-0.006	0.025	-0.008	-0.009 ± 0.020

Table 3.4. Displacements (in m) both measured and modelled at GPS sites LINC and PJRT for the time span of the individual interferograms. For the LOS component uncertainties for both GPS and MOGI are given. Fuente: Wendt et al. (2017).

As expected, the modelled horizontal displacements point towards the centre of deformation (Fig. 3.6). The observed GPS vectors differ from this direction by 6° for LINC and by 23° for PJRT. For interferogram 2011-06/2011-07, displacements measured at LINC agree with those computed from the Mogi source model within uncertainties. For the station PJRT horizontal movement derived by GPS for the time of interferogram 2011-06/2011-07 is of smaller magnitude than the modelled one. On the contrary, measured subsidence is one order of magnitude larger than predicted by the model. Unfortunately, this large deformation cannot be verified by InSAR directly because of the low coherence in this area, but the difference between model and observation is well above the error bound of the GPS measurements. The residual displacement at PJRT comparing the observation with the model prediction is 0.06m in SE direction and a subsidence of 0.18 m. Any monument instability or local effect can be excluded, because the station has a steel monumentation as it is conventionally used for CGPS sites and is installed in a locally stable zone. However, this additional local effect could be related to the location of PJRT in the trace of the LOFZ pointing to a possible movement of the structure during the eruption.
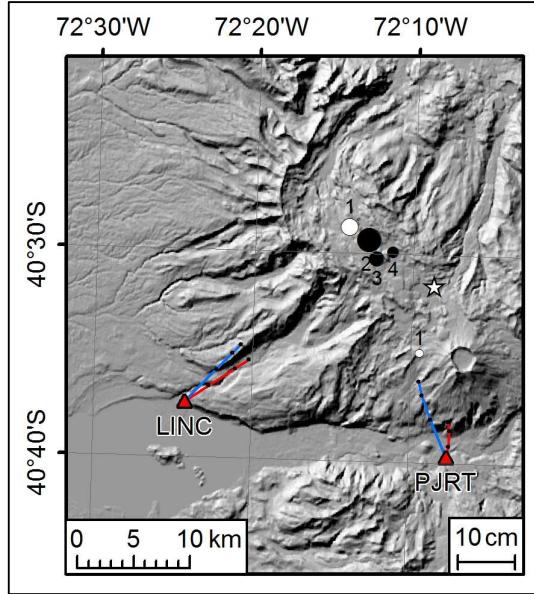
Figure 3.6 Map view of the GPS derived displacement vectors in red and the modelled vectors in blue. Mogi sources derived from the InSAR data that correspond to the deformation steps are depicted as black circles (2-4) and scaled in accordance to their volume change; the first Mogi sources not covered by GPS observations are drawn in white for completeness. The eruptive vent is marked by a star. Fuente: Wendt et al. (2017).

In the case of interferograms 2011-07/2011-10 and 2011-10/2011-12, we note that the horizontal displacement observed at LINC is well reproduced by the prediction of the Mogi sources modelled from InSAR deformation. However, the uplift starting in August cannot be explained by a deflating Mogi source. While this disparity in the observed and modelled vertical displacement could point to the existence of rheological and/or geometrical complexity in the dynamics of the system that is not captured by the simple Mogi model, a non-tectonic seasonal signal cannot be excluded. Such seasonal vertical displacements are known from many GPS sites and are often related to atmospheric or local hydrological loading effects (e.g. Bevis et al., 2004; Bos et al., 2010; Tregoning & Watson 2009). Although the neighbouring PJRT station does not show a significant vertical movement in 2011after the pronounced initial subsidence in June, newer data of that site reveal seasonal height changes with a minimum in winter also typical for other stations in the region, but of smaller amplitude (Báez, personal communication). The deformation recorded by PJRT between July and September shows a northward displacement and no significant vertical movement, while the Mogi model predicts a larger movement towards NNW and subsidence

comparable to that at LINC. The horizontal residual amounts to 0.028 m towards SE. For the last time period (interferogram 2011-10/2011-12) GPS-derived deformation at PRJT and the prediction of the Mogi model coincide in direction with a slightly less pronounced deformation measured than modelled.

3.8 Comparing modelled sources with seismicity

The seismic network recorded first signs of seismic unrest from February to April 2011, consisting in sporadic but significant (*Ml* 2 to 4.3) Volcano-Tectonic (VT) and some Very Long Period (VLP) events located around the Cordillera Nevada caldera and the NW part of Cordón Caulle graben. During the next month, magnitude and frequency of seismicity gradually increased and expanded to the whole Cordón Caulle graben inside its bounding structures (Fig. 3.7A, NW-SE lineament). Few days before the eruption, the seismicity rapidly increased in magnitude and frequency and concentrated near the surface. At this stage, earthquakes were characterised by a blend of VT, hybrid (HB), and VLP sources. Similar seismicity with a mixture of different types were for instance recorded a few days before the eruption of Mount St. Helens (Qamar et al., 1983; Main 1987) and Augustine Volcano (Jacobs & McNutt 2011) and has been associated with the movement and/or ascent of magmatic fluids. Events were located along the NE wall of the Cordón Caulle graben at shallow depths and in a NE-SW oriented branch in the south (Fig. 3.7A, southern blue dots), suggesting the participation of another structure in the last phase, possibly related to an unmapped secondary branch to the LOFZ.

Figure 3.7B shows the hypocentres recorded after the onset of the eruption (5 June – 20 July) indicating a more heterogeneous distribution of VT events along the graben with depths dominantly shallower than 5 km and a rapid decay of seismicity rate with time. Few events were actually recorded by the network after July (black dots in Fig. 3.7B) and they mostly concentrated at the western flank of Puyehue volcano likely along the reactivated branch of the LOFZ.

The notable concentration of seismicity along the Cordón Caulle graben and the western side of the LOFZ in the days immediately before and after the eruption strongly suggests that both structures could have experienced differential motion during the preparation phase of the eruption and in its subsequent development. This is also consistent with the location of the new active vent near the intersection of both structures.
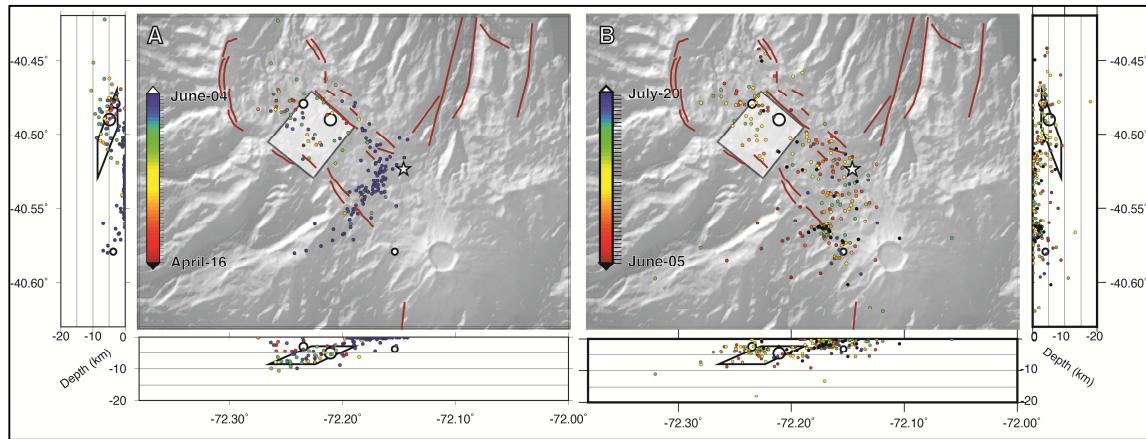
Figure 3.7 Relocation of seismicity. A: recorded from 16 April to 4 June (eruption start), B: recorded from 5 June to 27 November 2011. The colours in B represent the temporal distribution of seismicity between 5 June to 20 July. The black points in right panel are events recorded after 20 July. The red lines show the most important structures on the PCCVC. The white star represents the 2011 vent eruption. White circles mark positions of the Mogi sources with their size approximately proportional to the volume change, the Okada dike is indicated as grey rectangle. Fuente: Wendt et al. (2017).

3.9 Discussion

The structural setting in which PCCVC is emplaced, at the intersection of the trench-parallel LOFZ with an old NW-SE inherited tectonic lineament, makes it a first-order example of a volcanic complex that has been constructed under a strong structural control (e.g. Cembrano & Lara 2009; Sepúlveda et al., 2005; Lara et al., 2006; Singer et al., 2008). Particularly, Cembrano & Lara (2009) note that the acidic composition of PCCVC during the Holocene indicates the presence of a long-lived reservoir where magma have sufficient time to differentiate because NW-oriented structures forming the walls of the reservoir are dominantly compressive under a dextral motion of the LOFZ. At shorter time-scales, a structural control was also apparent during 20th century fissure eruptions, particularly for the 1960 event that was likely triggered by the unclamping of the NW-oriented faults along the Cordón Caulle graben following the Mw:9.5 Valdivia earthquake (Lara et al., 2004; Bonali et al., 2013). For the case of the recent 2011 eruption, petrological analyses of erupted material allow inferring a possible tectonic control in the storage and co-eruptive interconnection of different melt pockets feeding the eruption (Alloway et al., 2015), and in the transport of variably-degassed magma through a dike connecting the main reservoir with the eruptive vent (Castro et al.,2013). The fact that co-eruptive deflating point sources modelled by us and Jay et al. (2014) are several kilometres apart from this vent and collocated with it along the

Cordón Caulle graben can be considered indirect evidence of the activity of such a dike. In following paragraph, we will discuss our results seeking for a more direct evaluation of a hypothetical structural control on this eruption.

Interferogram 2011-05/2011-06 (Fig. 3.2D), although only spanning the first three days of the eruption, depicts a surface subsidence of more than a meter associated with a volume change at depth of 0.11 km^3 when modelled with two Mogi point sources. The largest of these sources (accounting for approx. 85% of the estimated volume change) is located near Cordillera Nevada caldera. This source roughly coincides with the main location of the inflating sources recognised by Fournier et al. (2010) and Jay et al. (2014) for the years before the eruption. This suggests that the main magmatic reservoir was located here but magma and gases were mobilised along the northern branch of Cordón Caulle graben toward the SE near its intersection with the LOFZ where the vent was finally opened. This is consistent with the spatiotemporal evolution of seismicity just before and during the first explosive phase of the eruption, with a SE expansion and shallowing of quakes inside the graben from Cordillera Nevada toward the vent. The spatiotemporal evolution of seismicity during this early stage was recorded by few local seismic stations and therefore it does not allow interpreting a clear pattern of dike propagation with a front of seismicity moving from the reservoir toward the vent. Such a spreading effect has been observed for other well-studied cases such as the 1983 dike intrusion in Kilauea (e.g. Rubin and Gillard 1998), the Dabbahu dike propagation episode in Ethiopia (e.g. Grandin et al., 2011), or more recently, Bárdarbunga volcano in Iceland in 2014 when a dike developed accompanied by propagating seismicity up to 45 km away from the deflating magma source (Sigmundsson et al., 2015).

Aiming to test the possible activity of a structure during the onset and first phase of the eruption, we intended an end-member model with respect to the point Mogi source supposing that surface deformation observed by InSAR near the intersection of Cordón Caulle graben with Cordillera Nevada in the NW was solely caused by a dike-like Okada source. We note that such an end-member model is unrealistic in the sense that the assumed structure should mostly conduct magma to the surface from a proper (deflating) reservoir from where the magma is extracted, but the exercise helps evaluating the significance of the dike-like hypothesis. The RMS error between model prediction and observation is larger for a model combining this Okada source with a small Mogi source near Puyehue volcano in the SE (0.072 m) as compared with the two Mogi point sources model (0.054 m). However, the

difference between the RMS error of both models is nearly 2% of the maximum LOS amplitude recorded by the first co-eruptive interferogram and therefore the two point Mogi sources model should be considered only slightly better than the combined dike-like Okada + small Mogi source model.

Nevertheless, these alternative models substantially differ in the derived volume changes of the magmatic reservoir at depth (-0.113 km^3 vs.-0.078km^3).Comparing these predictions against observed erupted volumes could be useful for discussing the validity of both scenarios. For this exercise, we compare our calculated volume changes at depth (ΔV) for the first three days of the eruption (derived from interferogram 2011-05/2011-06) with an erupted volume (V_e) of 0.27 km^3 of DRE magma as estimated by Pistolesi et al. (2015) for this period. The ratio $V_e/\Delta V$ depends on the ratio between the compressibility of magma (K_m) and the compressibility of the elastic media surrounding the magmatic reservoir (K_r) (e.g. Mastin et al., 2009);

$$\frac{V_e}{\Delta V} = -\left(1 + \frac{K_m}{K_r}\right). \quad (1)$$

The compressibility of magma for the case of the 2011 eruption of PCCVC was estimated by Jay et al. (2014) based on fluid content of the erupted lava to 2.1±0.4 x 10^{-10} Pa^{-1}. Given these values, equation 1 predicts that K_r should be 1.5±0.4 x 10^{-10} Pa^{-1} if all the erupted magma was extracted from the two point deflating sources. The combined model of the closing dike in the NW with the small deflating point source in the SE predicts $K_r = 8.5±4x$ 10^{-11} Pa^{-1}. We can use the seismic velocity model generated during relocation of seismicity (Table 3.2) with the relationship of Birch (1960) for calculating K_r as the inverse of bulk modulus B;

$$\frac{1}{K_r} = B = \rho\left(V_p^2 - \frac{4}{3}V_s^2\right). \quad (2)$$

For a density $\rho = 2550±150$ kg/m^3 in the shallow upper crust, the compressibility derived from the seismic model at the depth range of the modelled sources (2.5 – 6.5 km) is of the order of 2±0.1 x 10^{-11} Pa^{-1}. Both source models overestimate the value of compressibility derived from the seismic structure of the crust, although the value estimated by the dike+point model is closer to the seismic estimation as a consequence of the lower volume change at depth that is needed because part of the surface deformation is related to the slip of the dike. Alternatively, the difference between the small seismically-estimated compressibility and the higher value estimated from the source models could be explained by a strain weakening process decreasing the bulk modulus during the deformation associated with the eruption as proposed elsewhere (e.g. Gudmundsson 2004), although quantifying this effect is unclear.

As we can see, the two Mogi sources model generates a (slightly) better reproduction of InSAR-observed deformation than the combined NW Okada+ SE Mogi model, but the later requires a smaller volume change at depth which is more consistent with the volume expected from equation 1 assuming a value of rock compressibility derived from the seismic velocity model. We therefore envisage an intermediate model for the NW deformation source: a deflating Mogi source at depth with a volume change of the order of -0.03±0.01 km^3(as required by equation 1 using the value of K_r derived from the seismic velocity model) from which magma is extracted and simultaneously conducted to the surface along a slipping dike. Testing such a complex configuration is beyond the scope of our work but could be done in the future using a finite element approach considering the layered elastic properties implied by the seismic velocity model, and a point-like deflating source coupled with a slipping dike. Our Okada model predicts a left-lateral strike-slip movement of the SW-dipping dike with a large normal component accounting for a total slip of 6.3 m of the hanging wall toward the SE at a depth between 2000 m and 9000 m. Given the dimensions of the dike (Table 3) and a value of 20 GPa for the shear modulus G (as derived from the seismic velocity model using the relationship of Birch (1960) $G=\rho Vs^2$), this slip implies a seismic moment of 3.88 x 10^{18} Nm and a moment magnitude Mw=6.3. From the 425 high quality events contained in our seismicity catalog roughly half of them occurred inside the time window of the first co-eruptive interferogram. These events with local magnitudes between 0.3 and 4.9 released a total seismic moment of 1.85 x 10^{17} Nm, which correspond to a cumulated moment magnitude of 5.4.The National Earthquake Information Center PDE catalog (http://earthquake.usgs.gov/earthquakes/search/) reports 22 quakes occurring during the corresponding time interval with magnitudes ranging between 3.6 and 5. The total seismic moment accounted by these quakes is 2.35 x 10^{17} Nm with an equivalent summed magnitude Mw=5.5, very similar to the one computed with our seismicity catalog. This exercise shows that probably a small part of the slip resulting from the dike-like model could be related with seismic energy released as the dike propagated rupturing the walls of Cordón Caulle graben, with most of the motion being likely aseismic. Such discrepancy between slip and the associated released seismic moment is frequently observed during magmatic events (Pedersen et al., 2007).

Interferogram 2011-06/2011-07 (Fig 3.2E), which covers the first weeks of the effusive phase of the eruption, shows deformation over a wider area but with smaller surface

amplitude. The modelled Mogi source is located closer to the vent compared with the main point source of the earlier interferogram, but at an increased depth and producing a larger volume change at depth of 0.169 km^3. The erupted volume during the time of this interferogram comprises lava that was emitted starting 15 June after a phase of relative quiescence. Until 7 July (day of the second scene forming this interferogram), 0.10km^3 of lava was accumulated (Bertin et al., 2012), a value lower than the computed volume change at depth. This inconsistency could be caused by two reasons, or a combination thereof. On the one hand, the erupted volume could be underestimated and a significant volume of ash and gases were evacuated between 6 June and 15 June, as it is actually shown by Bignami et al. (2015).On the other hand, the volume change at depth could be overestimated because of the simplified assumptions of the Mogi approximation with respect to the more complex elastic structure of the media implied by the seismic velocity model as discussed for the first interferogram.

To assess the role of the dike during the effusive phase and to test whether analogously to the first interferogram a slipping dike would produce a smaller volume and therefore a better agreement with the erupted volume, a similar dike geometry was tested for the second co-eruptive interferogram. However, the solution tends towards a deep horizontal fault (depth > 7500 m) with only a small slip (1.9 m) but a large closing component, corresponding to a volume change at least comparable to the Mogi source. Therefore, the NW tending graben structure seems not to be active in this phase of the eruption. After all these considerations the large SSE and downward residual motion of GPS site PJRT located near the main arm of the LOFZ still cannot be explained by the Mogi source. Together with the simultaneous concentration of seismicity along the graben and near the LOFZ (Fig. 3.7), this could indicate some local effect related to the activity of these structures.

The deformation rates recorded after mid-July 2011 are rather small compared with the first month of the eruption. Our continuous GPS observations actually indicate that rates of horizontal movement strongly decrease and surface subsidence stopped near 7 July, which is the day when the SAR scene forming interferograms 2011-06/2011-07 and 2011-07/2011-10 was obtained by the satellite. The deformation signal observed at interferograms 2011-07/2011-10 and 2011-10/2011-12 can be modelled as single Mogi sources with smaller volume change (-0.077 km^3 and -0.047 km^3 respectively) at monthly rates of the order of -0.025 km^{3}per month. For the same time periods, Bertin et al. (2015)

estimated an erupted lava volume of 0.18 km^3 for interferogram 2011-07/2011-10 and 0.13 km^3 for interferogram 2011-10/2011-12. Using equation 1 with the same magma compressibility as for the previous exercises, gives values of K_r of 1.57 x 10^{-10} Pa^{-1}and 1.19 x 10^{-10} Pa^{-1}. These values are similar to the one computed for the first co-eruptive interferogram based on the two Mogi sources and therefore one order of magnitude higher than the rock compressibility estimated by the seismic velocity model. The consistent difference between values of K_r derived from the Mogi source models for the first and last interferograms and the one estimated from the seismic velocity model is likely indicative of a systematic overestimation of volume changes at depths related to the complex rheologic structure of PCCVC not reflected by the simple isotropic linear elastic solid assumed by the Mogi approximation. As a corollary, this consistency also suggests that a missing erupted volume is likely needed to explain the large volume change at depth modelled for the second co-eruptive interferogram.

Since the effusion rates steadily decreased from mid-July onwards (Bertin et al.,2015), it can be suggested that the small surface deformation afterwards is not solely due to the further evacuation of magma from a deep reservoir but also related to the relaxation of the system after the eruption. This post-eruptive process could include a number of phenomena acting simultaneously (viscous and poroelastic relaxation of the upper crust, e.g. Plattner et al. (2013), Segall (2010), Froger et al. (2016), creeping at faults, e.g. Hill & Prejean (2007), densification of erupted lava flow and consequent increase of vertical loading, e.g. Lu et al. (2005), Odbert et al. (2015) etc.) that cannot be simulated by the simple elastic half-space model assumed by the point Mogi source.

3.10 Conclusions

We can conclude that a structural control on the 2011 PCCVC eruption, although being very likely from geological, volcanological and petrological perspectives, is only indirectly shown by data and results presented and discussed here. Particularly, InSAR-observed surface deformation associated with the first explosive phase of the eruption can be better explained by a model considering two point Mogi sources aligned with the Cordón Caulle graben than a combined model of a closing and slipping Okada dike in the NW with a small Mogi point in the SE. However, the model including the slipping dike requires a much smaller volume change at depth, which translates into a smaller implied value of rock

compressibility that is more consistent with the value derived from the local seismic velocity model generated during seismicity relocation. Thus, it seems very likely that a more complex source configuration at the intersection of Cordón Caulle graben with Cordillera Nevada could reconcile these observations. At least for the first, explosive phase of the eruption, we envisage a deflating point-like source at depth from which a smaller amount of magma and gases is extracted (compared with the estimated amount of the two point sources model) that is connected with a dike propagating along the northern wall of Cordón Caulle graben toward its intersection with the LOFZ where the vent was finally opened. Seismicity accompanying this first phase was recorded by few local stations and it does not show a clear migration of a rupturing front as observed for other well-studied dike propagating events. However, the spatiotemporal evolution of seismicity shows that quakes were concentrated below Cordillera Nevada until days before the eruption and then they show an expansion toward the SE and simultaneous shallowing. This is at least consistent with the idea of a pulse of magma and gases advancing from the main reservoir in the NW along the graben, opening the walls of the graben to create the vent at the intersection with the main LOFZ branch and finally stimulating the onset of the explosive phase. Since the seismic moment computed from the left-lateral motion of the dike-like structure is an order of magnitude higher than the cumulated moment released by quakes recorded during the same period of time, we suggest that most of the slip that could have accompanied the dike propagation was aseismic. After three days of volcanic paroxysm, the InSAR-observed surface deformation recorded during the first weeks of the effusive phase is well modelled by an isolated deflating Mogi source near the source of the first phase, and an Okada dike-like model can be discarded. This is expected because once the structural channel between magmatic reservoir and eruptive vent is created, magma and gases are just conducted along this channel with no need for further motion of the structure. However, the concentration of seismicity along the SE part of Cordón Caulle graben and the western branch of the LOFZ, in conjunction with large vertical and SSE residual motion (with respect to the InSAR-derived source model) observed at the continuous GPS station PJRT located near the main branch of the LOFZ, both suggest that the structural framework over which PCCVC is installed was partially activated also during the effusive phase.

This eruption is the first large acidic, explosive eruption that is relatively well monitored by local seismic and geodetic networks. These observations indirectly suggest that such an eruption could be at least partially controlled by the activation of structures forming

the plumbing system of a long-lived magmatic reservoir, a control which was also inferred for the hybrid explosive-effusive rhyodacitic eruption of Chaitén volcano in 2008 (Wicks et al., 2011; Piña-Gauthier et al., 2013). A different modelling approach based on finite element methods could perhaps help in the future to test more complex rheology and source scenarios combining deformation and seismicity during the 2011 Cordón Caulle eruption that could more clearly show the structural control on this kind of largely dangerous eruptions.

3.11 Acknowledgements

CAPÍTULO IV: Structural control on silicic magma ascent and evacuation evidenced by seismicity recorded during the 2011 eruption of Cordon Caulle (Southern Andes)

Aceptado con corecciones en Journal of Volcanology and Geothermal Research

Daniel Basualto[1,2,3,4], Jonathan A. Lazo Gil[5], Luis Franco[2,3,4], Carlos Cardona[2,3,4], Juan J. San Martín[5], Fernando Gil[4], Francisco Garcia[2,3], Marcela Calabi-Floody[6], Andrés Tassara[2]*

[1]Universidad Católica de Temuco, Departamento de Geología y Obras Civiles, Facultad de Ingeniería, Rudecindo Ortega #02950, Temuco, Chile.

[2]Universidad de Concepción – Departamento Ciencias de la Tierra, Víctor Lamas #1290, Concepción, Chile.

[3]Universidad de Concepción – Programa de Doctorado en Ciencias Geológicas, Víctor Lamas #1290, Concepción, Chile.

[4]Servicio Nacional de Geología y Minería "SERNAGEOMIN"-Red Nacional de Vigilancia Volcánica "RNVV"- Observatorio Volcanológico de los Andes del Sur "OVDAS"; Rudecindo Ortega # 03850,Temuco, Chile.

[5]Universidad de La Frontera, Departamento de Ciencias Físicas, , Casilla 54-D, Temuco, Chile.

[6] Universidad de La Frontera , Nano-biotechnology Laboratory, Center of Plant, Soil Interaction and Natural Resources Biotechnology, Scientific and Biotechnological Bioresource Nucleus, BIOREN-UFRO, Temuco, Chile.

*Corresponding author: Andrés Tassara, andrestassara@udec.cl

4.1 Resumen

Las erupciones explosivas silíceas son uno de los fenómenos naturales más peligrosos, pero se sabe poco sobre los procesos que acompañan este tipo de erupciones, ya que son poco comunes. Presentamos la primera caracterización sistemática que se produce antes, durante y después de una gran erupción silícea, analizando los datos registrados en el Complejo Volcánico Puyehue-Cordón Caulle (PCCVC) durante la erupción riolítica VEI=4 en junio 4 de 2011. Estos datos fueron registrados por la red sísmica del Observatorio Volcanológico de los Andes del Sur (OVDAS) del Servicio Nacional de Geología y Minería (SERNAGEOMIN), red que se mejoró localmente después del gran terremoto Mw:8.8 de febrero 27/2010, región del Maule. Los resultados preliminares procesados por OVDAS para monitorear la crisis eruptiva fueron complementados con el análisis de inversiones sísmicas, mecanismos focales, series de tiempo del valor b y la relocalización de hipocentros generados gracias a un nuevo modelo local de velocidad 1D, ya que con ello se logró describir la evolución espacio-temporal de la sismicidad durante la crisis volcánica. Considerando los datos preliminares analizados y los resultados publicados años antes (en su mayoría estudios de deformación InSAR), se logró identificar varias fases antes, durante y después de la erupción registrada en 2011. La Fase Inicial de precursores (diciembre de 2010 - abril de 2011) fue iniciada con eventos relativamente energéticos de baja frecuencia (LP) e híbridos (HB) que fueron seguidos por la ocurrencia de eventos volcanotectónicos (VT) ubicados a 5-10 km por debajo de Cordillera Nevada (en el extremo NW del PCCVC). Esta ubicación coincide aproximadamente con las fuentes de inflación reportadas años antes de la erupción. Un gran evento HB (*Ml*4.5) marcó la entrada en una segunda fase de mayor inestabilidad (Enhanced, abril-mayo), caracterizada por un incremento en el número diario de eventos VT, HB. De igual forma, sus magnitudes aumentaron con el tiempo a medida que los hipocentros migraron a lo largo del graben del Cordón Caulle hacia el Este como hacia la superficie. La semana anterior a la erupción (Fase Final de la actividad precursora) se caracterizó por un número creciente de eventos poco profundos con una combinación de eventos VT, LP y HB, predominando este último tipo de evento sísmico. El número de eventos, sus energías y sus magnitudes aumentaron gradualmente con el tiempo, mientras que el valor b disminuyó considerablemente días antes de la erupción, lo que sugiere una presurización del sistema volcánico. Los mecanismos focales de los grandes eventos de HB de las fases precursoras están dominados por una expansión volumétrica, consistente con la movilización esperada de fluidos y magmas desde la cámara principal (más profunda, con altas presiones de confinamiento) hacia el cono final, distante 11 km. Una vez que la erupción comenzó, el

conducto se abrió violentamente la tarde del 4 de junio, dando origen la Fase Explosiva, la que duró 10 días y se caracterizó por el hundimiento de la superficie observado por InSAR, disminuyendo la cantidad y la magnitud de los eventos VT y HB, aumentando los valores de b (interpretados como una relajación del sistema), registrando además un tremor definido como espasmódico, cuya amplitud disminuyó con el tiempo atribuido a la disminución de la altura de la columna piroclástica (de 14 a 2-3 km). El 15 de junio, una reducción notable de la columna piroclástica fue seguida por el inicio de la Fase Efusiva, la que se extendió hasta el 6 de agosto. La Fase Efusiva estuvo marcada por una disminución adicional en la tasa de sismicidad, aunque con magnitudes algo mayores que la fase anterior, y la aparición de un temblor energético cuasi-armónico, cuya amplitud está directamente relacionada con las tasas de descarga de lava riolítica desde su cono. Una Fase de Declinación (agosto-septiembre) con bajos niveles de sismicidad y emisión de lava, es seguida finalmente por una Fase de Resurgimiento (octubre 2011 - enero 2012) cuando un número creciente de eventos de LP fueron coetáneos con un incremento en la emisión de lava y ceniza desde el cono de 2011. Los mecanismos focales de eventos VT que se producen principalmente durante la fase efusiva muestran una combinación de fuentes con una prevalencia de mecanismos normales alineados con el muro sur del graben y soluciones transcurrentes pertenecientes a un grupo de sismos alineado con el Sistema de Fallas Liquiñe-Ofqui (LOFS). Nuestros resultados muestran, con detalles sin precedentes, la evolución de una gran erupción silícea y analiza una serie de procesos subyacentes, con énfasis en el posible papel que podrían tener las estructuras del basamento para permitir la movilización de magma y fluidos a alta presión antes de la erupción, seguidos por una subsidencia durante la evacuación de magma y gases volcánicos.

4.2 Abstract

High-silica explosive eruptions are one of the most dangerous natural phenomena, yet little is know about processes accompanying this type of eruptions because they are relatively uncommon. We present the first systematic characterization of seismicity occurring before, during and after a large high-silica eruption, analyzing data recorded in the vicinity of Puyehue-CordónCaulle Volcanic Complex (PCCVC) during its VEI=4 2011 rhyolitic eruption. These data were recorded by the seismic network of ObservatorioVolcanológico de los Andes del Sur (OVDAS, part of the Chilean Geological Survey SERNAGEOMIN), which was locally improved in the aftermath of the great Mw8.8 2010 Maule megathrust earthquake. Results of a preliminary data processing, developed by OVDAS to monitor unrest and

eruption, were complemented here with the computation offocal mechanism, time-series of the b-value, and the relocation of hypocentersinto a local 1D velocity model. Considering the preliminary data and published results (mostly of InSAR-based studies of surface deformation), we first defined several phases before and after the onset of the eruption (June 4th 2011). Then, we describe the space-time evolution of seismicity. Theinitial unrest phase (December 2010 – April 2011) wasinitiated by relatively energetic low-frequency (LP) and hybrid (HB) events that are followed by the occurrence of volcano-tectonic (VT) events located 5-10 km below Cordillera Nevada (at the NW-extreme of the PCCVC). This location roughly coincidences with sources of surface inflation years to months before the eruption. A large (Ml4.5) HB event marked the entrance in a phase of enhanced unrest (April-May) when the daily number of VT and mostly HB events and their magnitudes increased with time as the hypocenters migrated to shallower depths and south-westwards along the Cordon Caulle graben. The week before the eruption (final unrest phase) was characterized by an increasing number of shallow events with a mix of VT, LP, and mainly HB events. The number of events, their energy and magnitudes gradually increased with time, whereas the b-value strongly decreased days before the eruption suggesting a pressurization of the system. Focal mechanisms of large HB events of the unrest phase are dominated by a volumetric expansion, consistent with the expected mobilization of magma and fluids from the deep reservoir toward the final vent at high confining pressures. Once the vent was violently open the afternoon of June 4th, an explosive phase that lasted 10 days was characterized by meter-scale surface subsidence observed by InSAR, decreasing amount and magnitude of VT and HB events, increasing b-values (interpreted as a relaxation of the system) and a spasmodic seismic tremor which amplitude decreased with time following the height of the pyroclastic column (from 14 to 2-3 km). On June 15th, a notable reduction of the pyroclastic column was followed by the initiation of the effusive phase that characterizes the eruption until August 6th. This phase is marked by a further decrease in seismicity rate although with somehow larger magnitudes than the previous phase, and the occurrence of an energetic quasi-harmonic tremor which amplitude is directly related to discharge rates of rhyolitic lava from the vent. A declining phase (August-Spetember) with low levels of seismicity and lava effusion,is followed by a resurging phase (October 2011 – January 2012) when a rising number of LP events were coeval with a renewed emission of lava and ash from the vent.Focal mechanisms of relatively large VT events occurring mostly during the effusive phase shows a mix of sources with a prevalence of normal mechanisms aligned with the southern branch of the graben and strike-slip for those belonging to sub-clusters aligned with the Liquiñe-Ofqui Fault Sistem (LOFS)

at the eastern border of PCCVC. Our results show, with unprecedented detail, the evolution of a large high-silica eruption and illuminate a number of underlying processes, with emphasis on the possible role that basement structures could have on allowing the mobilization of magma and fluids at high pressure before the eruption and further relaxation of stresses during the evacuation of magma and gases.

4.3 Introduction

Silicic volcanic eruptions are one of the most dangerous natural hazards , commonly associated with the violent explosive evacuation of volatile-rich magma. Explosive high-silica eruptions are relatively infrequent but are associated with some of the largest natural disasters in human history (e.g. Vesuvius 79, Ilopango 429, Unzen 1792, Krakatau 1883, Mt Pelee 1902, Pinatubo 1991). Only a handful of these eruptions however, have been instrumentally monitored (e.g. Usu 1978-1979, Yokohama et al., 1981, Usu 2000, Matsubara et al., 2004; Pinatubo 1991, Wolfe and Hoblitt 1996;Unzen 1991-1995, Umakoshi et al., 2008; Mt St. Helens 1980-1986 and 2004-2008, Dzurizin et al., 2005; Chaiten 2008, Wicks et al., 2011). This gap hampers our ability to understand possible near field precursory signals that could be useful for short-term hazard assessment and mitigation of its potentially catastrophic effects. Remote satellite-based observations and far-field recorded seismicity could help to partially fill this gap, as for the case of the rhyolitic eruption of Chaitén 2008 (Wicks et al., 2010; Piña et al., 2011). But direct records of instruments installed in the neighborhood of erupting silicic volcanoes, are almost lacking.

We present the first systematic characterization of seismicity occurring before, during and after a large high-silica eruption, analyzing data recorded in the vicinity of Puyehue Cordón Caulle Volcanic Complex (PCCVC) during its VEI=4 2011 rhyolitic eruption. These data were registered by a seismic network installed by the Observatorio Volcanológico de los Andes del Sur (OVDAS), belonging to the Chilean Geological Survey (SERNAGEOMIN). Before 2010, this network was composed by few isolated stations located at relative large distance (>30 km) from PCCVC. The number of near-field instruments (distances < 10 km) was augmented in the aftermath of the great Mw:8.8 Maule 2010 megathrust earthquake (which southern limit is located 300 km northward from PCCVC). This was motivated by the expectation of a possible post-seismic unrest of PCCVC, as could be suspected when

considering that its last eruption occurred 38 hours after the giant *Mw*:9.5 Valdivia 1960 earthquake (e.g. Lara et al., 2006; Amelung and Walter., 2009).

The possible earthquake triggering of the 1960 eruption was likely facilitated by the primary structural control exerted by regional basement faults on the magmatic plumbing system at PCCVC (Lara et al., 2004; Sepulveda et al., 2005; Singer et al., 2008). Indeed, the complex is composed by three main edifices located along an inherited (Paleozoic age) NW-oriented structure (Fig. 4.1): Cordillera Nevada Caldera at the NW extreme, Puyehue stratovolcano at the SE extreme, and Cordón Caulle graben connecting both extremes along a tectonic depression bounded by NW-SE fissures. Puyehue Volcano is itself located at the intersection of this basement structure with a major 1000 km long NNE-oriented structural system known as the Liquiñe-Ofqui Fault Zone (LOFZ). This system accommodates the dextral trench-parallel component of oblique convergence between Nazca and Southamerica plates and is genetically linked to the Southern Volcanic Zone (SVZ) of the Andes (Cembrano and Lara, 2009).This tectonic setting means that PCCVC is dominated by transpressional stresses during the interseismic phase of megathrust seismic cycle, which characterize the long-term crustal deformation. This tectonic setting explains the Late Pleistocene to Holocene evolution of the complex from a bulk basaltic composition to dacitic-rhyolitic. This magmas are the result of prevailing closed conditions of a long-lived magma reservoir, where magma can differentiate forming a high-silica melt on top of a crystal-rich mush zone (Lara et al., 2006b; Singer et al., 2008; Cembrano and Lara, 2009). In addition to this presumed structural control on long-term evolution (Lara et al., 2006a), the last three eruptions (1921/22, 1960 and 2011) evacuated almost the same rhyodacitic magma (67-74% SiO_2; Castro et al., 2013; Jay et al., 2014, Alloway et al., 2015) and where all connected to the structural borders of Cordón Caulle graben (Fig. 4.1). In this study, we combine relevant information published by previous authors and general features of seismic activity, as reported by the preliminary data analysis used by OVDAS. With this preliminary analysis, OVDAS could monitor the pre-eruptive unrest and declare changes in the level of volcanic alerts before and after the eruption onset. This is followed by results of the advanced analysis of seismicity and their sources, as presented into the framework of the previously defined chronology of the eruption.

Into this framework, the analysis of the 2011 eruption from both a petrological perspective (Castro et al., 2013, Alloway et al., 2015) and modeling of geodetic data (Jay et al., 2014; Wendt et al., 2017), suggest that it was coeval with activity of faults serving as

feeder dykes connecting a 5-8 km depth magmatic reservoir to the eruption vent. The detailed seismicity-based characterization of the eruption presented here, allows us to independently complement these previous findings, supporting the structural control on eruptive behavior and contributing with unprecedented information about the evolution of seismic activity during a high-silica eruption.

4.4 Data and methods.

We will first present details of the seismic network and methods, which is separated into a preliminary data processing step done by OVDAS during the crisis and an advanced analysis of the recorded seismic data. The later includes the relocation of hypocenters via computation of a local seismic velocity model. The estimation of focal mechanisms were calculated by first arrivals and waveform inversions, and computation were obtained though the time-series of the *b-value* that characterizes the frequency-magnitude relation of seismicity. We then describe the chronology of the 2011 eruption, including the definition of a number of phases from years before the eruption, to several months after its onset.
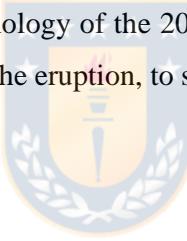
4.4.1 Seismological network.

The seismic network considered in this study (orange triangles, Fig. 4.1), involves seven stations installed before the eruption, six of them corresponding to Reftek151-30A, 0.03-50 *Hz* broadband seismic sensors connected to a Reftek 130B digitizers, and one station (PHU, the closest station to the eruptive vent) being instrumented with a Guralp 6TD 30 second seismic sensor and a 6TD digitizer. All the stations were connected by telemetry and internet to the OVDAS observatory located in the city of Temuco (aprox. 200 km northward) where a continuous flow of data was established allowing the monitoring of unrest and eruption in near real time. Four of these stations are located in the far field (35 to 80 km distance from PCCVC; Fig. 4.1) and form part of the regional surveillance network of OVDAS as consolidated in 2010. Up to 3 days after the eruption onset, other three stations (green triangles, Fig. 4.1; FUT, TAY and LIC; Reftek151-30A, 0.03-50 *Hz* connected to a Reftek 130B digitizers) were installed in the southern and western flank of PCCVC to monitor in detail the advance of the eruptive process. The sampling rate of seismic data was 100 samples per second. Finally, the installation of two surveillance optical cameras 5 days

after eruption onset, facilitated the observation of the post-eruptive phase, recording important explosions associated with the paroxysmal phase of the eruption and the subsequent extrusion of lava.
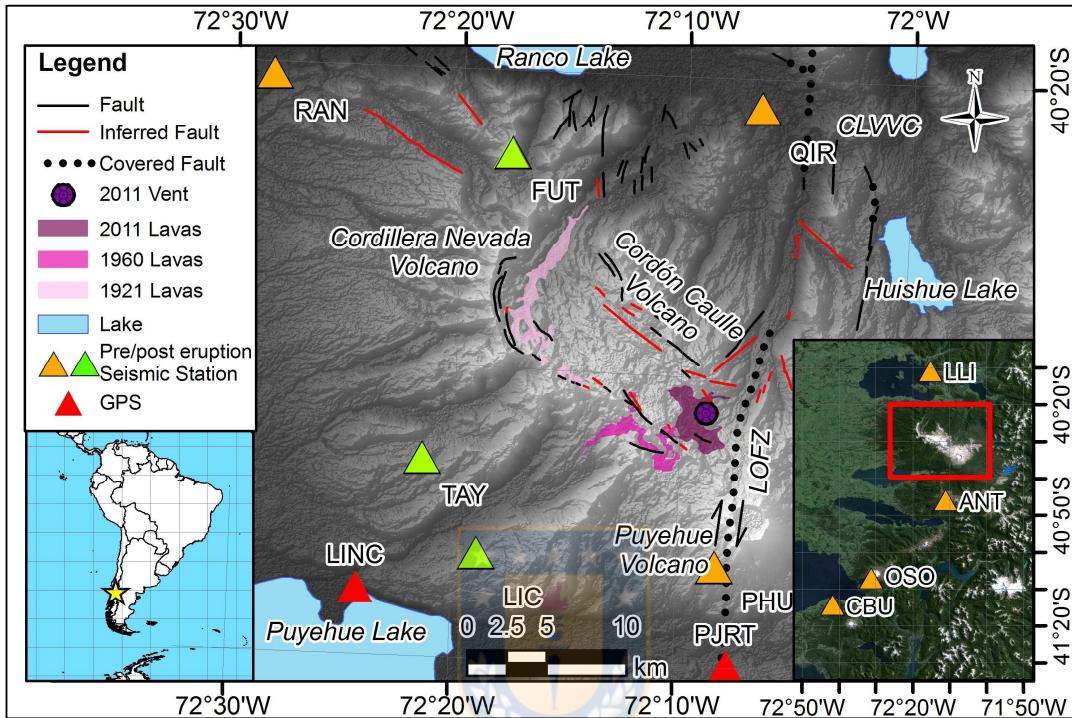
Figure 4.1. Location of Puyehue-Cordon Caulle Volcanic Complex (PCCVC) in the Southern Volcanic Zone (SVZ) of the Andes of southern Chile. On top of the topographic map we mark main geological structures (noting the Liquiñe-Ofqui Fault Zone LOFZ), lava flows generated by the 1921, 1960 and 2010 eruptions, the 2011 open vent and location of seismic stations (three orange triangle for pre-eruption and three green triangle for post-eruption location). The inset at the right bottom corner shows location of far-field seismic stations (four orange triangles). The red triangles in the bottom show two GPS cited in Wendt et al. (2017). Fuente: elaboración propia.

4.4.2. Preliminary data processing

A preliminary processing of the data recorded continuously by the routinely monitoring of OVDAS were used to follow the unrest and eruptive process. This considers the manual recognition of individual seismic events from the continuous seismic signal and extraction of basic information for each of them; as amplitude, duration and picking of wave phases. This information allowed the constuction of the computation classification scheme of Lahr et al. (1994) and Chouet (2003), which is based on the waveform appearance on the seismic records, wave morphologies and length. This establishes four main kinds of volcanic

signals. First: volcano-tectonic (VT) events, clear arrivals of the P and S body waves, that are related to brittle fracturing of rocks. Second: long period (LP) and very long period (VLP) events, with a body wave arrivals and a concentration of energy at low frequencies (LP<5 Hz and VLP<0.5 Hz) that suggest a genesis related to fluids movement or pressures changes of volcanic conduits. Third: hybrid (HB) events with a combination of features of VT and LP/VLP signals; and fourth: tremors (TR), which origin are similar to LP events, but with a sustained excitation through time that can last by hours to days. Finally, using the Local Magnitudes (*Ml*) proposed by Hutton & Boore, (1987), seismic energies described by Gutenberg & Richter, (1956) and the preliminary location of the hypocenters were calculated by HYPO 71. The preliminary data processing generated a database consisting on a total number of 32,850 earthquakes recorded between December 2010 and December 2011, from which 7,100 were classified as VT; 12,500 as LP and VLP; 7,150 as HB and 6,100 as TR (Fig. 4.2A). We also used wave polarization (Matsumura, 1982) to corroborate the existence of body waves in representative seismic traces (>10 μm) HB, LP, VLP, and Tremor (TR) events. In the last case, the polarization helped to estimate locations (azimuth) for case of TR seismic activity (Bertin et al., 2015). In order to quantify the size of TR events (spasmodic and quiasi-armonic; Supplementary Material Fig. S5-A y S5-B), the reduced displacement (D_R) was used (Aki, 1981; Fig. 4.2C).
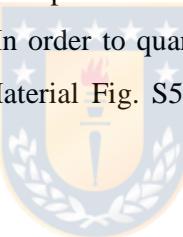
4.4.3. Advanced post-processing of the seismic data

A second, post-processing level was implemented in this work with the aim to refine the location and characterization of seismicity, including the following procedures:

4.4.3.1. 1D seismic velocity model and hypocenter relocation

We performed a relocation process of the recorded events using the Join Hypocenter Determination (JHD) algorithm (Crosson, 1976; Ellsworth, 1977; Thurber,1983). For this, the local one-dimensional (1D) crustal velocity model was refined from the regional model of Bohm et al. (2002) using VELEST (Kisslinget al., 1994) and considering only 425 high quality events (8 or more phases; horizontal errors <0.5 km, vertical errors<1 km; RMS solutions <0.15; gap <180°) from the 1750 earthquakes preliminary located using HYPO-71. The reference level of the 1D model was established at 1.5 km above sea level. According to the methodology proposed by Kissling et al. (1994), we proceeded to verify the results, fixing the 1D velocity model and time delays to each station, giving only degrees of freedom at 100 hypocenters, restoring the majority of the best locations.

4.4.3.2. Waveform Inversion of focal mechanisms

Focal mechanisms of relative large events (*Ml*>3.0) were computed using SEISAN [Earthquake Analysis Software Version 10.0; Havskov and Ottemoller (1999)] and considering first motion for events with 7 or more impulsive polarities recorded by the network. In order to improve the solutions, the nodal planes were selected using the S/P ratio amplitudes (Hardebeck and Shearer, 2003). For some particular cases of large VT, VLP and HB events we also computed the whole seismic moment tensor using waveform inversions with ISOLA (Sokos and Zahradnik, 2008). To eliminate noise signal, point-source deconvolution iterations were filtered to frequencies<0.25 *Hz*. The calculation of the Green Functions associated to the total wave field generated by the elastic behavior of the crust was developed following the methodology proposed by Bouchon (1981). The moment tensor is calculated using the least squares method. The time of origin and the spatial position of the point source (centroid) were searched around the relocated hypocenter. After introducing the instrumental response of the stations and the local velocity model, we proceeded to integrate the velocity signal.

4.4.3.3. Temporal variation of *b-value*

We investigate the temporal evolution of seismicity by means of the frequency-magnitude relationship as parameterized by the *b-value*, which is the slope on the Gutenberg and Richter (1944) earthquake-size distribution. We applied the method described in detail by Tassara et al. (2016), which is based on the maximum likelihood method (Aki, 1965; Hamilton, 1967). With this method, the *b-value* of a group of seismic events can be estimated as:

$$b = \frac{1}{\ln 10 \, (M_{mean} - M_c)}$$

where M_{mean} is the average magnitude of the sampled events and Mc the magnitude of completeness above which earthquakes are reliably recorded by the seismic network. We worked with a group of 1.750 events (VT and HB) with reliable estimated magnitudes. The magnitude of completeness of this sample is 1.6. We used correlative and overlapping time windows defined by the occurrence of 125 events with an overlap between them of 75%. For each window we compute one *b-value* and its error (as estimated using Aki, 1965). For the interpretation of the resulting time-series we considered that low/high *b-value*s are

characteristic of tectonic settings dominated by reverse/normal faulting (Scholz, 2015). Due to the large stress necessary to activate a reverse fault compared to a normal fault, this observation has led to the use of the *b-value* as a stress-meter that points to high/low stress at faults showing low/high *b-value* (Schoerlemer et al., 2005).

4.5. Chronology of 2011 Eruption

In order to establish a temporal framework to describe our results, we consider general information about the seismic activity reported by OVDAS mostly based on the preliminary processing of data recorded by the seismic network, and complemented this with a review of existing literature on time evolution of PCCVC between 2007 and the end of 2011. This is mostly based on observed changes of eruptive style after eruption onset and published analyses of InSAR and GPS data. Considering this information, we recognized and described the following temporal phases (Fig. 4.2).

4.5.1. Pre-unrest (2007-Dic 2010).
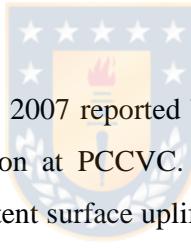
InSAR images obtained before 2007 reported by Fournier et al. (2010) and Jay et al. (2014) indicate no ground deformation at PCCVC. Interferograms from January 2007 to December 2009 however, show persistent surface uplift at rates of 20 cm/yr and these sources were modeled as lying 3-8 km below Cordillera Nevada and the SW flank of Cordón Caulle graben (Fournier et al., 2010). This inflation episode was accompanied by clusters of moderate magnitude (*Ml*: 1.5-4.0) VT quakes identified by the regional OVDAS network and located 1-10 km below Cordillera Nevada. After the *Mw*:8.8 Maule earthquake of 27 February 2010, Jay et al. (2014) identified a shallow inflation (1.7 km depth) below Cordillera Nevada, likely associated with the activation of the hydrothermal system.
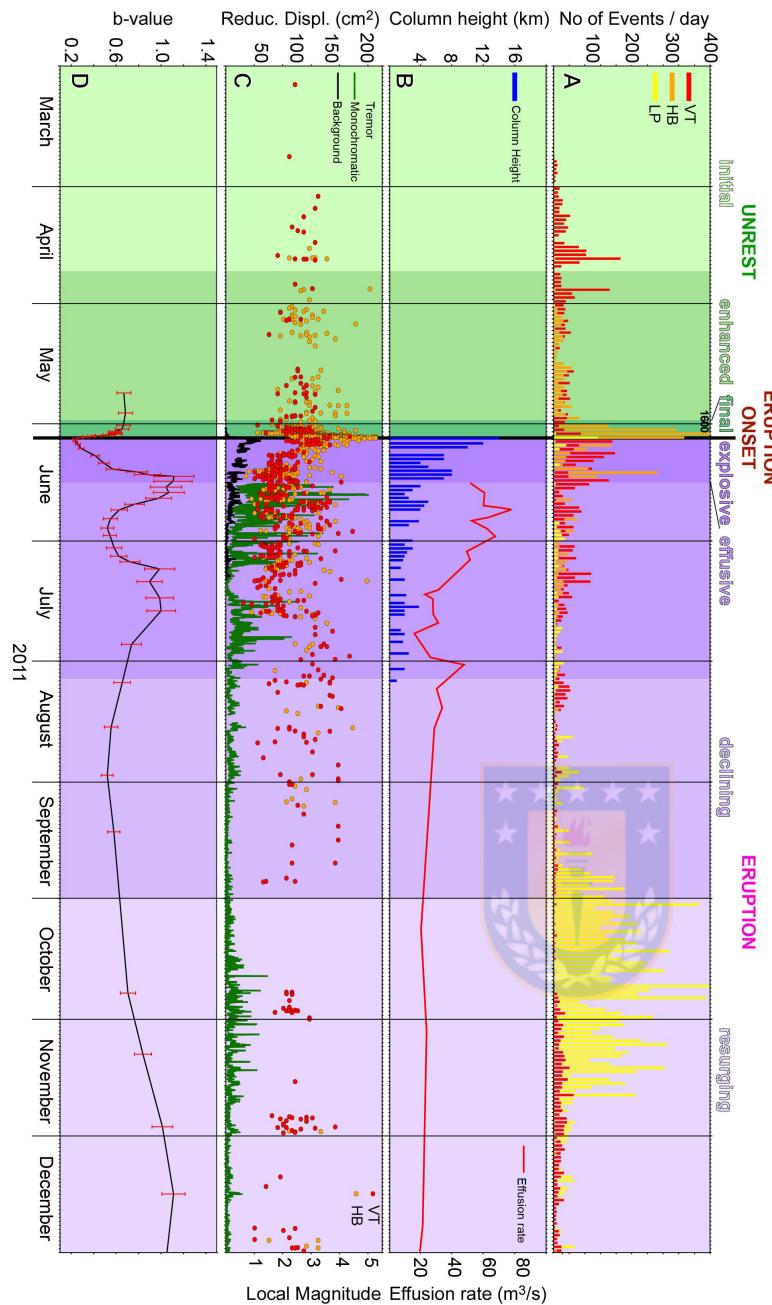
Figure 4.2. Time series of relevant parameters before (March) and after (December) the 2011 PCCVC eruption (June 4th).A: Daily count of VT (red), HB (orange) and LP (yellow) seismic events. B: Height of the pyroclastic column (blue) and effusion rate (red, after Bertin et al. (2015)). C: Local magnitude of VT (red) and HB (orange) events, amplitude of reduced displacement Dr of the background tremor (black) accompanying the explosive phase and the monochromatic tremor (green) dominating the effusive phase. D: *b-value* (grey line) with error bars (red). Fuente: elaboración propia.

4.5.2. Unrest (December 2010 – June 4 2011)

4.5.2.1. Initial (December 2010 – April 21 2011)

The regional network of OVDAS recognized first signs of unrest by the end of 2010, observing a sporadic record of low frequency events classified as VLP and HB. The subsequent installation of the seismic monitoring station PHU at the southern flank of Puyehue volcano in February 2011, and stations POC and RAN in the northern sector of PCCVC over the following two months, allowed capturing details of this seismicity through time. During the first half of March, some VT events per day were recorded with Ml<2-3 and were located 4-10 km depth below Cordillera Nevada (Fig. 4.4A). By the end of this month the number of VT events increased. A tendency maintained during the first half of April when pulses of this kind of quakes (mixed with some LP and HB events) lasting several days and reaching a register up to 180 events/day with magnitudes of Ml:4. After a cluster of seismicity on April 18, a period of relative seismic calm culminates this phase.
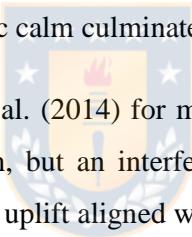
An InSAR image presented by Jay et al. (2014) for mid October 2010 to mid January 2011 shows no sign of surface deformation, but an interferogram between 9 March and 8 May suggest up to 5 cm line-of-sight (LOS) uplift aligned with the north-western extend of Cordón Caulle graben. This signal however, is considered as a tropospheric effect by Wendt et al. (2017).

4.5.2.2.Enhanced (April 22 - May 30)

A reactivation of seismicity during the last week of April was crowned the 27th with a very energetic event (Ml:4.5) classified as HB, which indicated signs of magma and/or fluid migration (Supplementary Figure S1). This event was followed by a cluster of decreasing number of mixed VT and HB seismicity. During the first half of May, the number of VT events kept constant in ca. 30-40 events/day with magnitudes up to Ml:3.5. Whereas HB events start to be more notable and reached larger magnitude (Ml:3.5-4). Preliminary locations of these epicenters suggested a spatial migration from deep (10 to 5 km depth) sources below Cordillera Nevada, to shallower depths (<5 km) toward the SE along Cordón Caulle graben. After a relative seismic quiescence at the mid of May, the second half of this month was characterized by a relatively constant rate of seismicity of mixed VT and HB

origin on the order of 35-45 events of each type per day, but maximum magnitudes were gradually increasing and locations were concentrating toward the central and eastern side of the graben with shallower depths (Fig. 4.4A).

4.5.2.3. Final Unrest (31 May – 4 June)

The week before the eruption was characterized by an increasing number of shallow events with a blend of seismic sources, showing a mix of VT, LP, and mainly HB events. The number of events, their energy and magnitudes gradually increased with time. On June 2th, OVDAS changed the volcanic alert to yellow (level 3). In the following days seismicity rate and magnitudes increased recording ca. 1600 HB events, the day before the eruption (Fig. 4.2), and more than 200 events per hour some hours before the eruption (Supplementary Figure S2, S3 and S4), with at least 25% of them presenting Ml:3.0-4.9. Considering this intense seismic activity, OVDAS decided to warn a red alert, activating the evacuation of the population within a radius of 25 km from the volcano on the morning of June 4th. In this period, the network started to record seismic activity outside the Cordón Caulle graben, suggesting the activation of a NNE-SSW branch of LOFZ (Fig. 4.4B).

4.5.3. Eruption (4 June 2011 – January 2012)

4.5.4. Onset (4 June,14:45 hours local time (18:45 GMT))

Culminating the intense seismic activity recorded at the end of the Final Unrest Phase, a Plinian VEI=4 explosive eruption took place, opening a new vent near the intersection of the northern branch of Cordón Caulle graben with a western trace of LOFZ. A sustained and vigorous eruptive column was fed from the vent at rates near 10^7 kg/s (Pistolesi et al., 2015) and rose to an altitude of 10-12 km in less than one hour.

4.5.5. Explosive (June 4 – June 14)

The paroxysmal starting phase lasted 2-3 days, with a pyroclastic column that reached up to 14 km height, and at least five episodes of partial column collapse that generated pyroclastic density currents mainly heading north (Pistolesi et al., 2015). Over the following week, column height oscillated in response to frequent variable-sized explosions and steadily reduced to 4-8 km height (Fig. 4.2B).

A SAR interferogram formed by scenes acquired at 8 May and 7 June 2011, captured the surface deformation produced by the first 3 days of the eruption (Jay et al., 2014; Wendt et al., 2017). This InSAR image is characterized by two lobes of large subsidence joined by an area elongated along Cordón Caulle graben. One lobe is collocated with the rim of Cordillera Nevada and shows up to 1.2 m of LOS subsidence, whereas the second less prominent and less coherent lobe lies southward of the new vent (Wendt et al, 2017). The source of deformation has been modeled by two deflating point sources at depths of 3.5-6 km, with volume changes in the order of -0.02 to -0.1 km^3 (Jay et al., 2014, Wendt et al., 2017). Wendt et al. (2017) demonstrated that the observed deformation signal could also be modeled by a closing NW-oriented southward-dipping dike, with a significant component of left-lateral strike slip movement, connecting the rim of Cordillera Nevada with the active erupting vent (Fig. 4.4C).

During the paroxysm, preliminary located events covered the entire graben area and the western flank of Puyehue Volcano, with an important cluster located southward of the active vent. After the paroxysm, a sharp decrease of HB events and an increase of VTs was recorded both with decreasing magnitudes with time. This seismicity was accompanied with a spasmodic tremor (Supplementary Material Fig. S5-A), which became the dominant component of the seismic signal since 6 June (Bertin et al., 2015). The multi-frequency character (0.4-4Hz) and constant oscillations in the amplitude of the tremor (as measured by the reduced displacement, Fig. 4.2C), evidenced a possible combination of sources and explosions, ash and gas output, and several pyroclastic flows. Digital elevation models constructed by Castro et al. (2016) from radar satellite images, suggest that a laccolithic intrusion started to develop at 8 June below the eruptive vent in response to conduit constriction (8-fold decrease in vent diameter), caused by the accumulation of blasts expelled by Vulcanian explosions.

On 12-13 June, pulsating pyroclastic jets were accompanied by an oscillating tremor signal, increased number of HB events and vigorous explosions that cast large ballistic bombs to distances of up to 2.5 km from the vent (Castro et al., 2013). By the end of this phase, the rate of seismicity decreased, the amplitude of the spasmodic tremor became minimal and eruptive column height was lowered to less than 4-3 km.

4.5.6.Effusive (15 June– 6 August)

Since 15 June, the entire seismic network began to record energetic low-frequency pulses constitutive of a quasi-harmonic tremor (Bertin et al., 2015). The reduced displacement of this signal was 10-15 times larger than the spasmodic tremor of the explosive phase (Fig. 4.2C; Supplementary Material Fig. S5-A), and indicated a significant change in the behavior of the eruption. This was interpreted by OVDAS as the onset of an effusive phase. A lava flow was actually confirmed on 17 June by satellite images and later on 20 June by an overflight (Bertin et al., 2015). As summarized by Bertin et al. (2015), tremor particle motions showed a P-wave nature with incidence angles close to sub-horizontal, pointing out to a shallow source and with virtually no changes of the dominant frequency of the tremor during the effusive phase. These tremor oscillation features, suggest the fast movement of magmas. A significant temporal correlation between reduced displacement (D_R) of the tremor and discharge rates of lava flow estimated by satellite images (Fig. 4.2B), confirm this causal relation (Bertin et al., 2015). Discharge rates 8 days after the start of the effusive phase were as high as 70 m^3/s, whereas the average eruption rate during the first 20 days was 50 m^3/s (Bertin et al., 2015). The initiation of the effusive phase was accompanied by a decrease in the seismicity rate of VT and HB events, although the magnitude of these events were somehow higher than during the end of the explosive phase. The quiasi-armonic tremor represented the beginning of magma supply (Fig. 4.2B). During the first half of July the daily number of seismic events kept relatively constant showing a prevalence of VT with respect to HB and LP, whereas the effusion rate gradually decreased together with the reduced displacement of the tremor. The last 2-3 weeks of the effusive phase were marked by a decrease of the seismicity rate, with relatively large magnitudes (*Ml*:3-4.5) mostly for VT events. Oscillation of the effusion rate reached a peak of ca. 45 m^3/s the first days of August and renewed energy of the tremor decline to a minimum at the end of the phase simultaneously with the disappearance of the pyroclastic column.

Combining SAR scenes for 7 June and 7 July, an interferogram presented by Jay et al. (2014) and Wendt et al. (2017) covering the waning stage of the explosive phase and the initiation of the effusive phase, was modeled with a single deflating point source located 5-6 km below the active vent and accounting for a volume change of -0.12 to -0.17 km^3 (Fig. 4.4D). Continuous GPS observations presented by Wendt et al. (2017) are readily explained by this modeled source, although a significant misfit in the vertical GPS component in the southern flank of Puyehue Volcano, likely points to a localized movement of LOFZ (Fig. 4.1)

as can be also inferred by the occurrence of seismicity along the western branch of the fault zone.

4.5.7. Declining (7 August – 30 September)

During this period, a small diffuse eruptive column was observed, discharge rates of lava keep constant at relatively low values (20-30 m^3/s) and seismic activity remained at low levels. Sporadic VT events were recorded along the graben and south to the vent, likely along the LOFZ. During the second half of September, an increase of LP activity was recorded. InSAR images and GPS data during this phase, still show some subsidence but modeled point sources comprise lower volumes compared with previous phases (Jay et al., 2014; Wendt et al., 2017).

4.5.8. Resurging (1 October 2011– January 2012)

A rising number of LP seismic events during the second half of September anticipated a reactivation of the volcanic activity. This was associated with an increase in the amplitude of the quasi-harmonic tremor and a new emission of ash, explosions and effusion of lavas that lasted until January 2012. Jay et al. (2014) reported subsidence until February 2012. InSAR images studied by Delgado et al. (2016) however, showed a surface uplift of 0.8 m from March 2012 until the end of 2015. In this work they interpreted this uplift as an intrusion of magma at volumes similar to those expulsed during the 2011 eruption as modeled by Jay et al. (2014) and Wendt et al. (2017), i.e. 0.125 km^3.

4.6. Results and Discussion

Here we present the advanced post-processing of the seismic data compared to the available literature.

4.6.1.Local seismic velocity model and refined space-time evolution of relocated seismicity

Local seismic velocities resulting during the seismicity relocation process, are 1-2 km/s lower than the regional model of Bohm et al. (2002) at depth shallower than 6 km, with values of Vp near 5 km/s and Vs around 2.8 km/s. This large difference gradually decreases between 6 and 10 km however, below 6 km depth, both models get closer (Fig. 4.3). This is not surprising, since the model of Bohm et al. (2002) is for the entire arc-forearc crust between 38º and 40ºS, and our model has a local significance behind PCCVC. Rather, low velocities at shallow depths in figure 4.3, suggest a dominance of recent volcano-clastic rocks

likely affected by penetrative fracturing and/or as the effect of an active hydrothermal system (e.g. Sepulveda et al. 2006). A relatively sharp velocity contrast at 6 km depth likely constitutes a mechanical-rheological limit that could act as a barrier for magma mobility and be related to the stagnation of magma in a reservoir. The estimated depth of such a discontinuity lays at the upper bound of depths from deformation sources modelled from InSAR data (Jay et al., 2014; Wendt et al., 2017) and therefore, it is likely connected with the main magmatic reservoir below PCCVC. Seismic events registered by the network, were relocated on this locally computed seismic velocity model and are shown in Figure 4.4 (A, B, C and D). Comparatively few hypocentres were recorded during the initial unrest phase and they are roughly concentrated below Cordillera Nevada Caldera and the NW half of Cordón Caulle graben above 5-6 km. This area roughly coincides with the location of modelled point sources of surface inflation observed by InSAR some years, to several months before the eruption (Furnier et al., 2010; Jay et al., 2014) and the main deflationary source during the effusive phase of the eruption (Jay et al., 2014; Wendt et al., 2017). The fact that most of the events recorded during the initial unrest sub-phase were classified as VT, suggests that fracturing of rock above the main reservoir was a prevailing process to prepare the system for the eruption.
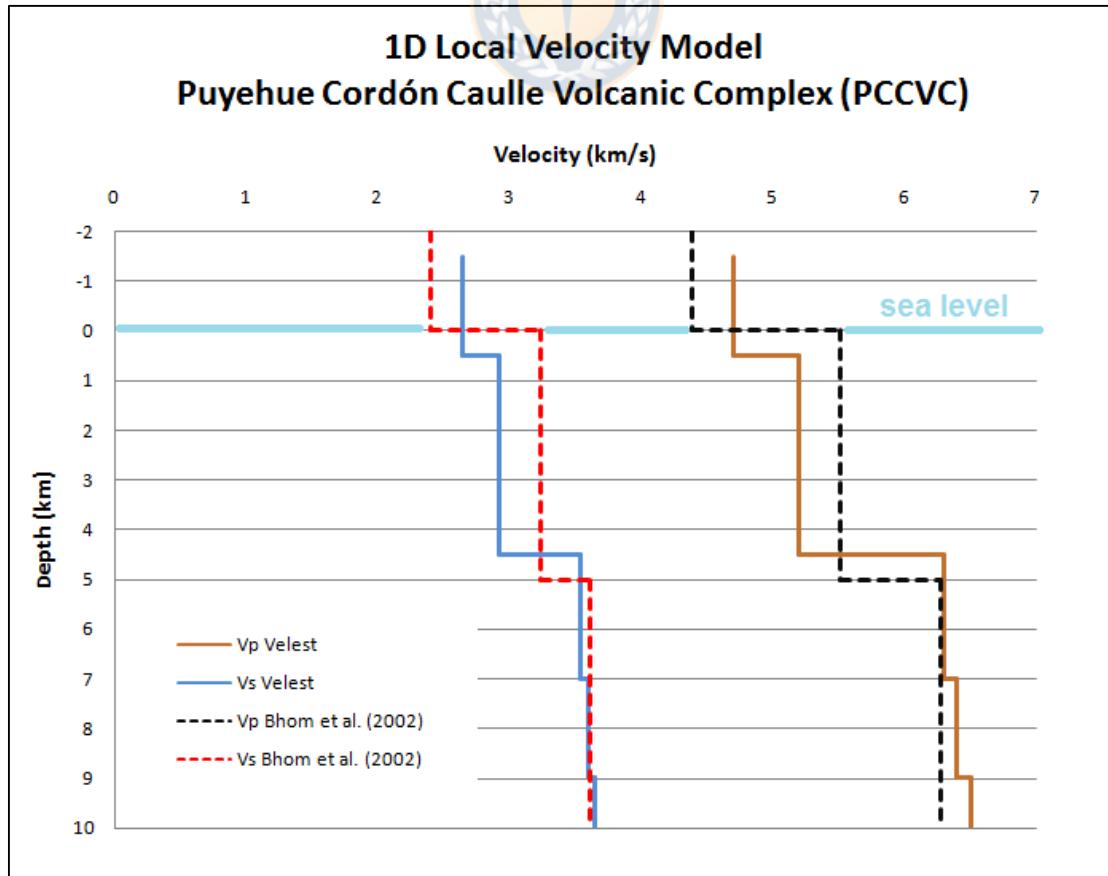
Figure 4.3. One-dimensional seismic velocity model (Vp red; Vs blue) obtained in this work (bold lines) compared with the one of Bohm et al. (2002, segmented line). The level 0 Km is related to the top of the Cordón Caulle graben (1.5 km above the sea level). The Bohm el al. (2002) velocity model started in -2 km and the 0 km is the sea level. Fuente: elaboración propia.
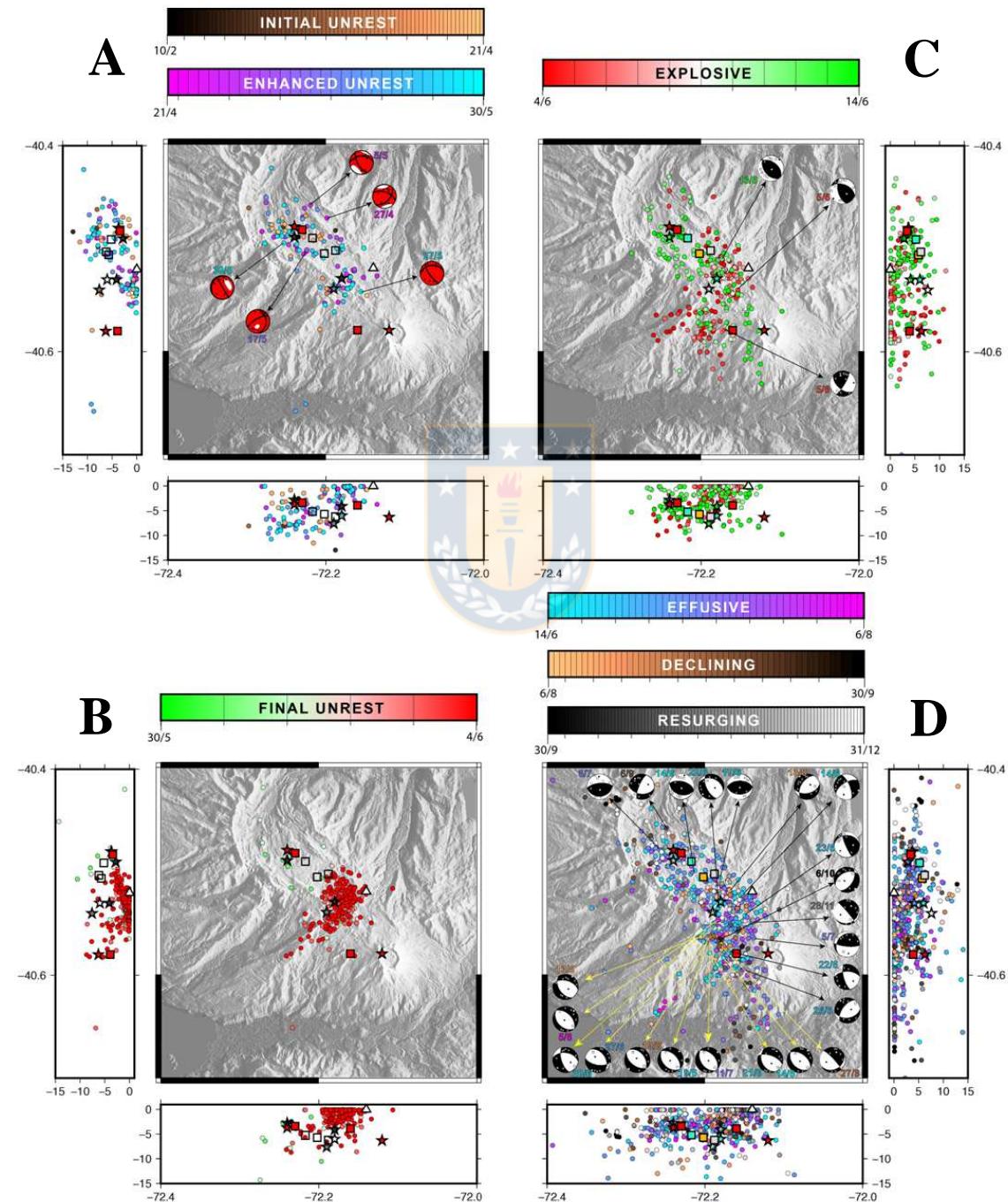
Figure 4.4.(Re)locations of seismic events recorded before (left, A-B) and after (right C-D) eruption onset. Events are coloured by day following codes defined for the different phases of the eruption. Focal mechanisms (A, C ad D) of some well-recorded events are also shown. White triangle is the eruptive vent. Location of deformation sources modelled by Jay et al. (2014, starts) and Wendt et al. (2017, squares) are either transparent (if they are inactive at the time of the respective panel) or coloured attempting to follow the codes of each phase of the eruption. Fuente: elaboración propia.

The appearance of LP and HB events near the beginning of the enhanced unrest sup-phase (end of April 2011) likely responds to the initial mobilization of fluids (magmatic and/or hydrothermal) from the reservoir toward the final vent. Hypocentres for events of this phase do not show a clear migration of a seismicity front from one point to the other, but more a south-eastward expansion of seismicity to shallower depths (<5 km) along Cordón Caulle graben and to deeper levels (up to 10 km) below Cordillera Nevada. The increasing number of LP and HB events mixed with comparable numbers of VT events, suggest that increasing amounts of fluids were injected at high pressure from the main reservoir below Cordillera Nevada, gradually invading the fault system underneath Cordón Caulle graben and opening paths for the movement of magma and gases to the surface.
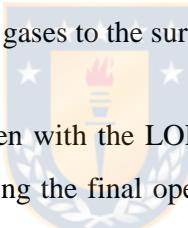
At the intersection of the graben with the LOFZ, a lower brittle strength of the rock massif was likely important for allowing the final opening of the vent. After several days of shallow seismic activity along both structures (graben-LOFZ), indicate the final unrest sub-phase. Events recorded during this phase, form a somehow diffuse grouping aligned with the NW-SE branch of Cordón Caulle graben and a more sharp NE-SW alignment at the western flank of Puyehue Volcano, that could be related with a western branch of LOFZ. The erupting vent is clearly located at the intersection of these two groups of events. Two days before the eruption, nearly 4200 counted events of all types were concentrated in a single and shallower area where the vent was finally opened. The total energy calculated from these events during the final pressurization of the system were 1.65×10^{20} ergs, representing an accumulated moment equivalent to a M_W:5.6 earthquake.

During the Explosive Phase of the eruption, the number of recorded events was gradually decreasing (Fig. 4.2) but their hypocenters spread out from the vent area covering the entire graben back to Cordillera Nevada (Fig. 4.4). The region identified as the sources of the 2008-2009 inflation event, were followed by a main co-eruptive deflation (Jay et al., 2014; Wendt et al., 2017). Also during this phase, a group of events formed a roughly NS

alignment southward of the vent and covering the western and southern flank of Puyehue volcano. This area roughly have coincidences with the secondary deflation source identified by InSAR studies (Jay et al., 2014; Wendt et al., 2017) and marks the possible activation of the main trace of the LOFZ.

The main area occupied by locations of events recorded during the Effusive Phase, does not differ markedly with respect of those of the Explosive Phase. Although, we note that seismicity tend to expand to the south-western flank of the complex and to deeper levels in comparison with the previous phase. This correlates with a larger depth of the deflation source, that explains a more regional surface deformation observed by InSAR (Jay et al., 2014; Wendt et al., 2017) during the Effusive Phase.

Events belonging to the Declining Phase maintain the distribution and tendency of the previous phase, but at the end of it the Resurging Phase shows an expansion of seismicity mostly outside the northwestern border of Cordillera Nevada caldera and southward of Puyehue volcano. The seismic distribution of this phase occurs along the main trace of LOFZ. By the second half of the Resurging Phase, seismic events tend to retract to locations similar to the Effusive Phase.
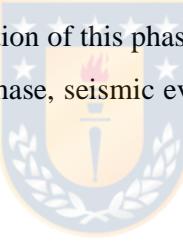
4.6.2. Focal mechanisms

At the beginning of the Enhanced Unrest Phase at April 27th, a large HB event (*Ml*:4.5) was recorded by the network. During this phase, other events with similar features (predominance of impulsive compressive polarities, high frequency at the beginning of the signal, followed by dominant frequencies <0.7*Hz*) were also registered. We used Full Moment Tenor inversion (Full MT) with ISOLA software, to obtain focal mechanisms of the five largest events of this type in the Enhanced Unrest Phase, as shown in figure 4.4 (and summarized in Supplementary Material Figure S6 and Table S1). These waveform inversions were complemented with the observation of first arrivals (all compressive), as shown in Fig. 4.4. These events are dominated by a non-double-couple (NDC) focal mechanism, with percentages of the double couple (DC) component as low as 10 to 40%. Full waveform inversion of some of these events, confirmed the dominance of the NDC component before the eruption (see Supplementary Material). This component is formed by an undetermined percentage of an isotropic component (ISO, also known as volumetric; e.g. Křížová et al., 2013) and a compensated linear vector dipole (CLVD) component. This combination has

been commonly interpreted in other volcanic areas, as caused by magma mobilization and intrusion (Aki 1984; Julian and Sipkin 1985; Dreger et al., 2000; Sarao et al., 2001; Templeton and Dreger 2006), in contrast with lateral slip along a fault plane as for DC-dominated focal mechanisms.

After the eruption onset (mainly Explosive, Effusive and Declining Phase), it was possible to compute 26 focal mechanisms using the first motion method on well-recorded VT´s (double couple earthquakes; Fig. 4.4). Most of these focal mechanisms, have been described for events occurring during the Effusive Phase. We note three main sources acting simultaneously during this phase. One of them is marked by events with dominantly reverse focal mechanisms that are aligned with the northern branch of the graben. They show strikes between NW to EW, i.e. roughly parallel to the strike of the Cordón Caulle graben. At the southern limit of this graben, the second group of events with a common focal mechanism of normal faulting is recognized with a dominant NW strike, which is totally parallel to the graben. A third group of events with dominantly strike-slip focal mechanisms, is recognized at the eastern portion of the graben near the intersection with LOFZ, suggesting an activation of this structure. Finally, ensuring the proper functioning of ISOLA software, we tested the quality of the solution using Full MT inversion. The results from the largest VT earthquake recorded at June 20th were compared using both; waveform inversion v/s fist polarities focal mechanism, obtaining similar results.

4.6.3. Temporal variations of the *b-value*

We computed a temporary variation of *b-value* using the seismicity recorded from May to December 2011 as shown in Fig. 4.2D. At the end of the Enhanced Unrest Phase, we note that the *b-value* was relatively constant near 0.7, but entering the Final Unrest, it started to rapidly decrease to values less than 0.3, mostly 2 days before the eruption. This is related with a marked increment in the magnitude of HB and VT events, days before the eruption onset (Fig. 4.2C). After this onset, the seismic magnitudes decrease gradually but keeping relatively constant number of events per day, which means that the *b-value* increases constantly during the explosive phase. A couple of days before the beginning of the Effusive Phase, the *b-value* stabilizes near 1.2, which is the maximum value computed for this time-series. Days after the end of the Explosive Phase, values of b decreases again and then increases to near 1, and this value is maintained until mid July. The second half of the effusive phase, is marked by a gradual decrease of *b-value* until the end of August into the

Declining Phase, but then this tendency reverts with a much gradual increase until the end of the analysed time window.

The development of an important seismic activity during the volcanic crisis, allowed us to define a local 1D velocity model for the volcanic complex. It was possible to calculate a superficial velocity model lower than the regional velocity defined by Bohm el al. (2002), which is consistent with an important hydrothermal system described by Sepulveda et al. (2005). In the same way, it was possible to identify a second relevant velocity change on 1D close to 6 km depth. This discontinuity would facilitate the lodging of shallow siliceous magmas, which is a common feature observed in other historical eruptions related to rhyolitic magmas (e.g. Novarupta-Kadmai 1912 and Chaitén 2008). This condition probably facilitate the formation of surface magmatic chambers associated with extensive hydrothermal systems.

With a 1D local velocity model defined, it was possible to relocate the seismic activity establishing a space-time evolution of the seismicity. This model helped to understand how different structures were reactivated throughout this volcanic complex in the eruptive crisis. The initial Unrest Phase, showed a deepest seismicity (mainly VT) located under the Caldera Cordillera Nevada, evidencing the reactivation of a deep reservoir, which is consistent with the InSAR data proposed by Fournier et al. (2010), Jay el al. (2014) and Wendt et al. (2016). In the Enhanced Unrest Phase, the seismicity was deployed mainly in the graben, migrating its location towards the east, decreasing the seismic depth. In this phase, it was possible to identify a predominance of HB/VLP seismic activity, which as a result of waveform inversions was possible to define as a non-double-couple (NDC) origin. These results are consistent with a migration of magmas/hydrothermal fluids through cracks/dikes as seismic sources. This NDC seismicity related to volumetric sources (compensated-linear-vector-dipole [CLVD] + isotropic [ISO]), were characterized by predominance of impulsive compressive polarities, showing a high frequency at the beginning of the signal, followed by predominant frequencies below 0.7 *Hz*. This behavior has been interpreted as an intrusion mechanism through dikes in active volcanic systems (Aki 1984; Julian and Sipkin 1985; Chouet 2003; Křížová et al., 2013). In this context, other volcanic systems have shown similar seismic events related with crustal deformation, suggesting the mobilization of magmatic fluids (Dreger et al., 2000; Sarao et al., 2001; Templeton and Dreger 2006). As shown in Table S1 (Supplementary Material), waveform inversions and polarities of first arrivals (Fig.

4.4A), suggest a predominant NDC for their sources. In this sense, the Okada model deformation proposed for dike-source by Wendt et al. (2016) and the petrologic analyses developed by Alloway et al. (2015), suggested an active role of dikes in the process of lodging, ascent and subsequent extrusion of rhyolitic magmas in 2011 PCCVC eruption. These studies are consistent with our results of the seismic sources that represent a movement of magma into mesh-dikes along the graben structures. The compressive polarities and waveform inversions are consistent with a volumetric change generated by a magmatic migration through open-cracks in a rhyolitic high pressure system. If we want to define the predominant stress field however, one possibility is try to use the seismic waveforms inversions to define P and T axes. The problem of NDC solution is that the results have an important volumetric component, for that reason it is hard to find the location of the principal stress field direction (σ1) that finally triggers the eruption. In the Final Unrest Phase, the NDC dominate the seismic activity becoming shallower and reactivating a branch of the LOFZ that is located outside the graben (southern sector). The 2011 vent was located where the two most important structures of the complex are intercepted, confirming the most brittle and heterogeneous area of the system. If we assume that the final phenomena triggering the eruption was the super-pressurization system (phenomena consistent of seismic migration along the graben) the local stress field in the volcano before the eruption, is related by the saturation of gases pushing the magma to the surface.

After the eruption onset, seismicity radically changed during the Explosive Phase, decreasing the earthquakes number and their magnitudes. However, the main change observed were produced in the frequency content of the seismic signal. Before the eruption (Final Unrest Phase) the seismicity predominance was mainly the low frequency activity HB (Supplementary Figure S1), meanwhile after the eruption, the seismogram showed only VT´s high frequency activity (Supplementary Figure S4). These changes are consistent with the evolution of volcanic processes. Before the eruption (Enhanced and Final Unrest phases), the seismic source was related with magmas intrusion through to the dikes (HB seismicity). Then, the post-eruption (opening of a high pressure system, Explosive and Effusive Phases), were controlled by a deflation of the system promoting mainly VT seismicity. The solutions of the focal mechanism at the end of the Explosive Phase and the beginning of the Effusive Phase, were located in the north wall of the graben, showing mainly inverse solutions (Fig. 4.4). This behavior is consistent with shallow intrusion of viscous magmas such as laccolith described

by Castro el al. (2016). Whereas, the Effusive Phase showed solutions of the focal mechanisms located in the southern wall of the graben predominantly normal, being consistent with the deflationary phase of the complex. Likewise, it was possible to establish dextral slip solutions in both phases, consistent with the LOFZ located in the east sector of the graben next to the Puyehue volcano. During the Effusive and Declining phases, a repetitive seismicity was generated with a common source. The similarity in the waveform, are consistent with similar solutions of 10 focal mechanisms (Fig. 4.4D, yellow arrows). The average of this 10 azimuth of focal mechanism solutions resulted in N150° (standard deviation=18°; dip:24° to 82° and Rake:-45° to -63°), evidencing the participation of the southern wall of the graben in the deflationary repetitive process. Finally, it should be noted that this average azimuth was calculated according to the Okada inversion reported by Wendt el al. (2016), corroborating the importance of this structure in the hosting and migration of magmas.

In general, the *b-value* is a measure that quantifies seismic production in terms of its spatial and temporal magnitudes for a specific area/volume (Scholz, 1968; Wyss, 1973). This quantification allows to establish the characterization for the different local tectonic stress regimes (Wiemer et al., 1996; Schorlemmer et al., 2004, Schorlemmer et al., 2005). Both temporal and spatial variations of the *b-value* have been interpreted as changes in an active framework regional tectonic stress (Gőrgün, 2013). In volcanic zones, the *b-value* has been associated with migration of magmatic/hydrothermal fluids which affect widely the volcanic arc (Enescu and Ito, 2003) or volcanoes such as Kilauea (Wyss et al., 2001), Augustin (Jacobs and Stephen, 2011) and Yellowstone (Farrell et al., 2009). The *b-value* was also used to infer the state of the differential stress (σ_D) in active faults, since Schorlemmer et al. (2005) showed the inverse relationship between this stress ($\sigma_D=\sigma1-\sigma3$) and the *b-value* ($\sigma_D=1/b$), which can be interpreted as an indicator of crustal relaxation produced after a major earthquake. In this context, *b-value* in the Final Unrest Phase showed a sharp decrease, likely due to a significant seismic magnitude increment, related to a magmatic fluid migrations. This response suggest an imminent eruption triggering, due to a overpressure of the volcanic system (increment σ_D). In the Explosive Phase, the pressure was released to a huge eruptive column producing a spasmodic (poly-frequency) tremor (Supplementary Material S5-A). An increase of the *b-value* in this phase was observed, associated to a decrease of seismic magnitudes. Therefore, a relaxation (deflation) of the volcanic system were measure by GPS and InSAR (Jey et al., 2014; Wendt et al., 2016). In the beginning of the Effusive Phase, the *b-value*s again began to

decrease due to a new increase in seismic magnitudes. This second decrease in the *b-value* is consistent with the maximum laccolith intrusion under the vent and the emission of lava flows to the surface of graben, which is represented by the maximum values of the DR associated with the quasi-harmonic tremor (Fig. 4.2b). After that, the values of b increased again, decreasing the magma supply rate and the relevant seismicity, suggesting that the *b-value* is inversely proportional to the siliceous volcanic activity that promote a high σ_D. Finally, the temporal evolution of *b-value* in the volcanic crisis is consistent with the evolution of the stress in the PCCVC. However, the key of this b-value tool is to detect rush stress changes in an explosive volcanic system, being a useful tool to forecast catastrophic siliceous eruptions.

The PCCVC 1960 eruption, is known in the scientific field due to a connection to the Valdivia megathrust (M_W:9.5; Barrientos et al., 1990; Sepúlveda et al., 2005). In general, most of the volcanoes do not produce an eruption after a megathrust, unless the precondition of the volcano (static or dynamic stress (Hill et al., 2002; Brodsky et al., 1998). This precondition play a key role in the processes of volcanic reactivation. The dynamic stress change added to a favourable orientation of the structure hosting the magma (PCCVC), could promote the relaxation of the graben, favouring the extrusion of magmas at high pressure as a result of megathrust (Stanton-Yongue et al., 2016; Farias et al., 2017). These observations are consistent with the tectonic setting recorded in the PCCVC during the last decade. Between 2007-2008 the volcanic complex recorded several swarms (first unrest) associated with an intrusion of magma (InSAR, Fournier et al., 2010) without an eruption, verifying that the volcano was already in an unusual unrest. On February 27th 2010, the south of Chile suffered one of the largest earthquakes in its history (Maule Region, M_W:8.8), reactivating sections of the most important faults along the Southern Chilean Volcanic Arc (e.g. LOFZ, Andean Transverse Faults ATF). This phenomena accelerated the installation of the seismic network by OVDAS staff in the PCCVC at the end of 2010. Since December 15th 2010, an unusual seismic unrest were recorded probably promoted by the new local stress configuration generated after the Maule megathrust, favouring the activation of the NW structure graben containing magmas. In this context, after the first unrest recorded in 2007-2008, the magmatic fluids could climb easier due to the new configuration stress (post-megathrust period), increasing the seismic activity after the megathrust.

4.7. Conclusions

The 1D velocity model was useful to relocate all the seismic activity and fundamental to identify the spatio-temporal distribution of the seismicity. This model also helped to define the main structures activated in the volcanic process such as the graben or the LOFZ. The seismic sources before and after the eruption were calculated through the analysis of inversion and focal mechanisms, and these results allowed us to identify the role of the magma intrusion before the eruption and the subsidence thereafter, reactivating the local faults (LOFZ). The fluctuation of the b-value before, during and after the eruption, were helpful to identify these phases along the eruption. The tectonic configuration around the PCCVC and the existence of a megathrust recorded before the eruption suggest a link between this two phenomena however, this connection requires a previous condition; the volcano must be in a active status before the earthquake, and a correct orientation of the structure that host the magma is required.

CAPÍTULO V: Síntesis y conclusiones

La crisis volcánica registrada por el CVPCC durante 2011 fue la primera gran erupción explosiva de carácter riolítico que está relativamente bien documentada por redes sísmicas y geodésicas locales. Estas observaciones sugieren que la erupción estuvo controlada por la reactivación de las estructuras del basamento de rumbo NW que controlaron no solo el ascenso de magmas a través de diques, sino que además el emplazamiento del reservorio magmático principal (Fig. S7). El desarrollo de profusa actividad sísmica durante la crisis volcánica nos permitió definir un modelo local de velocidad 1D para el complejo volcánico. Este nuevo modelo evidenció velocidades considerablemente menores a los valores regionales propuestos por Bohm el al. (2002), resultados consistentes con un arco volcánico activo. Adicionalmente, fue posible identificar una relevante discontinuidad, la que se manifestó por un importante cambio de velocidades cercano a los 6 km de profundidad, estructura que facilitaría el alojamiento de magmas silíceos poco profundos, característica común observada en otras erupciones riolíticas históricas como Novarupta-Kadmai 1912 y Chaitén 2008, favoreciendo la formación de cámaras magmáticas superficiales. Con un modelo local de velocidad más preciso y representativo de la corteza, se consiguió relocalizar la actividad sísmica más relevante, logrando obtener una detallada evolución espacio-temporal de la sismicidad durante las fases pre y post eruptiva, identificando las principales estructuras que participaron en el proceso eruptivo (NW y NNE). La actividad sísmica más profunda comenzó debajo la Caldera Cordillera Nevada (CCN), sugiriendo el emplazamiento del reservorio principal bajo la caldera. La actividad sísmica luego migró a través del graben hasta el vent de 2011, distante 11 km del reservorio, reactivando toda la estructura de rumbo NW. Días antes de la erupción, se logró identificar la reactivación de la SFLO, sugiriendo que el vent de 2011 se localizó en la intersección del graben (NW) con el SFLO de rumbo NNE. Sísmicamente también se logró identificar un cambio en la evolución del proceso eruptivo. Si bien las fuentes sísmicas comenzaron siendo de origen volcano-tectónico (VT) bajo la CCN, estas evolucionaron hasta predominar la sismicidad de tipo híbrido (HB) días antes de la erupción. Para poder identificar la fuente (origen) de los sismos de muy baja frecuencia (VLP) que se registraron durante la fase pre-eruptiva, se realizaron inversiones de onda, las que arrojaron un origen de tipo volumétrico, denominados "No Doble Cupla" (NDC), los que fueron interpretados como actividad sísmica relacionada con importantes pulsos de ascenso/migración de fluidos magmáticos a través de una red de diques controlados principalmente por el graben (estructura NW). La migración de magmas también fue

consistente con la evolución espacio-temporal de la sismicidad, la que migró de Oeste a Eeste a lo largo del graben, produciéndose una superficialización de los enjambres dentro del graben desde la CCN hacia el cráter de 2011, distantes 11 km entre sí. Después del inicio de la erupción, la sismicidad cambió radicalmente. Estos cambios fueron consistentes con la evolución de los procesos volcánicos, ya que durante la fase pre-eruptiva, la fuentes sísmicas estuvieron relacionadas con el ascenso/migración de magmas (HB, VLP de tipo NDC), mientas que la fase post-erupción (fases explosiva y efusiva), la sismicidad estuvo controlada por sismos de tipo VT asociados con la deflación (colapso) del sistema volcánico y por un tremor quasi-armónico relacionado con la emisión de imponentes flujos de lava rioliticas en superficie. Debido a las características poco habituales que posee el tremor quasi-armónico, fue posible utilizar esta señal para identificar el fenómeno de extrusión de lavas rioliticas en superficie y además lograr cuantificar la tasa de emisión de lavas. Hay volcanes que debido a condiciones climáticas extremas y/o geográficas, es imposible llegar a realizar una estimación confiable de las tasas de descarga promedios de lavas, por lo tanto con el análisis sísmico de esta señal de tremor (amplitud, frecuencia dominante, distancia fuente-receptor y el D_R), es posible lograr estimar de forma fácil y precisa la tasa de descarga (emisión de lavas) en superficie. De hecho, de la misma manera que Battaglia et al. (2005) encontró relaciones empíricas entre amplitud de tremor y las tasas de flujo de lava, hemos observado una relación general entre el D_R del temblor cuasi-armónico y tasas de descarga promediadas en el tiempo, sugiriendo que el D_R se puede utilizar como un proxy de la tasa de efusión a lo largo de todo el ciclo eruptivo. Las elevadas tasas de descarga observadas para el CVPCC muestran que los altos valores serían más comunes para las erupciones silícicas de lo que se pensaba, especialmente durante las etapas iniciales de la erupción, esto debido a las implicancias directas que se generan al momento de evaluar el riesgo en el manejo de una crisis volcánica explosiva.

Después del inicio de la erupción, los mecanismos focales calculados durante la fase efusiva mostraron soluciones principalmente normales, siendo consistentes con la fase deflacionaria del complejo. Asimismo, fue posible establecer soluciones de deslizamiento dextral, siendo consistentes con el SFLO, sistema que se localiza en el sector Este del graben y que tuvo un rol en la fase final de la erupción. Debido a la profusa sismicidad registrada en la pared sur del graben, se calculó el azimut promedio para los 10 mecanismos focales más importantes de esta zona, arrojando un valor de N150° (desviación estándar σ=18°), sugiriendo la participación del muro sur del graben en el proceso deflacionario. Cabe destacar que este acimut promedio es consistente con la inversión de Okada reportada por Wendt el al.

(2016), corroborando la importancia de esta estructura en el hospedaje y migración de magmas durante el ciclo eruptivo. El valor de b es una medida que cuantifica la producción sísmica en términos de sus magnitudes espaciales y temporales en una crisis volcánica. En este contexto, los bajos valores de b registrados 2 días antes de la erupción evidenciaron un sistema volcánico sobrepresionado, relacionado con importante actividad sísmica. Ya generada la erupción, la presión del sistema disminuyó, y con ello, el aumento del valor b, sugiriendo una disminución de las magnitudes sísmicas. Durante la fase efusiva, los valores de b nuevamente fluctuaron siguiendo el patrón antes descrito, por ende, se propone que el valor de b es inversamente proporcional a la actividad volcánica silícea. Finalmente, la evolución temporal de b puede ser utilizada para detectar cambios bruscos de estrés en sistemas volcánicos explosivos, siendo una herramienta útil que podría pronosticar futuras erupciones de carácter explosivo.

En general, la mayoría de los volcanes no entran en actividad después de un terremoto, a menos que las condiciones previas de un volcán activo logre acelerar un proceso inestable en gestación. De igual forma, un cambio de estrés dinámico sumado a la orientación favorable de una estructura que alberga un magma somero, podría fomentar el ascenso de fluidos magmáticos. Estas observaciones son consistentes con el marco tectónico registrado para el CVPCC antes de la erupción de 2011, ya que durante los años 2008-2009 el volcán registró un cambio de alerta volcánica (Alerta Naranja) producto de una intensa actividad sísmica precursora, seguido un año después por un terremoto de magnitud Mw:8.8 (Febrero 27 de 2010). De esta forma, se sugiere que la inestabilidad volcánica registrada en 2008-2009 sumada a la configuración tectónica de las estructuras que alojan el magma (NW) pudieron favorecer el movimiento/ascenso de fluidos magmáticos producto del terremoto Mw:8.8, acelerando el proceso eruptivo para el CVPCC. Finalmente si consideramos que este sistema volcánico está inmerso en una estructura NW orientada favorable a una respuesta estática (Stanton-Yongue 2016) y dinámica (Farías et al., 2017) gatillada por terremotos de subducción, es posible perturbar un reservorio magmático o hidrotermal somero, ya que el CVPCC posee uno de los sistemas hidrotermales más importantes de la zona sur del país.

Material Suplementario

Here we present a number of figures and a table that compliment part of the results discussed in the main text.
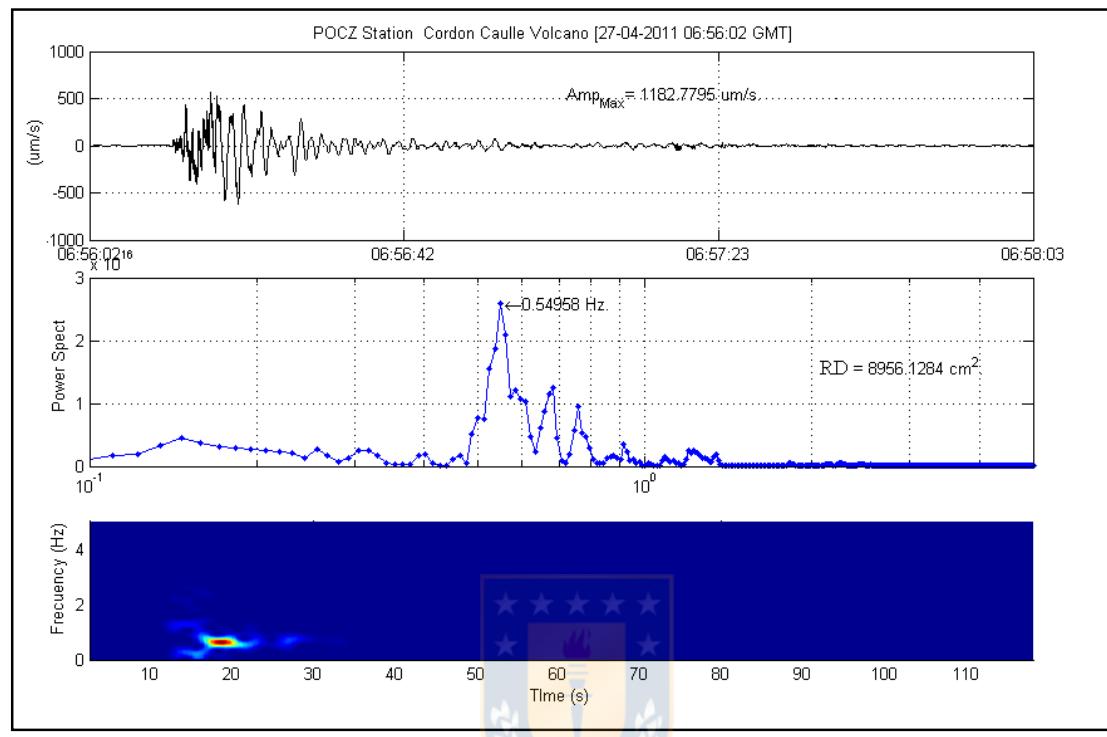
Figure S1. HB the typical waveform of the seismic events before the eruption. Earthquake classified as HB registered by POC station on April 27th, 2011, with an *Ml*:4.6. The amplitude is measurement in micrometers/second. Below, it shows the spectra in seismic power and finally the spectrogram in Hz. This event had a *RD*: 8,956.1 cm^2 and was recorded throughout the RNVV, from the Lascar volcano (1,950 km) to the Hudson volcano (610 km), distant respectively of the PCCVC. Fuente: elaboración propia.
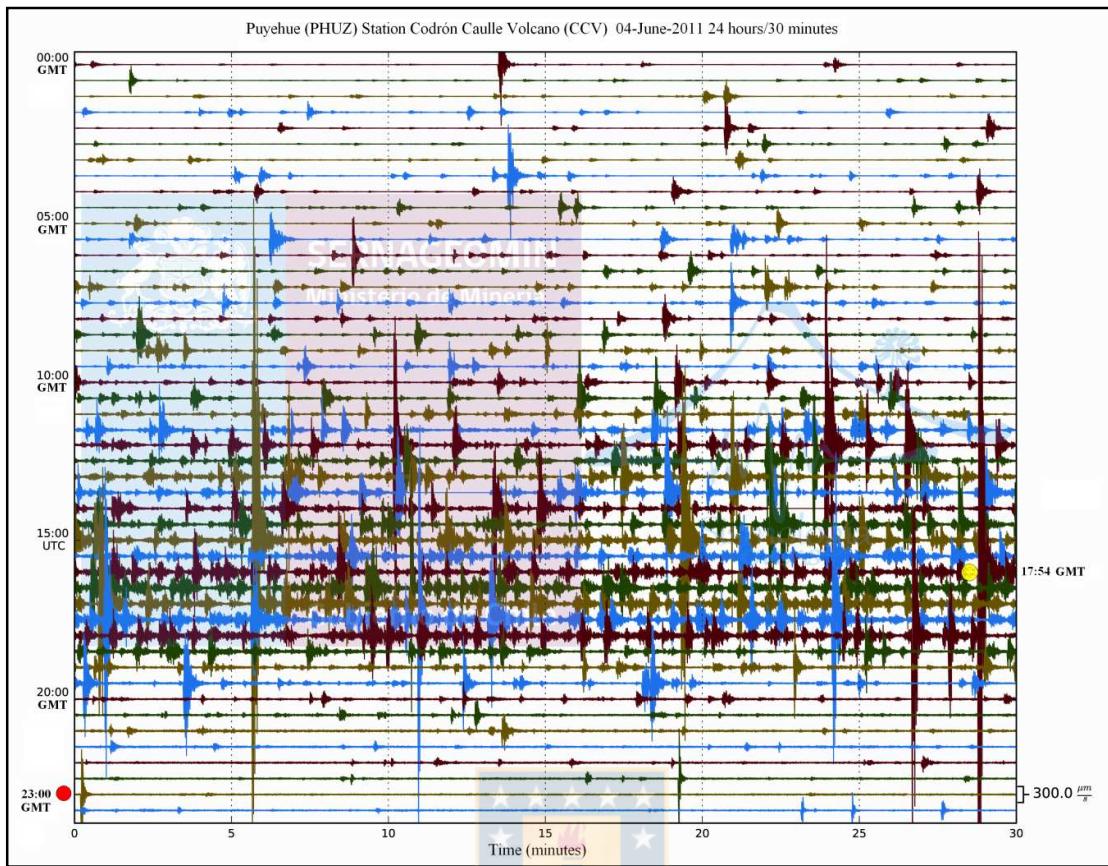
Figure S2. Continuous seismic record at PHU station seismogram (vertical component) 24 hours/30 minutes registered on June 04th, 2011.Two classes of earthquakes are highlighted given that represent the seismic onset process 4 June eruption and the subsequent post-eruptive seismic change. The first was classified as VLP recorded before the eruption (17:54 GMT, yellow dot). The second earthquake highlighted was generated after the eruption (23:00 GMT, red dot). Each of them is detailed in the supplementary figures S3 and S4. Fuente: elaboración propia.
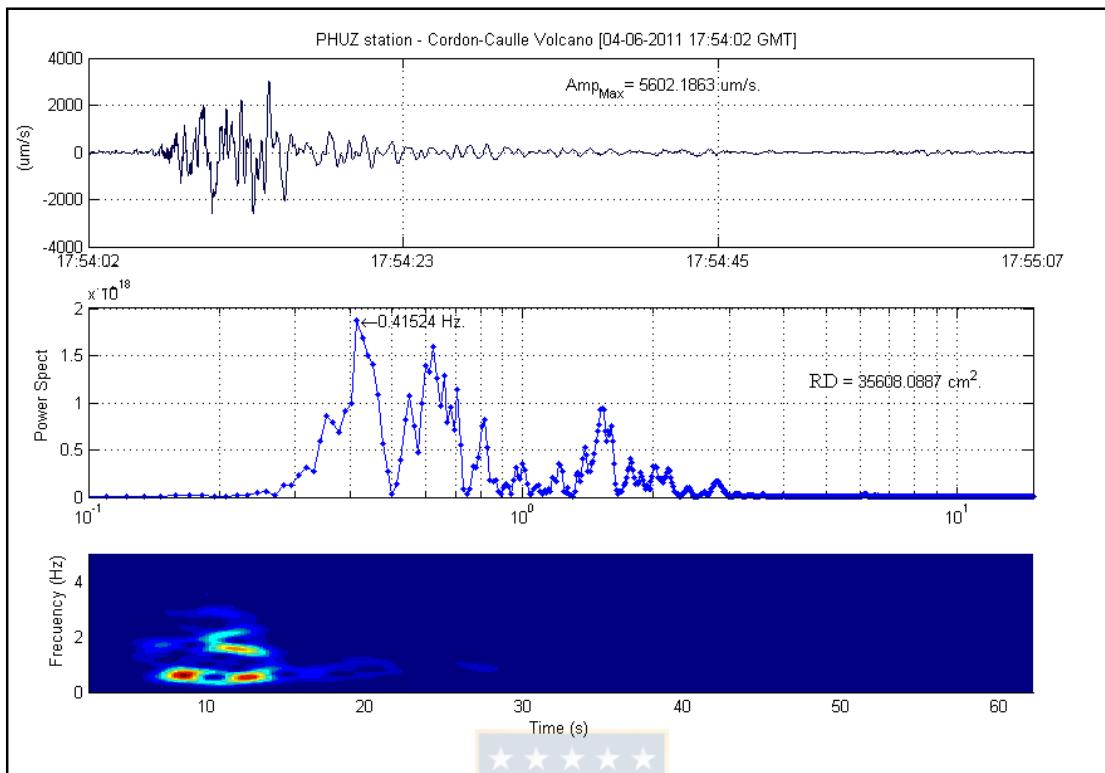
Figure S3. Earthquake classified as VLP registered by PHU station on June 04th 2011 17:54 GMT (yellow dot Fig. S1), before the eruption with a *Ml*:4.9. The amplitude is measurement in micrometers/second. Below, it shows the spectra in seismic power and finally the spectrogram in Hz. This event had a *RD*= 35.608 cm^2. Fuente: elaboración propia.
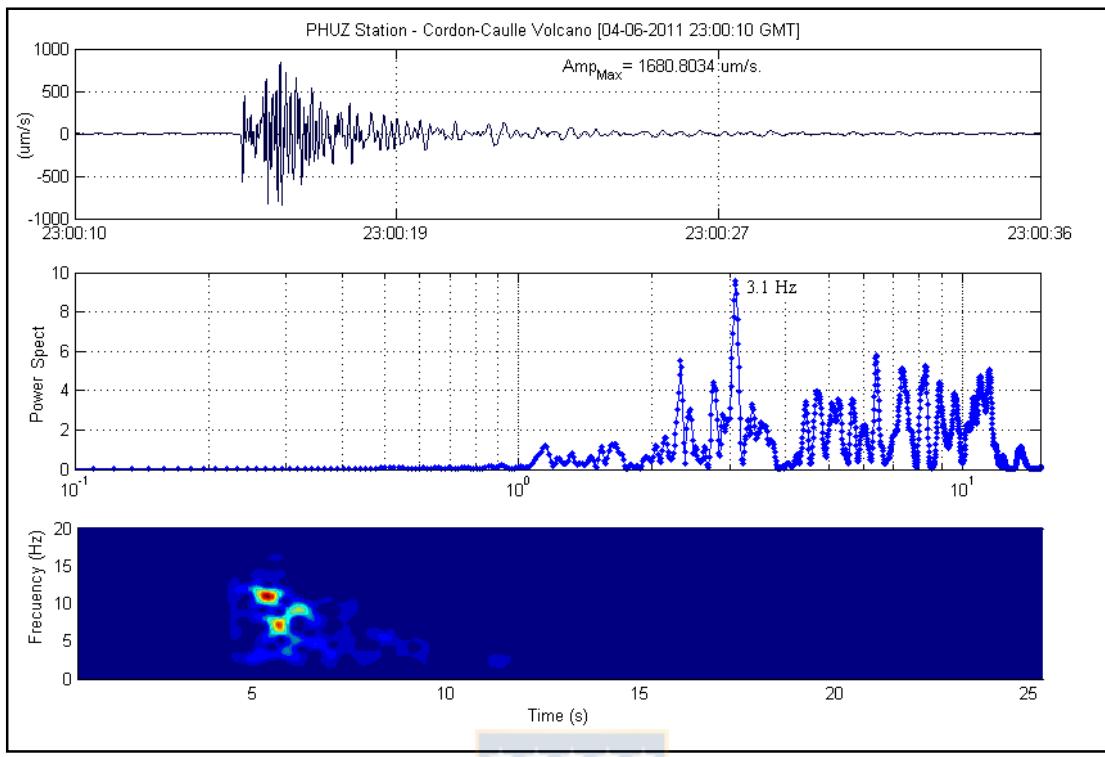
Figure S4. VT the predominance waveform of the seismic events after the eruption. Earthquake classified as VT registered by PHU station on June 04th 2011 23:00 GMT, with a *Ml*:3.8. The amplitude is measurement in micrometers/second. Below, it shows the spectra in seismic power and finally the spectrogram in *Hz*. Fuente: elaboración propia.
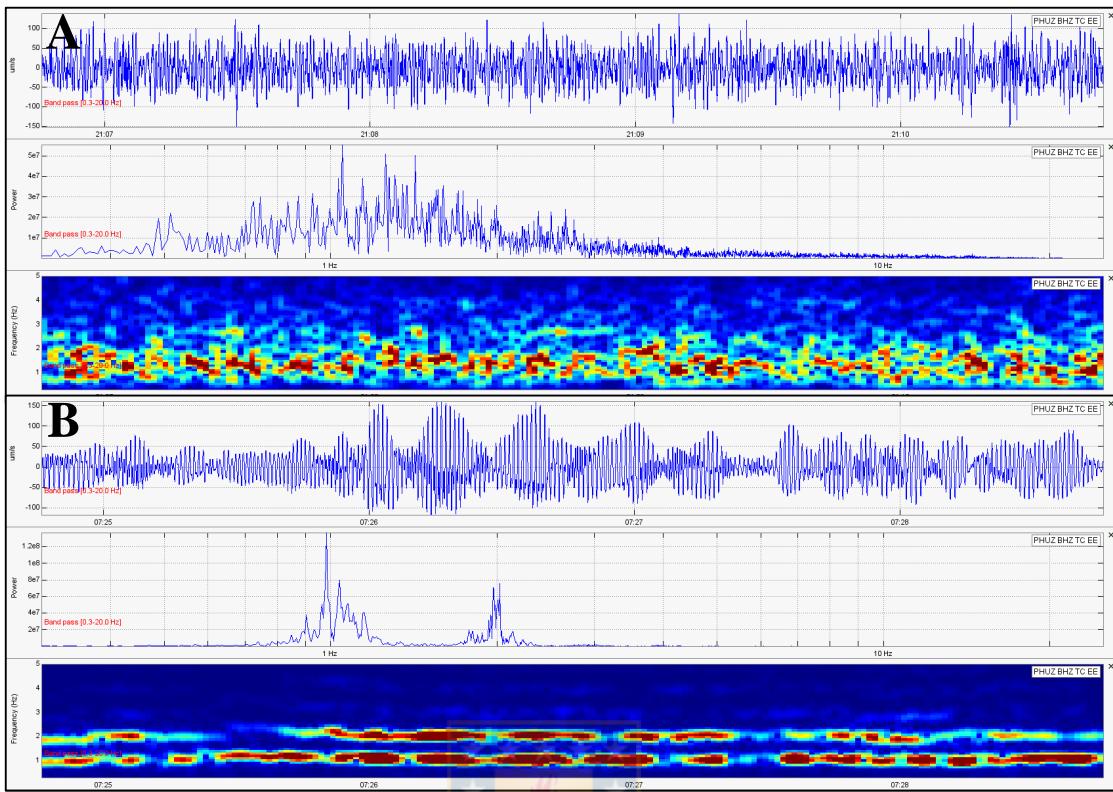
Figure S5-A. The velocity seismogram of spasmodic tremor with its related spectrogram pattern. **S5-B.** The velocity seismogram of tremor with its related spectrogram highlighting the quasi-harmonic pattern within the dominant frequency. PHU is the closer station to the vent (~8 km, Figure 1). Fuente: elaboración propia.
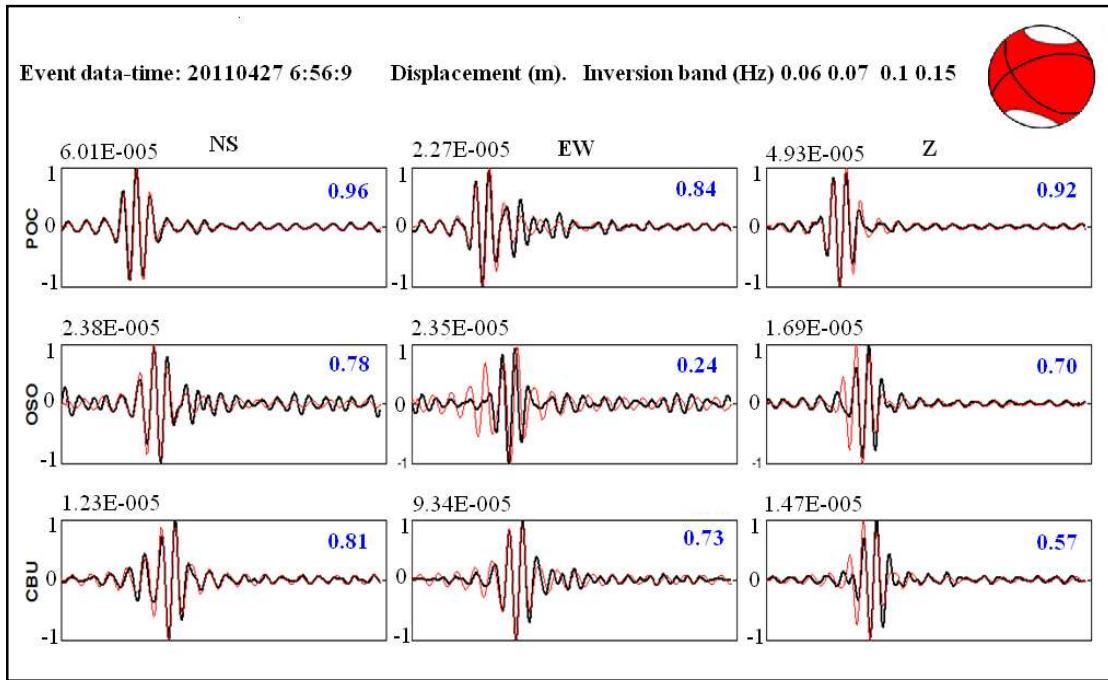
Figure S6. Hybrid (HB) seismic inversion *Ml*:4.5 registered on April 27th, 2011 filtered 0.06-0.15 *Hz*. Red seismogram shows the synthetic signal, while the black seismogram represents the signal recorded by different stations. The blue numbers represent the reduction of variance. The amplitudes of the signals are normalized and also are shown in meters. Fuente: elaboración propia.
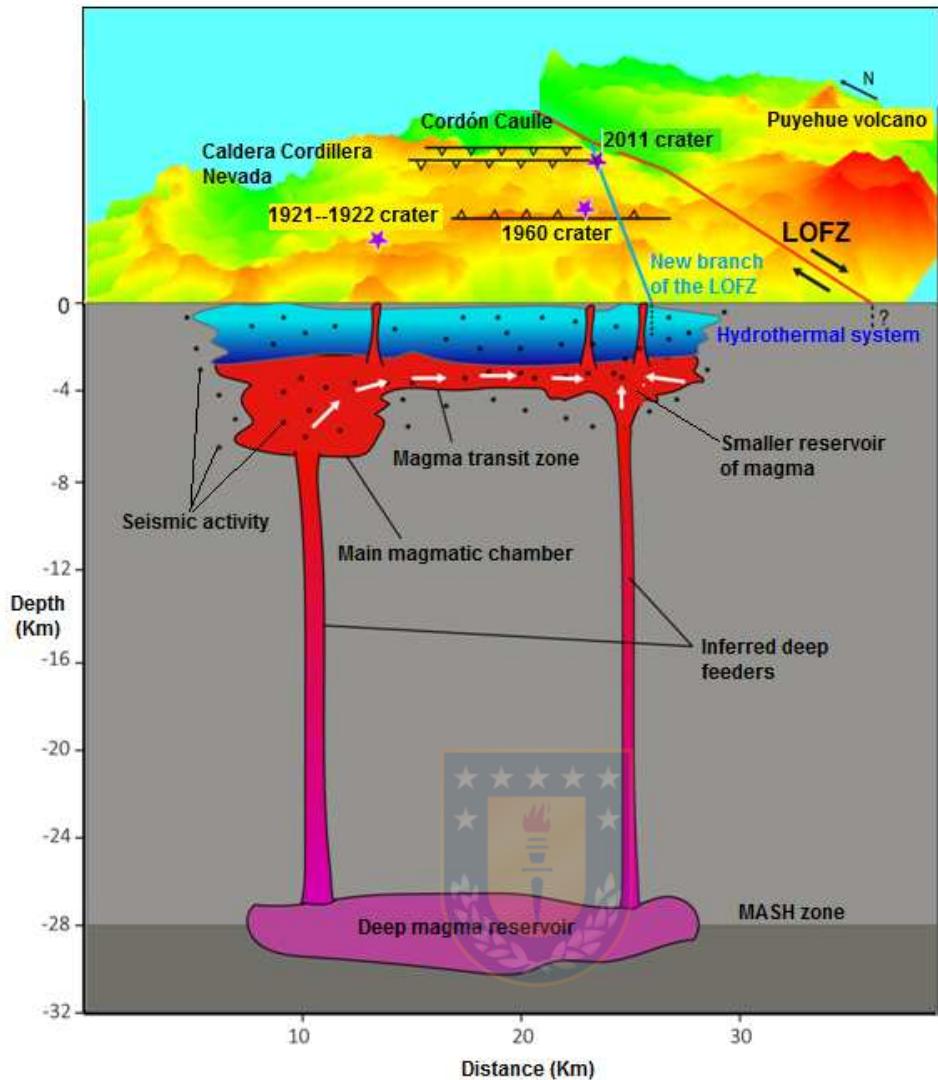
Figure S7. Conceptual model of the main structures present under the Puyehue-Cordón Caulle volcanic complex (PCCVC). The figure shows seismic activity (random dots), a main magmatic reservoir under the Caldera Cordillera Nevada, a zone of transit of magmas under the Cordón Caulle, a shallow hydrothermal system and a new branch of the LOFZ, which is intercepted with the northern wall of the graben where the eruption of June 4th, 2011 occurred. Additionally, the location of the historical eruptions and their possible deep feeders. Fuente: elaboración propia.

Data (time GMT)	Deep (km) Magnitude	Stations	Filter inversion	% DC %CLVD+ISO	Variance Reduction	Focal Mechanism
April 27 06:56	4.3 *Ml*=4.5	POC OSO CAL	0.07-0.15	DC=16.6 CLVD+ISO=83.4	0.7	
May 05 02:09	4.6 *Ml*=4.2	POC PHU RAN	0.09-0.18	DC=39.6 CLVD+ISO=60.4	0.6	
May 17 14:31	4.1 *Ml*=3.7	POC PHU RAN	0.1-0.21	DC=34.5 CLVD+ISO=65.5	0.62	
May 27 08:30	4.2 *Ml*=4.1	POC PHU RAN	0.07-0.17	DC=9 CLVD+ISO=91	0.55	
May 30 19:36	4.0 *Ml*=3.6	POC PHU RAN	0.12-0.2	DC=28.6 CLVD+ISO=71.4	0.56	
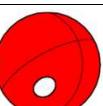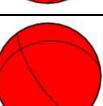
Table S1.-Focal mechanisms inversions of large HB events of the unrest enhanced phase.Main characteristics of the earthquakes before the eruption made with ISOLA software. It highlights its depth,Local Magnitude (*Ml*), the stations used in the inversions, the filter range, the percentages of the mechanism involved in the seismic source, the reduction of variance, and finally a graph to the focal mechanism obtained. The locations of these earthquakes are showed in the figure 4 (left). DC= double couple, ISO=isotropic, CLVD= compensated linearly dipole vector. Full wave inversion of some of these events confirmed the dominance of the NDC component. Fuente: elaboración propia.

Anexos

Metodologías

Modelo 1 D De Velocidades En El Complejo Volcánico Puyehue Cordón Caulle CVPCC

El problema del tiempo de llegada de una onda sísmica generada por un sismo es una función no lineal de:

1.- Las coordenadas de la estación (s)

2.- el hipocentro (h, incluyendo el tiempo de origen)

3.- Campo de velocidades (m),

Es así que "el tiempo observado" será igual a:

$$\textbf{t observado= f (s h m)}$$

En general, tanto los parámetros hipocentrales como el campo de velocidad, son desconocidos. Las únicas variables medibles con las cuales podemos trabajar son: a) los tiempos de llegada a cada estación, y b) la ubicación de cada una de estas estaciones. Para comenzar debemos trabajar bajo un modelo inicial, en el que trazaremos los rayos de una fuente (hipocentro) a una receptora (estación), y calcularemos los tiempos de llegada teóricos (tcalc). La diferencias entre los tiempos observados y los calculados (el tiempo de viaje residual "tres"), se pueden resumir como funciones de las diferencias entre el tiempo estimado y el tiempo verdadero, este último relacionado con la velocidad, para finalmente ajustar (mediante correcciones) el modelo inicial. Es necesario conocer la dependencia de todas las observaciones (los tiempos de viaje entre fuente-receptor) y corregirlos. Esta dependencia es moderadamente no lineal para los parámetros de velocidad, incluso en un modelo 1-D (Pavlis y Booker , 1983). La aplicación de la serie de Taylor de primer orden en el desarrollo de la ecuación (1) nos permitirá acercarnos a una relación lineal entre el tiempo de desplazamiento residual, el ajuste de los hipocentros (Δhk) y la velocidad (Δmi).

$$t_{res} = t_{obs} - t_{calc} = \sum_{k=1,4} \frac{\partial f}{\partial h_k} \Delta h_k + \sum_{i=1,n} \frac{\partial f}{\partial m_i} \Delta m_i + e. \qquad \textbf{(1)}$$

La localización de los sismos, tiene el potencial de introducir errores sistemáticos. De igual manera, el modelo de capas puede dar lugar a parámetros de velocidad sesgados (Vander Hilst y Spakman. 1989), no obstante, la inclusión de ambos parámetros (solución de los hipocentros y el modelo de velocidad) en el procedimiento no nos garantiza

necesariamente una recuperación exitosa de la distribución de velocidades. Bajo el supuesto de errores distribuidos normalmente, y la existencia de perturbaciones en el modelo, el trabajo con mínimos cuadrados (RMS) nos ayudará a aproximarnos a una solución más probable; la que estará relacionada directamente con la familia de soluciones del modelo de referencia inicial. De ahí la importancia de elegir un modelo inicial coherente con los datos. Establecer el modelo 1-D.

En general, el uso de modelos sísmicos de refracción, simplifica la elección de capas de velocidad constante. Por otro lado, inferir la estratificación estructural mediante el uso de información geológica también nos puede llevar a elegir un buen modelo inicial. No hay que olvidar que para definir un buen modelo, se deben definir varias capas, las que deben ir aumento su velocidad con la profundidad. Se recomienda utilizar espesores en la corteza superior que no superen los 2 km, y en la corteza inferior que no sobrepasen los 5 km. Se debe tener presente que al momento de seleccionar una estación de referencia, esta no muestre importantes efectos de sitio, que posea un extenso registro y que preferentemente esté situada hacia el centro de la red.

Geometría e intervalos de velocidad del potencial modelo 1-D

Para trabajar con el programa VELEST, se debe seleccionar como máximo 500 eventos (es decir, aquellos con el mayor número de P de alta calidad, con un azimut < 180º), que posean una calidad B o A y de preferencia, cubran toda el área de trabajo. Relocalizar los sismos con la rutina VELEST utilizando un coeficiente de amortiguación de 0,01 para los parámetros hipocentrales, 0,1 tanto para los retardos de las estaciones como para los parámetros de velocidad y una relación Vp/Vs 1,78 y 1,75. "Cabe destacar" que para obtener una buena solución, se sugiere invertir los tiempos de los hipocentros en cada iteración, pero tanto los retardos de las estaciones como los parámetros de velocidad, solo en la segunda iteración. Esto se consigue modificando el archivo "velest.cmn"/línea 37 en "invertratio" debe tener un número 2. Repita este procedimiento varias veces, pero no olvidar utilizar las nuevas velocidades referidas al modelo 1-D con los nuevos retardos de las estaciones utilizando las nuevas localizaciones hipocentrales. Trate de reducir el número de capas cuando sea posible, mediante la combinación de capas adyacentes con velocidades similares. En la mayoría de los casos, es preferible evitar capas superficiales de baja velocidad, ya que normalmente introducen inestabilidades en el cálculo de las soluciones. Kissling (1994), sugiere que los

datos obtenidos por disparos o explosiones artificiales, no deben ser incluidos en la inversión del modelo 1-D calculado mediante hipocentros sísmicos. No obstante, estos datos deberían ser utilizados para establecer las velocidades cercanas a la superficie o para probar el rendimiento del modelo 1-D mínimo resultante en el caso de contar con localizaciones de hipocentros superficiales. El objetivo de este método de ensayo y error es establecer geometrías razonables del modelo cortical y los correspondientes intervalos para los parámetros de velocidad y los retardos para cada estación. Cuando la ubicación de los sismos, los retardos de las estaciones y los valores de velocidad no varíen significativamente, los valores RMS totales a lo largo de todas las inversiones deben mostrar una reducción significativa con respecto a las primeras rutinas. Finalmente, el cálculo del modelo de velocidad 1-D y los retardos calculados en cada una de las estaciones deben tener su correspondencia desde el punto de vista de la geología. Por ejemplo, las estaciones con residuos negativos de tiempo deben estar en áreas locales de alta velocidad con respecto a la estación de referencia. Si se cumplen todos estos requisitos, el resultado podría ser una actualización exitosa del modelo 1-D.

Relocalización y selección final de Eventos

Para tener un resultado final de nuestro modelo, hay que volver a relocalizar todos los eventos utilizando la versión actualizada de un modelo 1-D con los residuos de las estaciones obtenidos. Las nuevas localizaciones pueden ser re-calculadas con las siguientes rutinas: HYPO71 [Lee y Lahr, 1975], HYPOINVERSE [Klein, 1978], HYPOELLIPSE [Lahr, 1980] o con VELEST, esto último se puede llevar a cabo fijando tanto los parámetros de las estaciones, como el modelo de velocidad (con el número 999). En términos generales, podemos repetir todo el proceso, pero amortiguando en 0,01 los hipocentros; en 0,1 el retado de las estaciones, y en 1,0 el modelo de velocidad. El objetivo de este paso es calcular el modelo 1-D (parámetros de velocidad y los residuos de las estaciones) para minimizar los errores totales dados por una geometría casi fija de velocidad, dado por el valor 1. Se recomienda probar la estabilidad del resultado, desplazando sistemáticamente y al azar, tanto los hipocentros como los parámetros de velocidad.

Datos sismológicos del CVPCC

Este trabajo se llevo a cabo con la sismicidad histórica registrada por la Red Nacional de Vigilancia Volcánica RNVV. De un total de 1750 sismos localizados durante el año 2011-2013, se seleccionaron 425 sismos, los cuales contaron con una buena localización, es decir, cálculos con 8 o más fases y con un azimut < 180º; en síntesis, sismos de calidad B o A que tuvieran una optima distribución de sus localizaciones. Para el caso de la erupción del 2011, la distribución se extendió desde la Caldera Cordillera Nevada hasta el flanco este del volcán Puyehue. La estación que se utilizó como referencia para el programa VELEST fue la estación Puyehue (PHU), y el modelo con el que se comenzó a trabajar fue el 1-D publicado por Bohm et al. (2002) en la zona sur de Chile. Como se sugiere en el manual, solo se trabajaron con menos de 9 iteraciones en cada una de las fases de aproximaciones al modelo final. En el anexo se adjuntaron los parámetros de entrada del programa y algunas observaciones que el usuario debe tener presente al momento de ejecutar el programa. Si bien todas las estaciones poseen un importante efecto topográfico, se trabajo con una referencia de alturas promedio para el CVCC de 1,5 km por sobre el nivel del mar. Como archivos de entrada se utilizó el modelo de velocidad propuesto por Bohm et al., 2002. La primera iteración (cero) efectuada por el VELEST, arrojó un RMS≈ 32, evidenciando un fuerte contraste entre los retardos utilizados para cada estación, la localización de las estaciones y el modelo de velocidad propuesto. Tal y como se sugiere en el manual, las iteraciones fueron realizadas con todos los grados de libertad tanto para el modelo (0,1), como para el retardo de las estaciones (0,1) y la ubicación de los hipocentros (0,01). Luego de realizar varias pruebas incrementado y disminuyendo tanto las velocidades como los espesores de las capas (sobre todo de los primeros 3 horizontes), los valores de RMS para cada iteración fueron disminuyendo progresivamente, destacando que solo se efectuaban no más de siete iteraciones por fase. Si los valores eran favorables, se tomaban las nuevas localizaciones y el nuevo modelo (ya más ajustado) y se volvía a iterar en una segunda fase (de 5 a 7 iteraciones), esto con el objeto de lograr disminuir aun más el valor del RMS.

Resultados

Luego de efectuar muchas pruebas tanto en el modelo como en los grados de libertad que ejecutan los parámetro de entrada del programa VELEST, se llego a un RMS mínimo de

0,18; arrojando además de un nuevo modelo de velocidades, los retardos (delay) asociados a cada una de las estaciones que componen la red. La mayoría de los retardos mostraron valores positivos que no superaron los 0,6 segundo. Desde el punto de vista geológico, cada uno de estos retardos calculados señalan zonas de menor velocidad entre la estación de referencia (PHUZ) y sus pares, no obstante, las estaciones localizadas en el flanco oeste del volcán (Futangue FUTZ, Rucatayo TAYZ y Lican LICZ) poseen los valores más altos de retardo, destacando el hecho de que todas ellas se localizan alrededor de la Caldera Cordillera Nevada, lugar donde se localiza el reservorio principal del complejo volcánico.

Se adjunta el archivo **"velest.cmn"** que controla los parámetros y la ejecución de los archivos adicionales que utiliza el programa VELEST.

******* CONTROL-FILE FOR PROGRAM V E L E S T (28-SEPT1993) *******

*** (all lines starting with * are ignored!)

*** (where no filename is specified,

***   leave the line BLANK. Do NOT delete!)

*** next line contains a title (printed on output):

CAULLE VOLCANO. INITIAL 1-D MODEL AUG/2013

***   starting model based on dbasualto 2013

*** olat   olon   icoordsystem   zshift   itrial ztrial   ised

   -40.5005 72.1956   0   0.0   0   0.00   0

*** neqs   nshot   rotate

   425   0   0.0

*** isingle   iresolcalc

    0   0

*** dmax   itopo   zmin   veladj   zadj   lowveloclay

   100.0   0   0.0   0.2   5.0   0

*** nsp   swtfac   vpvs   nmod

    2   0.50   1.78   1

*** othet xythet zthet   vthet stathet

    0.01   0.01   0.01   1.0   0.1

*** nsinv   nshcor   nshfix   iuseelev   iusestacorr

    1   0   0   1   1

*** iturbo   icnvout   istaout   ismpout

```
    1       1       1       1
*** irayout  idrvout  ialeout  idspout  irflout  irfrout  iresout
    0       0       0       0       0       0       0
*** delmin  ittmax  invertratio
   0.01      7       2
*** Modelfile:
caulle.mod
*** Stationfile:
caulle.sta
```

Observaciones para el lector:

El programa posee varios archivos de entrada como es la localización de las estaciones (*.*.STA), el modelo de velocidad inicial (*.*.MOD), los parámetros para ejecutar el Velest (velest.cmn) y los datos sismológicos de las localizaciones (*.*.CNV), no obstante, cada uno de estos archivos posee un formato específico. Favor poner atención en cada uno de los archivos mencionados, _no debe quedar ninguna línea adicional al final de cada uno de los archivos de entrada, líneas vacías o espacios,_ ya que en ocasiones, esto puede traer problemas al momento de ejecutar el sofrware Velest con errores que no están especificados en el manual.
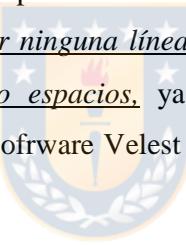
Distribución Temporal Del Parámetro b En El Complejo Volcanica Puyehue Cordon Caulle CVPCC

El método utilizado para calcular la "Distribución de la Frecuencia de Magnitudes" (DFM) fue propuesto por Ishimoto & Lida, (1939) y Gutemberg & Richter, (1944),

$$log_{10}N = a - bM \qquad (1)$$

donde N es el número acumulativo de sismos con magnitudes mayores o iguales a M, *a* y *b* son constantes. El parámetro "*a*" representa la actividad en un volumen específico y "*b*" el decaimiento del tamaño de los sismos en ese mismo volumen. Wiemer y Wyss. (2000) sugieren realizar una estimación rigurosa de la homogeneidad espacial y temporal de la magnitud de completitud (M_C) antes de procede con el cálculo del *valor de b*, ya que la elección de magnitudes menores puede distorsionar la DFM cuya distribución es asumida como una ley de potencia (ecuación 1). M_C se define como la magnitud por encima de la cual la red es capaza de detectar actividad en el espacio-tiempo. La M_C puede cambiar en el tiempo, ya que la instalación de nuevas estaciones puede generar mayor sensibilidad en la red, lo que se traduce en una disminución del valor de la M_C. Una buena aproximación del M_C se puede realizar construyendo un histograma del número de sismos versus la magnitud. En este gráfico, la M_C quedará definida por sobre el mayor número de sismos asociados con una determinada *Ml*.

El valor de b es inversamente proporcional a la magnitud media *M*, definiendo así una magnitud mínima $M_{min}= M_C$ para una muestra dada. De esta forma, se calcularon los *valores de b* mediante la "Máxima Probabilidad" usando la siguiente ecuación obtenida de *Utsu*, (1965); *Aki*, (1965); Bender (1983):

$$b = \frac{1}{M - M_{min}} \log e \qquad (2)$$

De esta forma se cumple que $M \geq M_C$.

El valor de b se calcula a partir de la pendiente de una recta, la que se construye mediante la aproximación de una línea recta sobre la curva de acumulación de la frecuencia de magnitudes de los sismos localizados. El cálculo de b tanto temporal como espacial fue propuesto por Wiemer, (1996, 1997, 1998), en el cual se mapea la distribución temporal o espacial de *b*, este último mapeado tanto en planta como en profundidad, utilizando un

número de sismos (Nº) predeterminado (50<Nº<300, normalmente=100-150). La totalidad de los sismos son grillados en un reticulado espacial cuyas dimensiones dependerán del número de sismos y del área de la zona de estudio. Es posible también realizar un grillado tomando cilindros con un radio y profundidad determinados, pero el sólido utilizado (esfera, cilindro o cubo) para calcular el valor de b dependerá del método que el usuario utilice. Finalmente, este tipo de análisis de la sismicidad nos permitirá obtener imágenes del valor b en función del tiempo y del espacio (Wiemer et al., 1998).

Variación temporal del *b-value* en el CVPCC

En el caso del CVPCC, se seleccionaron los sismos mejor localizados (calidades B y C, con errores mínimos en la horizontal menores a 0,75 Km y en la vertical de 1,5 Km), registrados durante enero 2011 a diciembre de 2013. Se comenzó por relocalizar todos los sismos trabajados por el grupo de analistas, haciendo hincapié en cada una de las lecturas "P" y "S", sus respectivos pesos y polaridades. Para el cálculo de la *Ml* se utilizaron las estaciones Ranco, Pocura y Puyehue; trabajando con un promedio de las lecturas de las componentes horizontales para cada una de estas estaciones. Para el cálculo temporal del valor de *b*, se trabajó con un total de 1750 sismos, todos localizados en el área del CVPCC, los cuales corresponden a las etapas pre, sin y post-eruptiva del proceso volcánico. Con el objeto de ver como varía el valor de b con respecto al número de sismos y eventualmente a su magnitud de completitud (M_C).

En relación al cálculo del valor de b temporal finalmente se escogió la ventana de 125 eventos con un overlap del 75% y una M_C que actuara de forma fija e igual 1,6 respectivamente (Figura M1). Dicha figura representa el análisis de las magnitudes, esto con el fin de determinar la sensibilidad de la red sísmica del CVPCC.
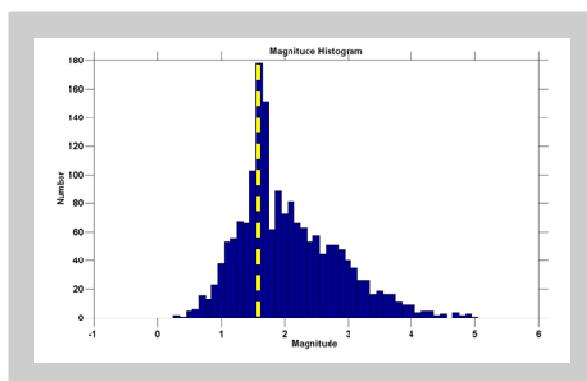
Figura M1. Histograma de las *Ml* registradas por la red de estaciones del CVPCC desde enero de 2011 a diciembre de 2013,1750 sismos, se destaca (barra amarilla) el mayor número de sismos (178) con una M_C=1,6. Fuente: elaboración propia.

En relación a los resultados obtenidos analizando las variaciones temporales del valor de b (Figuras M2), se pudo observar que días antes de la erupción, el valor de b mostró un abrupto descenso, rasgo que predominó independientemente de la base de datos utilizada, o de los valores seleccionados para el cálculo de b; evidenciando que dicha variación está relacionada con el proceso volcánico, y más específicamente, con la inestabilidad generada por el ascenso de magmas y sus importantes magnitudes. De igual forma, en la figura M3 (derecha), podemos observar los errores asociados a cada una de las ventanas seleccionadas para calcular el valor de b. Las metodologías utilizadas para calcular dichos errores (estimación de la incertidumbre), fueron las propuestas por Aki. (1965) [ec. 3, barras verticales celestes] y las de Shia & Bolt. (1982) [ec. 4, barras verticales fucsias], esta última sugerida para el cálculo espacial del valor de b.

$$\hat{\sigma}_{b^*} = \frac{\hat{b}^*}{\sqrt{N}} \qquad (3) \qquad \hat{\sigma}_{b^*}^{(SB)} = 2.30\hat{b}^{*2}\sqrt{\frac{\sum_{i=1}^{N}\left(M_i - \hat{\mu}\right)^2}{N(N-1)}} \qquad (4)$$

Donde N es el número de sismos y μ es el promedio del muestreo de las magnitudes.
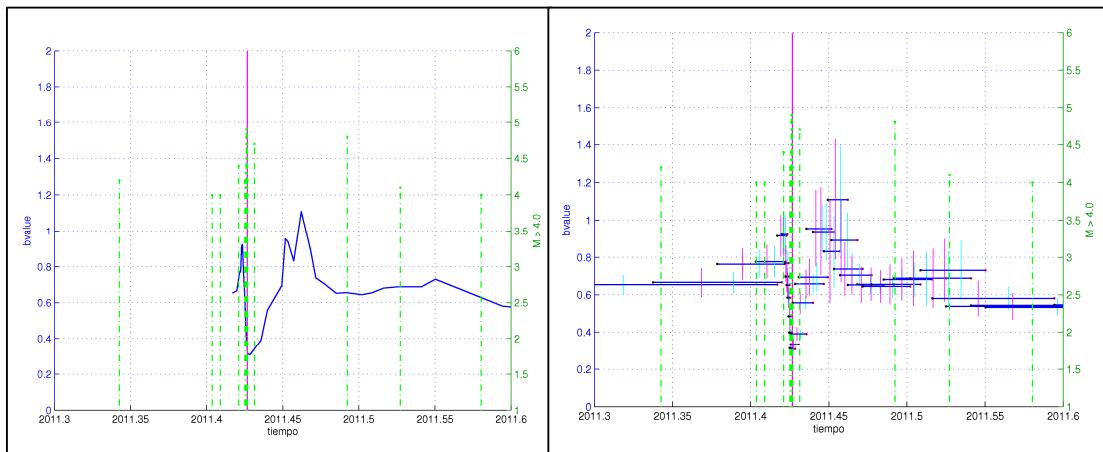
Figura M2. Izquierda, valor de b temporal para la serie de tiempo Normal de 1750 sismos localizados por la RNVV durante el año 2011. Derecha, valor de b indicando además la extensión de cada una de las ventanas temporales de 125 sismos (líneas azules) y los errores calculados para cada una de estas ventanas tanto por el método de Aki. (1965) barra celeste, como por el de Shia & Bolt. (1982), barras purpuras. En verde se destacan los sismos mayores a 4 *Ml* y con la línea gruesa de color purpura, el origen de la erupción (04 de junio de 2011). Fuente: elaboración propia.

Luego de analizar muchas combinaciones tanto de overlap (25, 50 o 75%) como del número de sismos (50-75-100-125-150) para construir el b-value temporal, se logró observar que "como rasgo general", las grandes variaciones del valor de b se mantienen independientemente de los valores utilizados. Finalmente, se escogió la ventana de 125 eventos con un overlap del 75% y una M_C que actuara de forma fija e igual 1,6.

# Inversiones de ondas sísmicas (ISOLA software)

El proceso de inversión de onda sísmica tiene como finalidad encontrar una aproximación y reconstrucción de la fuente sísmica. Durante el proceso, se deben considerar tanto las propiedades físicas del medio (elasticidad de la corteza, velocidad, densidad, coeficientes de atenuación), como la respuesta instrumental, para lograr reconstruir la onda sísmica y su propagación. Debido a la gran cantidad de información se decidió invertir la actividad sísmica más relevante (*Ml*>3,0) y calcular el tensor de momento actuante para la actividad más representativa de la crisis volcánica. Son varios los trabajos avocados a determinar el tensor momento para sismos de carácter tectónicos (Sokos et al., 2012; Hicks & Rietbrock 2015); no obstante, trabajos relacionados con soluciones isotrópicas (ISO, conocidas también como volumétricas) o de tipo CLVD (dipolo de vector lineal compensado) asociados con sistemas volcánicos activos son poco conocidos (Křížová et al., 2013), donde las soluciones propuestas sugieren una combinación de fuentes CLVD+ISO= No Doble Cupla (NDC). Es evidente que en zonas volcánicas es posible encontrar mecanismos puros de tipo Doble Cupla (DC), pero por lo general aparecen en grupos de sismos tipo VT (enjambres), donde no existe un evento principal que luego gatille replicas (Mogi 1963). No obstante, para el caso particular del CVPCC, los sismos NDC (HB/VLP) en un comienzo aparecieron de forma aislada, sin que estuvieran precedidos por importantes sismos de tipo VT o enjambres. Los sismos que posteriormente presentarían mecanismos combinados (CLVD+ISO=NDC) se caracterizaros por presentar un predominio absoluto de polaridades impulsivas compresivas, una alta frecuencia en el comienzo del evento, para luego registrar frecuencias por debajo de 1 Hz. Considerando la participación de fluidos hidrotermales y/o magmáticos asociados a mecanismos NDC en su fuente, se calculó el tensor momento (TM) sísmico, utilizando inversiones de ondas. Las inversiones calculadas se realizaron tanto para eventos de tipo VLP-HB como para sismos tipo VT. Las inversiones se llevaron a cabo utilizando ondas de cuerpo (fue corroborada su existencia con polarización de ondas) y un filtro< 0,25 Hz. El software utilizado para las inversiones fue "ISOLA" versión 2013 (Sokos y Zahradnik 2008). Este programa está basado en iteraciones de deconvolución punto-fuente para ondas de cuerpo. El cálculo de las funciones de Green asociado al campo de onda total generado producto del comportamiento elástico de la corteza, se realizó siguiendo la metodología propuesta por Bouchon (1981). El tensor momento es calculado con el método de mínimos cuadrados. El tiempo de origen y la posición espacial de la fuente puntual (centroide) se buscaron en el entorno al hipocentro relocalizado por VELEST. Luego de ingresar la

respuesta instrumental de las estaciones y definir el modelo de velocidad local (calculado mediante VELEST), se procedió a integrar la señal de velocidad ya que el programa trabaja con desplazamientos y no con velocidades. De igual forma, y para corroborar que la relación señal/ruido estuviera por sobre los parámetros necesarios para invertir las señales, se graficaron en el dominio de la frecuencia y del tiempo, buscando la frecuencia esquina y con ello el predominio de las bajas frecuencias, evitando que el registro se distorsiona producto del bajo coeficiente señal/ruido. Finalmente, para el cálculo de las inversiones se utilizó la aproximación a la solución: "único punto de origen", iterando cada 1 km desde 0,25 a 12,25 km de profundidad y se utilizó la inversión de tipo "full wave inversion" (Full MT) para obtener tanto el TM como el mecanismo focal asociado a esta fuente sísmica.

Existe un consenso sobre el hecho de obtener una inversión correcta. Para ello, una red debe tener una distribución espacial adecuada, mejores soluciones hipocentral, un modelo de velocidad preciso y una diferencia adecuada en la relación señal-ruido (Sokos y Zahradnik, 2008). En el caso de la actividad sísmica de CVPCC, se trabajó con fuentes sísmicas cuyas *Ml*> 3,0. Sin embargo, para corroborar que las soluciones obtenidas fueran estables (sugiriendo una solución única) debido a los altos porcentaje volumétricos de tipo NDC, se decidió poner a prueba el sismo más representativo y de mayor magnitud registrado durante el período pre-eruptivo para probar la componente volumétrica (VLP, 27 de abril de 2011). Para verificar la estabilidad de la fuente y la posible variación de las soluciones, se insertaron diferentes porcentajes de ruidos aleatorios en el sismograma (Vavryčuk 2007). Para esto se construyó una señal de ruido con frecuencias aleatorias por debajo de 1.0 Hz, utilizando amplitudes que alcanzan el 10, 20 y 30% de la amplitud predominantes del sismo VLP (Fig. M3). Finalmente, cada ruido obtenido se agregó (sumo) a la señal VLP previamente seleccionada con el fin de verificar la estabilidad de las soluciones de las inversión con los diferentes porcentages de ruido incoprporados.

Figura M3.- Solución obtenida de la inversión generada del sismo VLP registrado el 27 de abril de 2011. Color rojo el sismograma sintético y en negro el sismo registrado por la RNVV. Las frecuencias utilizadas fueron de 0.03 a 0.2 Hz. Los números azules representan la reducción de varianza, valor que cuantifica el ajuste entre ambas señales. Las amplitudes de cada sismo se destacan en metros. Si bien las soluciones no tuvieron la misma calidad que las calculadas en la figura S5, la solución obtenida continúa sugiriendo un predominio de CLVD+ISO. Fuente: elaboración propia.

Finalmente, si el lector requiere más detalles de esta metodología, se sugiere bajar y leer el manual del software ISOLA en:

http://seismo.geology.upatras.gr/isola/manual.html

Referencias

Adams, N. K., B. F. Houghton, and S. A. Fagents (2006). The transition from explosive to effusive eruption regime: The example of the 1912 Novarupta eruption, Alaska, Geol. Soc. Am. Bull., 118, 620–634.

Aki, K., (1965). Maximum likelihood estimate of b in the formula log N=a–bM and its confidence limits. Bull. Earthq. Res. Inst. Univ. Tokyo 43, 237–239.

Aki, K., M. Fehler, and S. Das (1977). Source mechanism of volcanic tremor: Fluid-driven crack models and their application to the 1963 Kīlauea eruptions, J. Volcanol. Geotherm. Res., 2, 259–287.

Aki, K., and R. Koyanagi (1981). Deep volcanic tremor and magma ascent mechanism under Kīlauea, Hawaii, J. Geophys. Res., 86, 7095–7109, doi:10.1029/JB086iB08p07095.

Aki, K., and Richards, P., (1980). Quantitaive Seismology, Theory and Methods, 932 pp. San Francisco, CA: W H Freeman.

Aki, K., (1984). Evidence for magma intrusion during the Mammoth Lakes earthquakes of May 1980 and implication of the absence of volcanic (Harmonic) Tremor. Journal of Geophysical Research 89 (B9), 7689–7696.

Allan, J. F., and T. Simkin (2000). Fernandina volcano's evolved, well mixed basalts: Mineralogical and petrological constraints on the nature of the Galápagos plume, J. Geophys. Res., 105, 6017–6041, doi:10.1029/1999JB900417.

Alloway, B.V., Pearce, N.J.G., Villarosa, G., Outes, V. & Moreno, P.I. (2015). Multiple melt bodies fed the AD 2011 eruption of Puyehue-Cordón Caulle, Chile, *Scientific reports*, 5, 17589.

Alparone, S., D. Andronico, L. Lodato, and T. Sgroi (2003). Relationship between tremor and volcanic activity during the Southeast Crater eruption on Mount Etna in early 2000, J. Geophys. Res., 108(B5), 2241, doi:10.1029/2002JB001866.

Altamimi, Z., Collilieux, X. & Métivier, L., (2011). ITRF2008: an improvement solution of the International Terrestrial Reference Frame, *Journal of Geodesy*, 85, 457-473.

Anderson, S. W., and J. H. Fink (1990). The development and distribution of lava textures at the Mount St. Helens dome, in Lava Flows and Domes: Emplacement Mechanisms and Hazard Implications, IAVCEI Proc. in Volcanol. Ser., vol. 2, edited by J. H. Fink, pp. 25–46, Springer, Berlin.

Andronico, Branca, D., Calvari, S., Burton, S., Caltabiano, M., Corsaro, R., Del Carlo, P., Garfí G., Lodato, L., Miraglia, L., Muré, F., Neri, M. Pecora, E., Pompilio, M., Salerno, G., Spampinato L. (2005). A multi-disciplinary study of the 2002–03 Etna eruption: Insights into a complex plumbing system, Bull. Volcanol. 67, 314–330.

Arculus, R. J., R. W. Johnson, B. W. Chappell, C. O. McKee, and H. Sakai (1983). Ophiolite-contaminated andesites, trachybasalts, and cognate inclusions of Mount Lamington, Papua New Guinea: Anhydrite-amphibole-bearing lavas and the 1951 cumulodome, J. Volcanol. Geotherm. Res., 18, 215–247.

ASTER GDEM Validation Team: Tachikawa, T., M. Kaku, A. Iwasaki, D. Gesch, M. Oimoen, Z. Zhang, J. Danielson, T. Krieger, B. Curtis, J. Hasse M. Abrams, R. Cripeen, C. Carabajal, and D. Meyer (2011), ASTER Global Digital Elevation Model Version 2 – Summary of validation results.

Bailey, J. E., A. J. L. Harris, J. Dehn, S. Calvari, M. Burton, and S. K. Rowland (2006). The changing morphology of an open lava channel on Mt. Etna, Bull. Volcanol., 52, 113–117.
Barrientos, S., y Ward, S., 1990. The 1960 Chile earthquake: inversion for slip distribution from surface deformation. Geophys. J. Int.103, pág 589-598.

Bender, B., (1983). Maximum likelihood estimation of b values for magnitude grouped data. Bull. Seismol. Soc. Am. 73, 831–851.

Barrientos, S.E. & Ward, S.N., (1990). The 1960 Chile earthquake: inversion for slip distribution from surface deformation, *Geophysical Journal International*, 103(3), 589-598.

Basualto, D.; Cardona, C.; Franco, L.; Gil, F.; Valderrama, A.; Hernández, E.; (2012). Mecanismos de intrusión relacionados con la erupción del complejo volcánico Cordón Caulle – Chile, Junio 4 de 2011. Congreso Geológico Chileno, No. 13, Actas X: 522-524. Antofagasta.

Battaglia, J., K. Aki, and T. Staudacher (2005). Location of tremor sources and estimation of lava output using tremor source amplitude on the Piton de la Fournaise volcano: 2 Estimation of lava output, J. Volcanol. Geotherm. Res., 147, 291–308.

Beauducel, F., Briole, P. & Froger, J.-L., (2000). Volcano-wide fringes in ERS synthetic aperture radar interferograms of Etna (1992-1998): Deformation or tropospheric effect ? *Journal of Geophysical Research*,105(B7), 16391–16402, doi:10.1029/2000JB900095.

Bedford, J., Moreno, M., Báez, J.C., Lange, D., Tilmann, F., Rosenau, M., Heidbach, O., Oncken, O., Bartsch, M., Rietbrock, A., Tassara, A., Bevis, M. & Vigny, M., (2013). A high-resolution, time-variable afterslip model for the 2010 Maule Mw=8.8, Chile megathrust earthquake, *Earth and Planetary Science Letters*, 383, 26-36.

Behncke, B., and M. Neri (2003). The July–August 2001 eruption of Mt. Etna (Sicily), Bull. Volcanol., 65, 461–476.

Bellier, O., Se´brier, M., (1994). Relationship between tectonism and volcanism along the Great Sumatran Fault deduced by SPOT image analyses. Tectonophysics 233, 215– 231.

Bertin, D., Lara, L.E., Basualto, D., Amigo, Á., Cardona, C. Franco, L., Gil, F.& Lazo, J., (2015). High effusion rates of the Cordón Caulle 2011–2012 eruption (Southern Andes) and their relation with the quasi-harmonic tremor, *Geophysical Research Letters*, doi:10.1002/2015GL064624.

Bertin, D.; Amigo, A.; Lara, L.E.; Orozco, G.; Silva, C. (2012). Erupción del Cordón Caulle 2011–2012: evolución de la fase efusiva. Congreso Geológico Chileno, No. 13, Actas X: 539-541. Antofagasta, Chile.

Bevis, M., Kendrick, E., Cser, A. & Smalley, R., (2004). Geodetic measurement of the local elastic response to the changing mass of water in Lago Laja, Chile,*Physics of the Earth and Planetary Interiors*, 141(2), 71-78.

Biggs, J., Ebmeier, S. K., Aspinall, W. P., Lu, Z., Pritchard, M. E., Sparks, R. S. J., & Mather, T. A. (2014). Global link between deformation and volcanic eruption quantified by satellite imagery. Nature Communications, 5, 3471.

Biggs, J., Mothes, P., Ruiz, M., Amelung, F., Dixon, T.H., Baker, S. & Hong, S.H., (2010). Stratovolcano growth by co-eruptive intrusion: The 2008 eruption of Tungurahua Ecuador, *Geophysical Research Letters*, 37(21), *L21302, doi:10.1029/2010GL044942*.

Bignami, C., Corradini, S., Merucci, L., de Michele, M., Raucoules, D., De Astis, G., Stramondo, S. & Piedra, J., (2014). Multisensor Satellite Monitoring of the 2011 Puyehue-Cordon Caulle Eruption,*IEEE Journal of Selected Topics in Applied Earth Observations and Remote Sensing*, 7(7), 2786-2796.

Birch, F., (1960). The velocity of compressional waves in rocks to 10 kilobars: 1. *Journal of Geophysical Research*, 65(4), 1083-1102.

Bjornsson, A., Hersir, G.P., (1986). The Hengill hightemperature area, S.W. Iceland: regional geophysical survey, Geotherm. Resour. Counc. Trans., 10, 205–210.

Bohm M.; Lüth S.; Echtler H.; Asch G.; Bataille K.; Bruhn C.; Rietbrock A.; Wigger P. (2002). The Southern Andes between 36º and 40º S latitude: seismicity and average seismic velocities. Tectonophysics 356, 275– 289.

Bonali, F.L., Tibaldi, A., Corazzato, C., Tormey, D.R.& Lara, L.E., (2013). Quantifying the effect of large earthquakes in promoting eruptions due to stress changes on magma pathway: the Chile case,*Tectonophysics*, 583, 54-67.

Bos, M.S., Bastos, L. & Fernandes, R.M.S., (2010). The influence of seasonal signals on the estimation of the tectonic motion in short continuous GPS time-series,*Journal of Geodynamics*, 49(3), 205-209.

Bouchon, M., (1981). A simple method to calculate Green's functions for elastic layered media: Bull. Seism. Soc. Am., 71, 959-971.

Brodsky EE, Sturtevant B, Kanamori H. (1998). Volcanoes, earthquakes and rectified diffusion.J. Geophys. Res. 103:23827–38.

Burton, M. R., et al. (2005). Etna 2004–2005: An archetype for geodynamically-controlled effusive eruptions, Geophys. Res. Lett., 32, L09303 doi:10.1029/2005GL022527. California. Journal of Geophysical Research 90 (B13), 11,155–11,169.

Calo, M. (2009). Tomography of subduction zones using regional earthquakes: methodological developments and application to the Ionian slab (Doctoral dissertation, Strasbourg).

Calvari, S., L. Spampinato, L. Lodato, A. J. L. Harris, M. R. Patrick, J. Dehn, M. R. Burton, and D. Andronico (2005). Chronology and complex volcanic processes during the 2002–2003 flank eruption at Stromboli volcano (Italy) reconstructed from direct observations and surveys with a hand-held thermal camera, J. Geophys. Res., 110, B02201, doi:10.1029/2004JB003129.

Calvari, S., M. Neri, and H. Pinkerton (2003). Effusion rate estimations during the 1999 summit eruption on Mount Etna, and growth of two distinct lava flows, J. Volcanol. Geotherm. Res., 119, 107–123.

Campos, A., Moreno, H., Muñoz, J., Antinao, J., Clayton, J., Martín, M., (1998). Mapa Geológico del Área de Futrono (1 : 1.000.000). Servicio Nacional de Geología Minería, CHILE.

Cannata, A., G. Di Gracia, P. Montalvo, F. Ferrari, G. Nunnari, D. Patanè, and E. Privitera (2010). New insights into banded tremor from the 2008–2009 Mount Etna eruption, J. Geophys. Res., 115, B12318, doi:10.1029/2009JB007.

Cardona, C., D. Basualto, L. Franco, F. Gil, and A. Valderrama (2012). Actividad sísmica relacionada con la erupción del Complejo Volcánico Cordón Caulle – Chile, Junio 4 de 2011, Cong. Geol. Chileno, 13, 542–547.
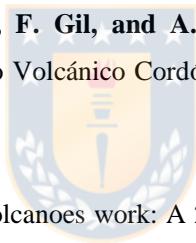
Cashman K., Sparks S., (2013). How volcanoes work: A 25 year perspective. Geological Society of America Bulletin 2013;125, no.5-6;664-690 doi: 10.1130/B30720.1

Castro JM, Dingwell DB, 2009. Rapid ascent of rhyolite magma at Chaitén volcano, Chile. Nature 461:780–784.

Castro, J. M., C. I. Schipper, S. P. Mueller, A. S. Militzer, A. Amigo, C. Silva Parejas, and D. Jacob (2013). Storage and eruptions of near-liquidus rhyolite magma at Cordón Caulle, Chile, Bull. Volcanol., 75, 702–719.

Castro, J. M., I. N. Bindeman, H. Tuffen, and C. I. Schipper (2014). Explosive origin of silicic lava: Textural and δD-H2O evidence for pyroclastic degassing during rhyolite effusion, Earth Planet. Sci. Lett., 405,52–61.

Cayol, V. & Cornet, F.H., (1998). Effects of topography on the interpretation of the deformation field of prominent volcanoes - Application to Etna, *Geophysical Research Letters*, 25, 1979–1982.

Cembrano, J., &Lara, L.E., (2009). The link between volcanism and tectonics in the southern volcanic zone of the Chilean Andes: a review, *Tectonophysics*, 471(1), 96-113.

Cembrano, J., Hervé, F., Lavenu, A., (1996). The Liquiñe–Ofqui fault: a long-lived intra-arc fault system in southern Chile. Tectonophysics 259, 55–66.

Cembrano, J., Lavenu, A., Reynolds, P., Arancibia, G., López, G., Sanhueza, A., (2002). Late Cenozoic transpressional ductile deformation north of the Nazca–South America–Antartica triple junction. Tectonophysics 354, 289– 314.

Cembrano, J., Moreno, H., (1994). Geometría y naturaleza contrastante del volcanismo cuaternario entre los 38°S y 46°S: ¿Dominios compresionales y tensionales en un régimen transcurrente? Congreso Geológico Chileno No. 7, Actas, vol. 1, pp. 240–244.

Cembrano, J., Schermer, E., Lavenu, A., Sanhueza, A., (2000). Contrasting nature of deformation along an intra-arc shear zone, the Liquin˜e–Ofqui fault zone, Southern Chilean Andes. Tectonophysics 319, 129– 149.

Chouet, B. (1981). Ground motion in the near field of a fluid-driven crack and its interpretation in the study of volcanic tremor, J. Geophys. Res., 86, 5985–6016, doi:10.1029/JB086iB07p05985.

Chouet, B. (1988). Excitation of a fluid-driven crack: Radiation properties and implication for the source of long-period events and harmonic tremor, J. Geophys. Res., 93, 4375–4400, doi:10.1029/JB093iB05p04375.

Chouet, B., (2003). Volcano Seismology, *Pure appl. Geophys.* 160, 739–788.

Coombs, M. L., J. C. Eichelberger, and M. J. Rutherford (2000). Magma storage and mixing conditions for the 1953–1974 eruptions of Southwest Trident volcano, Katmai National Park, Alaska, Contrib. Mineral. Petrol., 140, 99–118.

Coombs, M. L., K. F. Bull, J.W. Vallance, D. J. Schneider, E. E. Rhoms, R. L. Wessels, and R. G. McGimsey (2010). Timing, distribution, and volume of proximal products of the 2006 eruption of Augustine Volcano, in The 2006 Eruption of Augustine Volcano, Prof. Pap., vol. 1769, edited by J. A. Power, M. L. Coombs, and J. T. Freymueller, pp. 145–186, U.S. Geol. Surv., Alaska.

Coombs, M. L., T. W. Sisson, H. A. Bleick, S. M. Henton, C. J. Nye, A. L. Payne, C. E. Cameron, J. F. Larsen, K. L. Wallace, and K. F. Bull (2013). Andesites of the 2009 eruption of Redoubt Volcano, Alaska, J. Volcanol. Geotherm. Res., 259, 349–372.

Crosson, R.S., (1976). Crustal structure modelling of earthquake data, 1, Simultaneous least squares estimation of hypocenter and velocity parameters, J. Geophys. Res., 81, 3036-3046.

Dach, R., Hugentobler, U., Fridez, P.& Meindl, M., (2007). *Bernese GPS Software Version 5.0*, Astronomical Institute, University of Bern.

Degruyter, W., O. Bellier, A. Burgisser, and M. Manga (2012). The effects of outgassing on the transition between effusive and explosive silicic eruptions, Earth Planet. Sci. Lett., 349–350, 161–170.

Delgado F., Pritchard M., Basualto D., Lazo J., Córdoba L., Lara L. (2016). Rapid reinflation following the 2011–2012 rhyodacite eruption at CordónCaulle volcano (Southern Andes) imaged by InSAR: Evidence for magma reservoir refill. Geophisical Research Letter, 10.1002/2016GL070066.
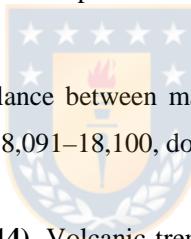
Denlinger, R. P. (1997). A dynamic balance between magma supply and eruption rate at Kīlauea Volcano, Hawaii, J. Geophys. Res., 102, 18,091–18,100, doi:10.1029/97JB01071.

Denlinger, R. P., and S. C. Moran (2014). Volcanic tremor masks its seismogenic source: Results from a study of noneruptive tremor recorded at Mount St. Helens, Washington, J. Geophys. Res. Solid Earth, 119, 2230–2251, doi:10.1002/2013JB010698.

Devine, J. D., M. D.Murphy, M. J. Rutherford, J. Barclay, R. S. J. Sparks,M. R. Carroll, S. R. Young, and J. E. Gardner (1998). Petrologic evidence for pre-eruptive pressure-temperature conditions, and recent reheating, of andesitic magma erupting at the Soufrière Hills Volcano, Montserrat, W.I, Geophys. Res. Lett., 25, 3669–3672, doi:10.1029/98GL01330.

Dhont, D., Chorowicz, J., Yürür, T., Froger, J.L., Köse, O., Gündogdu, N., (1998). Emplacement of volcanic vents and geodynamics of Central Anatolia, Turkey. J. Volcanol. Geotherm. Res. 62, 207–224.

Diefenbach, A. K., K. F. Bull, R. L. Wessels, and R. G. McGimsey (2012). Photogrammetric monitoring of lava dome growth during the 2009 eruption of Redoubt Volcano, J. Volcanol. Geotherm. Res., 259, 308–316.

Dixon, H.J., Murphy, M.D., Sparks, S.J., Chávez, R., Naranjo, J.A., Dunkley, P.N., Young, S.R., Gilbert, J.S., Pringle, M.R., (1999). The geology of the Nevados de Chillán volcano, Chile. Revista Geológica de Chile 26 (2), 227–253.

Dow, J.M., Neilan, R.E. &Rizos, C., (2009). The International GNSS Service in a changing landscape of Global Navigation Satellite Systems,*Journal of Geodesy*, 83,191-198, doi: 10.1007/s00190-008-0300-3.

Dreger D., Tkalčić1 H., Johnston M., (2000). Dilational Processes Accompanying Earthquakes in the Long Valley Caldera. Science 7 April 2000:Vol. 288 no. 5463 pp. 122-125 DOI: 10.1126/science.288.5463.122.

Dzurisin, D., J. W. Vallance, T. M. Gerlach, S. C. Moran, and S. D. Malone (2005). Mount St. Helens reawakens, Eos Trans. AGU, 86 (3), 25–36.

Eichelberger, J. C., C. R. Carrigan, H. R. Westrich, and R. H. Price (1986). Non-explosive silicic volcanism, Nature, 323, 598–602.
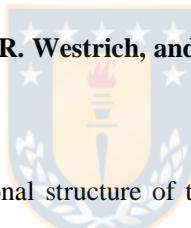
Ellsworth, W.L. (1977). Three-dimensional structure of the crust and mantle beneath the island of Hawaii, Ph.D. thesis, Mass. Inst. of Technol., Cambridge, 1977.

Emmerman, S., Marrett, R., (1990). Why dikes? Geology 18, 231– 233.

Enescu, B., Ito, K. (2003). Temporal and especial variations of seismicity during the 1998 Hida Mountain earthquake swarm, Central Honshu, Japan. Preliminary Result.

Falsaperla, S., H. Langer, and S. Spampinato (1998). Statistical analysis and characteristics of volcanic tremor on Stromboli volcano (Italy), Bull. Volcanol., 60,75–88.

Farias, Cristian& Galvan, Boris & Miller, Stephen. (2017). Numerical simulations (2D) on the influence of pre-existing local structures and seismic source characteristics in earthquake-volcano interactions.Journal of Volcanology and Geothermal Research. 10.1016/j.jvolgeores.2017.07.001.

Farr, T.G., Rosen, P.A., Caro, E., Crippen, R., Duren, R., Hensley, S., Kobrick, M., Paller, M., Rodríguez, E., Roth, L., Seal, D., Shaffer, S., Shimada, J., Umland, J., Werner, M., Oskin, M., Burbank, D., Alsdorf, D., (2007). The Shuttle Radar Topography Mission. *Reviews of Geophysics*, 45(2), RG2004, doi:10.1029/2005RG000183.

Farrell, L., Husen, S., Smith, R., (2009). Earthquake swarm and b-value characterization of the Yellowstone volcano-tectonic system. Journal of Volcanology and Geothermal Research 188 (2009) 260–276.

Fehler, M., and B. Chouet (1982). Operation of a digital seismic network onMount St. Helens volcano and observations of long-period seismic events that originate under the volcano, Geophys. Res. Lett., 9, 1017–1020, doi:10.1029/GL009i009p01017.

Fink, J. H., M. C. Malin, and S. W. Anderson (1990). Intrusive and extrusive growth of the Mount St Helens lava dome, Nature, 348, 435–437.

Fournier T.J., Pritchard M.E., Riddick S.N., (2010). Duration, magnitude, and frecuency of subaerial volcano deformation events: New results from Latin America using InSAR a global synthesis. Geochemistry GeopshysicsGeosystems G3. Volume 11, Number 1, 19 January 2010. Pag 1-29. doi:10.1029/2009GC002558.
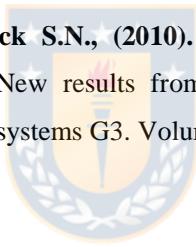
Fréchet, J. (1985). Sismogene`se et doublets sismiques, The`se d'Etat, Universite´ cientifique et Me´dicale de Grenoble, 206.

Froger, J.L., Cayol, V., &Famin, V., (2016). The March–April (2007) Eruptions of Piton de la Fournaise as Recorded by Interferometric Data,in *Active Volcanoes of the Southwest Indian Ocean*, pp. 271-286, ed. Bachelery, P., Lenat, J.-F., Di Muro, A. & Michon, M., Springer Berlin Heidelberg.

Froger, J.L., Fukushima, Y., Briole, P., Staudacher, T., Souriot, T.& Villeneuve, N., (2004). The deformation field of the August 2003 eruption at Piton de la Fournaise, Reunion Island, mapped by ASAR interferometry,*Geophysical Research Letters*, 31(14*), L14601, doi:10.1029/2004GL020479.*

García, F., (2015). Modelo structural del complejo volcánico Puyehue-Cordón Caulle y análisis sísmico del control estructural durante la erupción del 2011, Thesis, Universidad de Concepción, Concepción, Chile.

Gil, F., and B. Chouet (1997). Long-period events, the most characteristic seismicity accompanying the emplacement and extrusion of a lava dome in Galeras Volcano, Colombia, in 1991, J. Volcanol. Geotherm. Res., 77, 121–158.

Goldstein, R.M. & Werner, C.L., (1998). Radar interferogram filtering for geophysical applications,Geophysical Research Letters, 25(21), 4035-4038.

Görgün, E., (2013). Analysis of the b-values before and after the 23 October 2011 Mw 7.2 Van–Erciş, Turkey earthquake.Tectonophysics 603 (2013) 213–221.

Grandin, R., Jacques, E., Nercessian, A., Ayele, A., Doubre, C., Socquet, A., Keir, D., Kassim. M., Lemarchand, A.& King, G.C.P., (2011). Seismicity during lateral dike propagation: Insights from new data in the recent Manda Hararo–Dabbahu rifting episode (Afar, Ethiopia),Geochemistry, Geophysics, Geosystems, 12(4), Q0AB08, doi:10.1029/2010GC003434.

Green, D.N., Neuberg, J., (2006). Waveform classification of volcanic low-frequency earthquake swarms and its implication at Soufrie`re Hills Volcano, Montserrat.Journal of Volcanology.and Geo. Research 153 (2006) 51– 63.
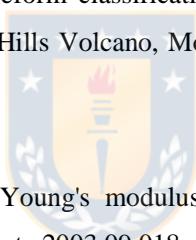
Gudmundsson, A., (2004). Effects of Young's modulus on fault displacement,Comptes Rendus Geoscience, 336(1), 85-92, doi:10.1016/j.crte.2003.09.018.

Guest, J. E., C. R. J. Kilburn, H. Pinkerton, and A. M. Duncan (1987). The evolution of lava flow-fields: Observations of the 1981 and 1983 eruptions of Mount Etna, Sicily, Bull. Volcanol., 49, 527–540.

Gutenberg, B. (1955). The Energy of Earthquakes.The Quarterly Journal of Geological Society of London, Volume CXII. Q.J.G.S. No. 445, 14pp.

Gutenberg, B., Richter, C.F., (1944). Frequency of earthquakes in California. Bull. Seismol. Soc. Am. 34, 185–188.

Hamilton R. M. , (1967). Mean magnitude of an earthquake sequence, Bull. seism. Soc. Am., 57 ,1115–1116.

Hardebeck, H., & Shearer, P., (2003). Using S/P Amplitude Ratios to Constrain the Focal Mechanisms of Small Earthquakes. Bulletin of the Seismological Society of America, Vol. 93, No. 6, pp. 2434–2444, December 2003.

Harper, M.A., (2003). 40Ar/39Ar constraints on the evolution of the Puyehue-Cordón Caulle volcanic complex, Andean southern volcanic zone, Chile [Unpublished M.S. thesis]: University of Wisconsin-Madison.

Harris, A. J. L., and M. Neri (2002). Volumetric observations during paroxysmal eruptions at Mount Etna: Pressurized drainage of a shallow chamber or pulsed supply?, J. Volcanol. Geotherm. Res., 116,79–95.

Harris, A. J. L., J. B. Murray, S. E. Aries, M. A. Davies, L. P. Flynn, M. J. Wooster, R. Wright, and D. A. Rothery (2000). Effusion rate trends at Etna and Krafla and their implications for eruptive mechanisms, J. Volcanol. Geotherm. Res., 102, 237–270.

Harris, A. J. L., J. Dehn, and S. Calvari (2007). Lava effusion rate definition and measurement: A review, Bull. Volcanol., 70(1), 1–22.
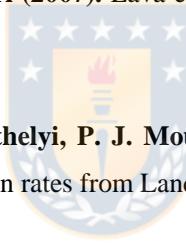
Harris, A. J. L., L. P. Flynn, L. Keszthelyi, P. J. Mouginis-Marks, S. K. Rowland, and J. A. Resing (1998). Calculation of lava effusion rates from Landsat TM Data, Bull. Volcanol., 60,52–71.

Harris, A. J. L., L. P. Flynn, O. Matías, and W. I. Rose (2002). The thermal stealth flows of Santiaguito: Implications for the cooling and emplacement of dacitic lava flows, Geol. Soc. Am. Bull., 114, 533–546.

Harris, A. J. L., W. I. Rose, and L. P. Flynn (2003). Temporal trends in lava dome extrusion at Santiaguito 1922–2000, Bull. Volcanol., 65,77–89.

Heise, W., Caldwell, T.G., Bibby H.M. & Bannister S.C (2008). Three-dimensional modelling of magnetotelluric data from the Rotokawa geothermal field, Taupo Volcanic Zone, New Zealand. Geophys. J. Int. (2008) 173, 740–750.

Hellweg, M. (2000). Physical models for the source of Lascar's harmonic tremor, J. Volcanol. Geotherm. Res., 101, 183–198.

Hicks, S., Rietbrock, A., (2015). Seismic slip on an upper-plate normal fault during a large subduction megathrust rupture. Nature Geoscience, 8, 955–960 (2015) doi:10.1038/ngeo2585.

Hildreth, W., and Fierstein, J., (2012). The Novarupta-Katmai eruption of 1912—largest eruption of the twentieth century; centennial perspectives: U.S. Geological Survey Professional Paper 1791, 259 p, Chapter 13.

Hill, D.& Prejean, S., (2007). Dynamic triggering,in Treatise on Geophysics, pp. 258–288, ed. Kanamori, H., Elsevier, Amsterdam.

Hill, D.P., Pollitz, F., and Newhall, C., (2002). Earthquake-volcano interactions: Physics Today, v. 55, p. 41–47.

Ishikawa, T. (1952). The chemical characteristics of the lavas from Volcano Tarumai, Hokkaido, Japan, J. Faculty Sci. Hokkaido Univ. Ser., 4(8), 107–135.
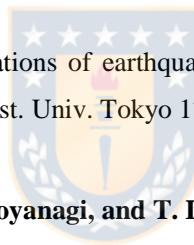
Ishimoto, M., Iida, K., (1939). Observations of earthquakes registered with the microseismograph constructed recently. Bull. Earthq. Res. Inst. Univ. Tokyo 17, 443–478.

Jackson, D. B., D. A. Swanson, R. Y. Koyanagi, and T. L. Wright (1975). The August and October 1968 east rift eruptions of Kīlauea Volcano, Hawaii, U.S. Geol. Surv. Prof. Pap., 890,1–33.

Jacobs, K.& McNutt, S., (2011). Using seismic b-values to interpret seismicity rates and physical processes during the preeruptive earthquake swarm at Augustine Volcano 2005–2006,in: *The 2006 Eruption of Augustine Volcano, Alaska*,pp. 59-83, eds. Power, J.A., Coombs, M.L. & Freymueller, J.T., U.S. Geological Survey Professional Paper 1769.

Jay, J., F. Costa, M. Pritchard, L. E. Lara, B. Singer, and J. Herrin (2014). Locating magma reservoirs using InSAR and petrology before and during the 2011–2012 Cordón Caulle silicic eruption, Earth Planet. Sci. Lett., 395, 254–266.

Jónasson, K. (1994). Rhyolite volcanism in the Krafla central volcano, north-east Iceland, Bull. Volcanol., 56, 516–528.

Julian, B. R. (1994). Volcanic tremor: Nonlinear excitation by fluid flow, J. Geophys. Res., 99, 11,859–11,877, doi:10.1029/93JB03129.

Julian, B.R., Sipkin, S.A., (1985). Earthquake processes in the Long Valley Caldera area, California. Jour. Geo. Res. doi.org/10.1029/JB090iB13p11155.

Kawakatsu, H., T. Ohminato, H. Ito, Y. Kuwahara, T. Kato, K. Tsuruga, S. Honda, and K. Yomogida (1992). Broadband seismic observations at the Sakurajima volcano, Japan, Geophys. Res. Lett., 19, 1959–1962, doi:10.1029/92GL01964.

Kilburn, C. R. J., H. Pinkerton, and L. Wilson (1995). Forecasting the behavior of lava flows, in Monitoring Active Volcanoes, edited by B. McGuire, C. R. J. Kilburn, and J. Murray, pp. 346–368, UCL, London.

Kissling, E., (1988). Geotomography with local earthquake data. *Rev. Geophys.*, 26, 659-698, doi:10.1029/RG026i004p00659.

Kissling, E., Ellsworth, W., Eberhart-Phillips D., Kradolfer, (1994). Initial reference models in local earthquake tomography. Journal of geophysical research, vol. 99, no. B10, october 10, 1994, 19635-19646.

Klein, F.W, (1978). Hypocenter location program HYPOINVERSE, U.S. Geological SurveyOpen-File Report 78-694, 113 pp.

Klotz, J., Khazaradze, G., Angermann, D., Reigber, C., Perdomo, R., Cifuentes, O., (2001). Earthquake cycle dominates contemporary crustal deformation in Central and Southern Andes. Earth and Planetary Science Letters 193, 437–446.

Křížová, D., Zahradník, J.,&Kiratzi, A., (2013). Resolvability of Isotropic Component in Regional Seismic Moment Tensor Inversion. Bull. seism. Soc. Am., 103 (4), 2460–2473.

Lahr, J.C, (1980). HYPOELLIPSE: a computer program for determining local earthquake hypocentral parameters, magnitude and first motion pattern, U.S. Geological Survey Open-FileReport 80-59, 59 pp.

Lahr, J.C., Chouet, B., Stephens, C., Power, J. & Page, R., (1994). Earthquake classification, location, and error analysis in a volcanic environment: implications for the magmatic system of the

1989-1990 eruptions at Redoubt Volcano, Alaska,*Journal of Volcanology and Geothermal Research*, 62, 137-151.

Lahsen, A., (1978). Características Geoquímicas y Origen de Las Aguas Termales de Chillán, Comunicaciones. Dep. de Geol., Univ. De Chile, pp. 35– 48.

Landi, P., L. Francalanci, M. Pompilio, M. Rosi, R. A. Corsaro, C. M. Petrone, I. Nardini, and L. Miraglia (2006). The December 2002–July 2003 effusive event at Stromboli volcano, Italy: Insights into the shallow plumbing system by petrochemical studies, J. Volcanol. Geotherm. Res., 155, 263–284.

Lange, D.; Cembrano, J.; Rietbrock, A.; Haberland, C.; Dahm, V.; Bataille, K. (2008). First seismic record for intra-arc strike-slip tectonics along the Liquiñe-Ofqui fault zone at the obliquely convergent plate margin of the southern Andes.Tectonophysics 455: 14-24.

Lara, L. E., A. Lavenu, J. Cembrano, and C. Rodríguez, (2006 a). Structural controls on volcanism in transversal chains: resheared faults andneotectonics in the Cordón Caulle – Puyehue area (40.5°S), Southern Andes, J. Volcanol. Geotherm. Res., 158,70–86.

Lara, L. E., J. A. Naranjo, and H. Moreno, (2004). Rhyodacitic fissure eruption in Southern Andes (Cordón Caulle; 40.5°S) after the 1960 (Mw: 9.5) Chilean earthquake: A structural interpretation, J. Volcanol. Geotherm. Res., 138, 127–138.

Lara, L.E. & Moreno, H., (2006). Geología del Complejo Volcánico Puyehue-Cordón Caulle, X Región de Los Lagos, Servicio Nacional de Geología y Minería, Carta Geológica de Chile, Serie Geología Básica, 1 mapa escala 1:50.000.

Lara, L.E., Moreno, H., Naranjo, J.A., Matthews, S.& Pérez de Arce, C., (2006 b). Magmatic evolution of the Puyehue–Cordón Caulle volcanic complex (40 S), Southern Andean Volcanic Zone: from shield to unusual rhyolitic fissure volcanism,*Journal of Volcanology and Geothermal Research*, 157(4), 343-366.

Larsen, J. F., C. J. Nye, M. L. Coombs, M. Tilman, P. Izbekov, and C. Cameron (2010). Petrology and geochemistry of the 2006 eruption of Augustine Volcano, in The 2006 Eruption of Augustine Volcano, Prof. Pap., vol. 1769, edited by J. A. Power, M. L. Coombs, and J. T. Freymueller, pp. 335–382, U.S. Geol. Surv., Alaska.

Larsen, J. F., M. G. Śliwiński, C. Nye, C. Cameron, and J. R. Schaefer (2013). The 2008 eruption of Okmok Volcano, Alaska: Petrological and geochemical constraints on the subsurface magma plumbing system, J. Volcanol. Geotherm. Res., 264,85–106.

Lavenu, A.; Cembrano, J. (1999). Compressional- and transpressional-stress pattern for Pliocene and Quaternary brittle deformation in fore-arc and intra-arc zones (Andes of Central and Southern Chile). Journal of Structural Geology 21 (1999) 1669±1691.

Lee, W.H., Bennett, R.E., Meagher, K.L. (1972). A Method of Estimating Magnitude of local earthquakes from signal duration. U.S. Geological Survey Open-File Report, p. 28.

Lipman, P. W., and N. G. Banks (1987). Aa flow dynamics, Mauna Loa 1984, U.S. Geol. Surv. Prof. Pap., 1350, 1527–1567.

Lopez-Escobar, L., Vergara, M., and Frey, F.A., (1981). Petrology and geochemistry of lavas from Antuco Volcano, a basaltic volcano of the Southern Andes (37°25′S): Journal of Volcanology and Geothermal Research, v. 11, p. 329–352, doi: 10.1016/0377-0273(81)90030-5.

Lu, Z., Masterlark, T.& Dzurisin, D., (2005). Interferometric synthetic aperture radar study of Okmok volcano, Alaska, 1992–2003: Magma supply dynamics and postemplacement lava flow deformation,*Journal of Geophysical Research*, 110(B2), B02403, doi: 10.1029/2004JB003148.

Macdonald, G. A., and T. Katsura (1961). Variations in the lava of the 1959 eruption in Kīlauea Iki Pacific, Science, 15(3), 358–369.

Main, I., (1987). A characteristic earthquake model of the seismicity preceding the eruption of Mount St. Helens on 18 May 1980,*Physics of the Earth and Planetary Interiors*, 49, 283–293.

Manga M. and Brodsky E. (2006). Seismic Triggering of Eruptions in the Far Field: Volcanoes and Geysers. Annu. Rev. Earth Planet. Sci 34, 263–291.

Mastin, L.G., Lisowski, M., Roeloffs, E.& Beeler, N., (2009). Improved constraints on the estimated size and volatile content of the Mount St. Helens magma system from the 2004–2008 history of dome growth and deformation,*Geophysical Research Letters*, 36(20), L20304, doi:10.1029/2009GL039863.

Matsumura, S. (1981). Three dimensional expression of seismic particle motion by the trajectory ellipsoid and its application to the seismic data observed in the Kanto district, Japan, J. Phys. Earth, 29, 211-239.

Mazzarini, F., M. T. Pareschi, M. Favalli, I. Isola, S. Tarquini, and E. Boschi (2005). Morphology of basaltic lava channels during the Mt. Etna September 2004 eruption from airborne laser altimeter data, Geophys. Res. Lett., 32, L04305, doi:10.1029/2004GL021815.

McNutt, S. R. (1992). Volcanic tremor, in Encyclopedia of Earth System Science, vol. 4, edited byW. A. Nierenberg, pp. 417–425, Academic Press, San Diego, Calif.

Mogi, K., (1958). Relations between the eruptions of various volcanoes and the deformations of the ground surfaces around them,*Bulletin of the Earthquake Research Institute*, 36, 99-134.

Mogi, K., (1963). Some discussions on aftershocks, foreshocks and earthquake swarms, the fracture of a semi-infinite body caused by an inner stress origin and its relation to the earthquake phenomena, 3. Bull. Earthq. Res. Inst. Univ. Tokyo 41, 615–658.
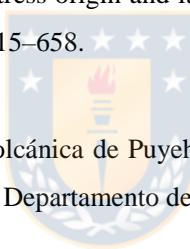
Moreno, H. (1977). Geología del área volcánica de Puyehue- Carrán en los Andes del sur de Chile. Memoria de Título, Universidad de Chile, Departamento de Geología, Santiago. 170 pp.

Munizaga, F., Hervé, F., Drake, R., Pankhurst, R.J., Brook, M., Snelling, N., (1988). Geocronology of the Lake Region of southcentral Chile (39º–42ºS): preliminary results. Journal of South American Earth Sciences 1 (3), 309– 316.

Nakada, S., and Y. Motomura (1999). Petrology of the 1991–1995 eruption at Unzen: Effusion pulsation and groundmass crystallization, J. Volcanol. Geotherm. Res., 89, 173–196.

Nakada, S., H. Shimizu, and K. Ohta (1999). Overview of the 1990–1995 eruption at Unzen, J. Volcanol. Geotherm. Res., 89,1–22.

Nakamura, K., (1977). Volcanoes as possible indicators of tectonic stress orientation: principle and proposal. J. Volcanol. Geotherm. Res. 2, 1 –16.

Nakamura, K., Uyeda, S., (1980). Stress gradient in arc–back arc regions and plate subduction. J. Geophys. Res. 85, 6419–6428.

Odbert, H., Taisne, B.& Gottsmann, J., (2015). Deposit loading and its effect on co-eruptive volcano deformation,*Earth and Planetary Science Letters*, 413, 186-196.

Okada, Y., (1985). Surface deformation due to shear and tensile faults in a half-space,*Bulletin of the seismological society of America*, 75(4), 1135-1154.

Omer, G. C. (1950). Volcanic tremor, Bull. Seismol. Soc. Am., 40, 175–194.

Pallister, J. S., A. K. Diefenbach, W. C. Burton, J. Muñoz, J. P. Griswold, L. E. Lara, J. B. Lowenstern, and C. E. Valenzuela (2013a). The Chaitén rhyolite lava dome: Eruption sequence, lava dome volumes, rapid effusion rates and source of the rhyolite magma, Andean, Geology, 40(2), 277–294.

Pallister, J. S., D. J. Schneider, J. P. Griswold, R. H. Keeler, W. C. Burton, C. Noyles, C. G. Newhall, and A. Ratdomopurbo (2013b). Merapi 2010 eruption—Chronology and extrusion rates monitored with satellite radar and used in eruption forecasting, J. Volcanol. Geotherm. Res., 261, 144–152.

Parada, M.A., Lahsen, A., Palacios, C., (2000). The Miocene plutonic event of the Patagonian Batholith at 44830V: thermocronological and geobarometric evidence for melting of a rapidly exhumated lower crust. Transactions of the Royal Society of Edinburgh. Earth Sciences 91, 169– 179.

Pardo-Casas, F., Molnar, P., (1987). Relative motion of the Nazca (Farallon) and South American plates since the Late Cretaceous times. Tectonics 6, 233– 248.

Patrick, M. R., J. Dehn, K. R. Papp, Z. Lu, K. Dean, L. Moxey, P. Izbekov, and R. Guritz (2003). The 1997 eruption of Okmok Volcano, Alaska: A synthesis of remotely sensed imagery, J. Volcanol. Geotherm. Res., 127,87–105.

Pavlis,G .L., andJ . R. Booker (1983). A study of the importance on nonlinearity in the inversion of earthquake arrival time data for velocity structure, J. Geophys R. es.,8 8, 5047-5055.

Pedersen, R., Sigmundsson, F. &Einarsson, P., (2007). Controlling factors on earthquake swarms associated with magmatic intrusions; constraints from Iceland,*J. Volcanol. Geothermal Res.*, 162, 73-80, doi:10.1016/j.jvolgeores.2006.12.010.

Pérez-Flores, P., J. Cembrano, P. Sáncez-Alfaro, E. Veloso, G. Arancibia and T. Roquer (2016). Tectonics, magmatism and paleo-fluid distribution in a strike-slip setting: Insights from the northern termination of the Liquiñe Ofqui Fault System, Chile, Tectonophysics, 680, 192–210, doi:10.1016/j.tecto.2016.05.016.

Pieri, D. C., and S. M. Baloga (1986). Eruption rate, area, and length relationships for some Hawaiian lava flows, J. Volcanol. Geotherm. Res., 30, 29–45.

Piña-Gauthier, M., Lara, L.E., Bataille, K., Tassara, A. & Báez, J.C., (2013). Co-eruptive deformation and dome growth during the 2008-2009 Chaitén eruption, Southern Andes,*Andean Geology*, 40(2), 310-323.

Pistolesi, M., Cioni, R., Bonadonna, C., Elissondo, M., Baumann, V., Bertagnini, A., Chiari, L., Gonzales, R., Rosi, M. & Francalanci, L., (2015). Complex dynamics of small-moderate volcanic events: the example of the 2011 rhyolitic Cordón Caulle eruption, Chile, *Bulletin of Volcanology*, 77(1), 1-24.

Prægel, N.-O., and P. M. Holm (2006). Lithospheric contributions to high-MgO basanites from the Cumbre Vieja Volcano, La Palma, Canary Islands and evidence for temporal variation in plume influence, J. Volcanol. Geotherm. Res., 149, 213–239.

Pritchard, M.E. & Simons, M., (2004a). An InSAR-based survey of volcanic deformation in the southern Andes,*Geophysical Research Letters*, 31, L15610, doi:10.1029/2004GL020545.

Pritchard, M.E., Jay, J.A., Aron, F., Henderson, S.T.& Lara, L.E., (2013). Subsidence at southern Andes volcanoes induced by the 2010 Maule, Chile earthquake,*Nature Geoscience*, 6(8), 632-636, doi:10.1038/ngeo1855.

Qamar, A., St. Lawrence, W., Moore, J.N. & Kendrick, G., (1983). Seismic signals preceding the explosive eruption of Mount St. Helens, Washington, on 18 May 1980,*Bulletin of the Seismological Society of America*, 73, 1797–1813.

Richer, M., C. P. Mann, and J. Stix (2004). Maficmagma injection triggers eruption at Ilopango Caldera, El Salvador, Central America, in Natural hazards in El Salvador, Spec. Pap., vol. 375, edited by W. I. Rose et al., pp. 175–189, U.S. Geol. Surv., Boulder, Colo.

Richter, D. H., and J. P. Eaton (1960). The 1959–60 eruption of Kīlauea volcano, New Scientist, 7, 994–997.

Richter, D. H., J. P. Eaton, K. J. Murata, W. U. Ault, and H. L. Krivoy (1970). Chronological narrative of the 1959–60 eruption of Kīlauea Volcano, Hawaii, U.S. Geol. Surv. Prof. Pap., 537,1–73.

Rodríguez, E., Morris, C.S.& Belz, J.E., (2006). A Global Assessment of the SRTM Performance,*Photogrammetric Engineering & Remote Sensing*, 72(3), 249–260.

Rose, W. I. (1973). Pattern and mechanism of volcanic activity at the Santiaguito volcanic dome, Guatemala, Bull. Volcanol., 37,73–94.

Rowland, S. K. (1996). Slopes, lava flow volumes and vent distributions of Volcán Fernandina, Galápagos Islands, J. Geophys. Res., 101, 27,657–27,672, doi:10.1029/96JB02649.

Rowland, S. K., and D. C. Munro (1993). The 1919–1920 eruption of Mauna Iki Kīlauea: Chronology, geologic mapping and magma transport mechanisms, Bull. Volcanol., 55, 190–203.
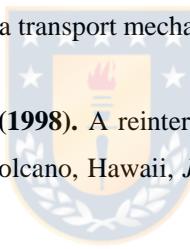
Rubin, A.M., Gillard, D. & Got, J.L., (1998). A reinterpretation of seismicity associated with the January 1983 dike intrusion at Kilauea Volcano, Hawaii, *Journal of Geophysical Research, 103(B5), 10003-10015.*

Sambridge, M., &Mosegaard, K., (2002). Monte Carlo Methods in Geophysical Inverse Problems. Rev. Geophys 40(3), 1009, doi:10.1029/2000RG00089.

Sánchez, P., P. Pérez-Flores, G. Arancibia, J. Cembrano, and M. Reich (2013). Crustal deformation effects on the chemical evolution of geothermal systems: The intra-arc Liquiñe–Ofqui fault system, Southern Andes, Int. Geol. Rev., 55(11), 1384–1400, doi:10.1080/00206814.2013.775731.

Sarao A.; Panza G.; Privitera E.; Cocina O. (2001). Non-double- couple mechanisms in the seismicity preceding the 1991–1993 Etna volcano eruption, Geophys. J. Int.145, 319 –335.

Schipper, C. I., J. M. Castro, H. Tuffen, M. R. James, and P. How (2013). Shallow vent architecture during hybrid explosive-effusive activity at Cordón Caulle (Chile, 2011–12): Evidence from direct observations and pyroclast textures, J. Volcanol. Geotherm. Res., 262,25–37.

Scholz, C.H., (1968). The frequency–magnitude relation of microfracturing in rock and its relation to earthquakes. Bull. Seismol. Soc. Am. 58, 399–415.

Schorlemmer, D., Weimer, S., Wyss, M., (2004). Earthquake statistics at Parkfield: 1. Stationarity of b values. J. Geophys. Res. 109, B12307.doi:10.1029/2004JB003234.

Schorlemmer, D., Wiemer, S., Wyss, M., (2005).Variations in earthquake-size distribution across different stress regimes.Nature 437, 539–542.

Segall, P., (2010). Earthquake and volcano deformation. Princeton University Press.

Sepúlveda, F., Lahsen, A., Bonvalot, S., Cembrano, J., Alvarado, A. & Letelier, P., (2005). Morpho-structural evolution of the Cordón Caulle geothermal region, Southern Volcanic Zone, Chile: Insights from gravity and 40Ar/ 39Ar dating, *Journal of Volcanology and Geothermal Research*, 148(1), 165-189.
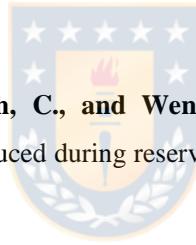
Shapiro, S., Dinske, C., Langenbruch, C., and Wenzel, F. (2010). "Seismogenic index and magnitude probability of earthquakes induced during reservoir fluid stimulations." The Leading Edge, 29(3), 304–309. doi: 10.1190/1.3353727

Sigmundsson, F., Hooper, A., Hreinsdóttir, S., Vogfjörd, K.S., Ófeigsson, B.G., Heimisson, E.R., Dumont, S., Parks, M., Spaans, K., Guðmundsson, G.B., Drouin, V., Árnadóttir, T., Jónsdóttir, K., Gudmundsson, M.T., Högnadóttir, T., Fridriksdóttir, H.M., Hensch,M., Einarsson, P., Magnússon, E., Samsonov, S., Brandsdóttir, B., White, R.S., Ágústsdóttir, T., Greenfield, T., Green, R.G., Hjartardóttir, Á.R., Pedersen, R., Bennett, R.A., Geirsson, H., La Femina, P.C., Björnsson, H., Pálsson, F., Sturkell, E., Been, C.J., Möllhoff, M., Braiden, A.K. &Eibl, E.P.S., (2015). Segmented lateral dyke growth in a rifting event at Bárðarbunga volcanic system, Iceland, *Nature*, 517, 191-195, doi:10.1038/nature14111.

Silva, P.; Lara, L.; Amigo, A.; Bertin, D.; Orozco, G.; (2012). Caracterización de los principales productos eruptivos emitidos durante la erupción del Complejo Volcánico Puyehue-Cordón Caulle 2011-2012. Congreso Geológico Chileno, Antofagasta.

Singer, B. S., Jicha, B.R., Harper, M.A., Naranjo, J.A., Lara, L.E.& Moreno-Roa, H., (2008). Eruptive history, geochronology, and magmatic evolution of the Puyehue-Cordón Caulle volcanic complex, Chile,*Geological Society of America Bulletin*, 120(5-6), 599-618.

Sokos E. y Zahradnik J. (2008). ISOLA A Fortran code and MatLab GUI to perform multiple-point sourse inversion of seismic data, *ComputGeosci.*34, 967-977.

Sokos, E. N., J. Zahradník, A. Kiratzi, J. Janský, F. Gallovič, O. Novotný, J. Kostelecký, A. Serpetsidaki, and G.-A. Tselentis. (2012). The January 2010 Efpalio earthquake sequence in the western Corinth Gulf (Greece), Tectonophysics 530-531, 299-309.

Sparks, R. S. J., et al. (1998). Magma production and growth of the lava dome of the Soufrière Hills Volcano, Montserrat, West Indies: November 1995 to December 1997, Geophys. Res. Lett., 25, 3421–3424, doi:10.1029/98GL00639.

Stanton-Yonge, A. (2016). Tectonic role of margin-parallel and margin-transverse faults during oblique subduction at the southern volcanic zone of the Andes (master's thesis). Pontificia Universidad Católica de Chile. Retrieved from https://repositorio.uc.cl/ handle/11534/16840.

Stasiuk, M. V., and C. Jaupart (1997). Lava flow shapes and dimensions as reflections ofmagma system conditions, J. Volcanol. Geotherm. Res., 78,31–50.

Stephens, C.D., Chouet, B.A., (2001). Evolution of the December 14, 1989 precursory long-period event swarm at Redoubt Volcano, Alaska. J. Volcanol. Geotherm. Res. 109 (1–3), 133– 148.

Stern, CR. (2004). Active Andean volcanism: its geologic and tectonic setting. Revista Geológica de Chile, Volumen 31, Numero 2, 181-206.

Surono, P., et al. (2012). The 2010 explosive eruption of Java'sMerapivolcano—A '100-year' event, J. Volcanol. Geotherm. Res., 241–242,121–135.

Swanson, D. A., and R. T. Holcomb (1990). Regularities in growth of the Mount St. Helens dacite dome, 1980–1986, in In Lava Flows and Domes, edited by J. H. Fink, pp. 3–24, Springer, Berlin, New York.

Swanson, D. A., D. Dzurisin, R. T. Holcomb, E. Y. Iwatsubo, W. W. Chadwick Jr., T. J. Casadevall, J. W. Ewert, and C. C. Heliker (1987). Growth of the lava dome at Mount St. Helens, Washington, in The Emplacement of Silicic Domes and Lava Flows, Geol. Soc. Am. Spec. Pap., vol. 212, edited by J. H. Fink, pp. 1–16, Geol. Soc. of Am., Boulder, Colo.

Swanson, D. A.,W. A. Duffield, D. B. Jackson, and D.W. Peterson (1979). Chronological narrative of the 1969–71Mauna Ulu eruption of Kīlauea volcano, Hawaii, U.S. Geol. Surv. Prof. Pap., 1056,1–55.

Tanguy, J. C., G. Kieffer, and G. Pantanè (1996). Dynamics, lava volume and effusion rate during the 1991–1993 eruption of Mount Etna, J. Volcanol. Geotherm. Res., 71, 259–265.

Tárraga, M., J. Martí, R. Abella, R. Carniel, and C. López (2014). Volcanic tremors: Good indicators of change in plumbing systems during volcanic eruptions, J. Volcanol. Geotherm. Res., 273,33–40.

Tassara A., Soto H., Bedford J., Moreno M., Baez J.C. (2015). Contrasting amount of fluids along the megathrust ruptured by the 2010 Maule earthquake as revealed by a combined analysis of ftershocks and afterslip.Tectonophysics 671, 2016, 95-109.

Tassara, A., Yañez, G. (2003). Relación entre espesor elástico de la litósfera y la sementación tectónica del margen andino. Revista Geológica de Chile, Vol30, N°2, pp159-186

Tassara, A., Schmidt, S., Tasarova, Z., Hackney, R., Wienecke, S., Go¨ tze, H.J., (2004). Structure, composition and thermo-mechanical state along the segmented Andean margin. Abstracts IAVCEI General Assembly, Symposium 8f.

Templeton D. and Dreger D. (2006). Non-Double-Couple Earthquakes in the Long Valley Volcanic Region. Bulletin of the Seismological Society of America, Vol. 96, No. 1, 69–79.

Thomson, S.N., (2002). Late Cenozoic geomorphic and tectonic evolution of the Patagonian Andes between latitutes 42ºS and 46ºS: an appraisal based on fission-tracks results from the transpressional intra-arc Liquin˜e–Ofqui fault zone. Geological Society of America Bulletin 114 (9), 1159– 1173.

Thurber, C.H. (1983). Earthquake locations and three-dimensional crustal structure in the Coyote Lake area, Central California. Journal of Geophysical Research 88: doi: 10.1029/JB080i010p08226. issn: 0148-0227.

Tibaldi, A., (1995). Morphology of pyroclastic cones and tectonics. J. Geophys. Res. 100, 24,521–24,535.

Tikhonov, A. N., Arsenin V. Y. (1977). Solutions of Ill-posed Problems, Winston, Washington, DC (1977).

Tilling, R. I. (1987). Fluctuations in surface height of active lava lakes during the 1972–1974 Mauna Ulu eruption, Kīlauea Volcano, Hawaii, J. Geophys. Res., 92, 13,721–13,730, doi:10.1029/JB092iB13p13721.

Tregoning, P. & Watson, C., (2009). Atmospheric effects and spurious signals in GPS analyses,*Journal of Geophysical Research*, 114, B09403, doi:10.1029/2009JB006344.
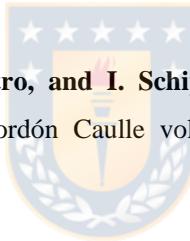
Tuffen, H., M. R. James, J. M. Castro, and I. Schipper (2013). Exceptional mobility of an advancing rhyolitic obsidian flow at Cordón Caulle volcano in Chile, Nat. Commun., 4, 2709, doi:10.1038/ncomms3709.

Umakoshi, K., Shimizu, H., Matsuwo, N., (2003). Seismic activity associated with the endogenous growth of lava dome at UnzenVolcano, Japan. Abstract V10/01A/D-014, IUGG XXIII Meeting, Sapporo, Japan.

Ussher, G., Harvey C., Johnstone, R. & Anderson E., (2000). Understanding resistivities observed in Geothermal Systems, in Proceedings World Geothermal Congress 2000, Kyushu-Tohoku, Japan.

Utsu, T., (1965). A method for determining the value of b in a formula log N=a−bM showing the magnitude frequency for earthquakes. Geophys. Bull. Hokkaido Univ. 13, 99–103.

Vander Hilst, R.D., and W. Spakman (1989). Importance of the reference model in linearizedt omographya nd imageso f subductionb elow the Caribbeanp late,G eophysR. es.L ett., 16, 1093-1096,1989.

Vavryčuk, V. (2007). On the retrieval of moment tensors from borehole data, Geophys. Prospect. 55, 381–391.

Vigouroux, N., A. E. Williams-Jones, P. Wallace, and T. Staudacher (2009). The November 2002 eruption of Piton de la Fournaise, Réunion: Tracking the pre-eruptive thermal evolution of magma using melt inclusions, Bull. Volcanol., 71, 1077–1089.

Villeneuve, N. (2000). Apports multi sources à une meilleure compréhension de la mise en place des coulées de lave et des risques associés au Piton de la Fournaise: Géomorphologie quantitative en terrain volcanique, PhD thesis, Institut de Physique du Globe de Paris, 378 pp.

Wadge, G. (1978). Effusion rate and the shape of aa lava flow-fields on Mount Etna, Geology, 6, 503–506.

Wadge, G. (1981). The variation of magma discharge during basaltic eruptions, J. Volcanol. Geotherm. Res., 11, 139–168.
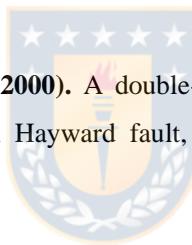
Waldhauser, F., & Ellsworth, W. L. (2000). A double-difference earthquake location algorithm: Method and application to the northern Hayward fault, California. Bulletin of the Seismological Society of America, 90(6), 1353-1368.

Walker, G. P. L. (1973). Lengths of lava flows, Philos. Trans. R. Soc. London, 274, 107–118.

Walter, T.R., Amelung, F., (2007). Volcanic eruptions following M≥9 megathrust arthquakes: implications for the Sumatra–Andaman volcanoes. Geology 35, 539–542.

Wendt, A., Tassara, A., Báez, J. C., Basualto, D., Lara, L., García, F., (2016). Possible structural control on the 2011 eruption of Puyehue-CordónCaulle Volcanic Complex (southern Chile) determined by InSAR, GPS and seismicity.Geophysical Journal International, GJI-15-1036.R1.

Werner, C., Wegmüller, U., Strozzi, T. & Wiesmann A., (2000). Gamma SAR and interferometric processing software,in *Proceedings of the ERS-ENVISAT Symposium, Gothenburg, Sweden*, pp. 16-20.

Werner, C., Wegmüller, U., Strozzi, T.& Wiesmann A., (2003). Processing strategies for phase unwrapping for INSAR applications,*Proceedings EUSAR 2002, Cologne, 4-6 June, 2002*.

Wicks, C. W. Jr., J. C. de la Llera, L. E. Lara, and J. Lowenstern, (2011). The role of dyking and fault control in the rapid onset of eruption at Chaitén volcano, Chile, Nature, 478(7369), 374–377, doi:10.1038/nature10541.

Wiemer, S., Benoit, J.P., (1996). Mapping the b-value anomaly at 100 km depth in Alaska and New Zealand subduction zones. Geophys. Res. Lett. 24, 189–192.

Wiemer, S., McNutt, S.R., (1997). Variations in the frequency–magnitude distribution with depth in two volcanic areas: Mount St. Helens, Washington, and Mt. Spurr, Alaska. Geophys. Res. Lett. 24, 189–192.

Wiemer, S., McNutt, S.R.,Wyss,M., (1998). Temporal and three-dimensional spatial analyses of the frequency–magnitude distribution near Long Valley Caldera, California. Geophys. J. Int. 134, 409–421.

Wiemer, S., Wyss, M., (2000). Minimum magnitude of completeness in earthquake catalogs: examples from Alaska, the western United States, and Japan. Bull. Seismol. Soc. Am. 90 (4), 859–869.
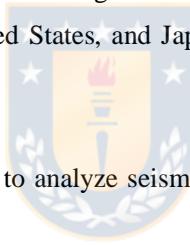
Wiemer, S., (2001). A software package to analyze seismicity: ZMAP. Seismol. Res. Lett. 72, 373–382.

Wiemer, S., Wyss, M., (2002). Mapping spatial variability of the frequency–magnitude distribution of earthquakes. Adv. Geophys. 45, 259–302.

Wolfe, E. W., *and* R. P. Hoblitt *(1996).* Overview of the eruptions, in Fire and Mud: Eruptions and Lahars of Mount Pinatubo, Philippines, edited by C. G. Newhall, and R. S. Punongbayan, pp. 3–20, Univ. of Wash. Press, Seattle.

Woods, A.W., and T. Koyaguchi (1994). Gas transport and bubble collapse in rhyoliticmagma: An experimental approach, Nature, 3767yy7u60, 641–644.

Wright, T.J., Parsons, B.E.& Lu, Z., (2004). Toward mapping surface deformation in three dimensions using InSAR. *Geophys. Res. Lett.*, 31, L01607, doi:10.1029/2003GL018827.

Wyss, M., (1973). Towards a physical understanding of the earthquake frequency distribution.Geophys. J. R. Astron. Soc. 31, 341–359.

Wyss, M., Hasegawa, A., Nakajima, J., (2001). Source and path of magma for volcanoes in the subduction zone of northeastern Japan, Geophys. Res. Lett., 28(9), 1819–1822, doi:10.1029/2000GL012558.

Yamaoka, K., J. Oikawa, and Y. Ida (1991). An isotropic source of volcanic tremor – Observation with a dense seismic network at Izu-Oshima volcano, Japan, J. Volcanol. Geotherm. Res., 47, 329–336.

Zhang, H., & Thurber, C. (2006). Development and applications of double-difference seismic tomography. *Pure and Applied Geophysics*, *163*(2), 373-403.